Murilo Henrique de Oliveira

Electromagnetically induced transparency under effects of light-mediated interactions, entanglement generation, and Fock states detection.

São Carlos

October 2022

Murilo Henrique de Oliveira

Electromagnetically induced transparency under effects of light-mediated interactions, entanglement generation, and Fock states detection.

PhD thesis submitted to the Postgraduate Coordination in Physics of the Center for Exact Sciences and Technology (CCET) at the Federal University of São Carlos.

Federal University of São Carlos – UFSCar

Center for Exact Sciences and Technology (CCET)

Graduate Program in Physics/CCET

Supervisor: Celso Jorge Villas-Bôas

São Carlos

October 2022

UNIVERSIDADE FEDERAL DE SÃO CARLOS

Centro de Ciências Exatas e de Tecnologia
Programa de Pós-Graduação em Física

Folha de Aprovação

Defesa de Tese de Doutorado do candidato Murilo Henrique de Oliveira, realizada em 25/10/2022.

Comissão Julgadora:

Prof. Dr. Celso Jorge Villas Boas (UFSCar)

Profa. Dra. Yara Galvão Gobato (UFSCar)

Prof. Dr. Raul Celistrino Teixeira (UFSCar)

Prof. Dr. Rafael Rothganger de Paiva (UFABC)

Prof. Dr. Daniel Felinto Pires Barbosa (UFPE)

O Relatório de Defesa assinado pelos membros da Comissão Julgadora encontra-se arquivado junto ao Programa de Pós-Graduação em Física.

To my loving wife and parents.

Acknowledgements

First of all, I would like to thank Celso Jorge Villas-Bôas for literally everything. His friendly and welcoming orientation ever since I first walked into his office, his encouragement, dedication and trust, have provided me inspiration and motivation during these past six years.

To Markus Hennrich and Ana Predojević, who I was fortunate enough to meet and have as supervisors while I was abroad. Thank you very much for the warm welcome, the time invested in me, the teachings and guidance during the wonderful year I spent in Stockholm with you. I surely learned a lot from you.

To Maria Lorena Teodoro, my beloved wife and friend, for her love, companionship and understanding. Thank you for being by my side throughout all the ups and downs, you have been a comforting constant amidst all the crazy variables of life, and no matter what, at the end of the day, I know you will be there for me.

To my parents, Daicy Márcia Bergui de Oliveira and Sergio Henrique de Oliveira, who made all of this possible. You have given me more than I could ever ask for. Thank you for all the love, support, care, and for sacrificing so much for me.

To Fernando Redivo Cardoso, whose friendship is surely one of the most valuable things I could take away from this PhD. Thank you for the company, daily conversations and physical discussions.

To Carlos Eduardo Máximo, for all the patience and time working side by side with me to complete the main work of this project. Thank you for all the discussions, conversations and meetings (often outside of working hours).

To my cousin Eduardo Henrique dos Santos, who has been nothing less than a brother to me. Thank you for these almost 30 years of friendship and companionship.

To Edmar Bueno, Elias Filipe Marinho da Costa and all my other friends and colleagues who directly or indirectly were part of this work. There are many names that should be cited here, but unfortunately I can't thank you all individually.

Finally, I would like to thank CNPq (141247/2018-5) and CAPES-STINT (BR2018-8054) for the financial support during the whole project, thus making its progress and conclusion possible.

Abstract

This thesis presents a brief compilation of the works developed during my doctorate, and can be divided basically into three main parts. In the first one, we show the changes caused by considering long-range interactions mediated by light in the phenomenon of electromagnetically induced transparency (EIT). We also show how these interactions can negatively impact population transfer through a stimulated Raman adiabatic passage (STIRAP) process, which may imply a technical limitation for EIT-based quantum memories, as the density and optical thickness of the samples have been increasing in recent experiments to obtain better efficiencies. In the second part, we propose two new schemes to generate highly entangled states in a system of two non-degenerate qubits coupled to a common bosonic mode, in both of which we use an EIT analogue to better understand and interpret the physics of the system. The first method relies on the injection of energy into the mode through a coherent pump to prevent the mode from decaying to vacuum, and under a certain parameter regime, we show that it is possible to obtain a maximally entangled steady state. In the second method, we transfer the population to the maximally entangled state through a STIRAP-like process. In the third and last part, we present a new idea for single-shot measurements of Fock states using the Autler-Townes effect, where two methods are proposed: both a destructive and a non-destructive one. The results presented were obtained from the experimental implementation of this scheme in a system of trapped ions, for measurements of phonon number states.

Keywords: Electromagnetically Induced Transparency, Stimulated Raman Adiabatic Passage, Quantum Memories, Entanglement, Single-shot phonon number measurements, Trapped Ions.

Abstract

Esta tese é um breve compilado dos trabalhos desenvolvidos durante meu doutorado, podendo ser dividida basicamente em três partes principais. Na primeira, mostramos as mudanças causadas quando consideramos interações de longo alcance mediadas por luz no fenômeno da transparência eletromagneticamente induzida (EIT). Além disso, mostramos como essas interações podem impactar negativamente a transferência de população através de um processo STIRAP, o que pode implicar em uma limitação técnica para memórias quânticas baseadas em EIT, já que a densidade e a espessura óptica das amostras vêm sendo cada vez mais aumentadas em experimentos recentes, a fim de obter melhores eficiências. Na segunda parte da tese, propomos dois novos esquemas para gerar estados altamente emaranhados em um sistema de dois qubits não-degenerados acoplados a um modo bosônico comum, sendo que em ambos os métodos, usamos um análogo de EIT para uma melhor compreensão e interpretação física do que está acontecendo no sistema. O primeiro método baseia-se na injeção de energia no modo bosônico através de um bombeio coerente para evitar que o modo decaia para vácuo, e sob um determinado regime de parâmetros mostramos ser possível obter um estado estacionário maximamente emaranhado. No segundo método, transferimos a população para o estado maximamente emaranhado através de um processo do tipo STIRAP. Por fim, na terceira e última parte da tese, apresentamos uma nova ideia para medições de estados Fock usando o efeito Autler-Townes, onde são propostos dois métodos: um destrutivo e um não destrutivo. Os resultados apresentados foram obtidos a partir da implementação experimental deste esquema em um sistema de íons aprisionados, para medidas de estados de números de fônons.

Palavras-chave: Transparência Eletromagneticamente Induzida, STIRAP, Memórias Quânticas, Emaranhamento, Medições de Números de Fônons, Íons Aprisionados.

List of Figures

Figure 1 – Level scheme. A two-level atom, with ground and excited states $|g\rangle$ and $|e\rangle$, respectively, is coupled resonantly to a quantized mode of Rabi frequency g and frequency ω. 23

Figure 2 – Energy level diagrams. (a) Energy levels of a three-level atom in the Λ configuration in free space and in the presence of classical fields. (b) Effect of the control field on the atom, where the strong coupling of the transition $|2\rangle \leftrightarrow |3\rangle$ causes a splitting of $|3\rangle$ and $|2\rangle$ into two symmetric dressed states $|a_{\pm}\rangle$. 25

Figure 3 – Optical response. a) Normalized absorption as a function of the detuning for a two-level atom and a three-level atom in the EIT regime. b) Refraction index of a two-level atom and a three-level atom in the EIT regime. The black dashed curves refer to the two-level system atom while the blue filled ones to the three-level system. The system parameters were set to $\Omega_p = \Gamma_{31}/50$, $\gamma_2 = \gamma_3 = 0$. For the 2-level atom curves the additional parameters were set to $\Gamma_{32} = 0$ and $\Omega_c = 0$. For the 3-level atom EIT curves these parameters were chosen as $\Gamma_{32} = \Gamma_{31}$ and $\Omega_c = \Gamma_{31}/5$. 30

Figure 4 – (a) Level scheme of a three-level atom in a Λ configuration trapped inside an optical cavity. A classical control field with frequency ω_c and Rabi frequency $2\Omega_c$, couples one of the atomic transitions. The other atomic transition is coupled by the cavity mode of frequency ω and vacuum Rabi frequency $2g$. We also consider a probe field with strength ε and frequency ω_P. (b) Pictorial representation of the experimental observation of the EIT phenomenon with a probe and a control fields, both focusing on a trapped atom inside a linear optical cavity, and a properly positioned detector, in order to measure the transmission. . . 31

Figure 5 – Transmission spectrum. The dashed blue curve represents the empty cavity situation, with maximum transparency at $\Delta_p = 0$ and FWHM = κ. The dotted red curve refers to the case of a two-level atom inside the cavity, with transmission peaks located exactly at $\Delta_p = \pm g$. The solid black curve shows the CEIT transmission spectrum with maximum transparency at resonance, just like the empty cavity, but with much narrower FWHM. It is also possible to observe peripheral peaks, which appear at the Autler-Townes doublet resonance at $\Delta_p = \pm\sqrt{g^2 + \Omega_c^2}$. CEIT parameters: $g = 5\kappa$, $\Omega_c = 2\kappa$, $\varepsilon = \sqrt{0.01}\kappa$, $\Delta_1 = \Delta_2 = 0$ and $\Gamma_{31} = \Gamma_{32} = 0.5\kappa$. For the empty cavity curve $\Omega_c = 0$, and for the two-level atom $\Omega_c = 0$ and $\Gamma_{32} = 0$. 34

Figure 6 – A cylindrical and homogeneous cold cloud of N disordered three-level atoms scatters probe and control fields to the free space. The atomic levels are in a Λ configuration, as schematically shown on the left. The radius R of the cylindrical surface is much larger than its thickness L, measuring the probe field transmission in a disk of radius $s_{\max} < R$. Taken from Ref. [1]. 38

Figure 7 – Transmission spectrum as a function of the probe field detuning. (a) and (c) were calculated in the EIT regime ($\Omega_2 = 0.5\Gamma \gg \Omega_1 = 0.1\Gamma$), while (b) and (d) were obtained for the CPT regime ($\Omega_2 = \Omega_1 = 0.5\Gamma$). In (a) and (b) we see the changes in the transmission spectrum for different values of the atomic density ρ, for a fixed cylinder thickness $k_1 L = 40$. While for (c) and (d) we vary $k_1 L$ for a fixed density $\rho/k_1^3 = 0.01$. In panels (a) and (b), the number of atoms N ranged from 314 to 3140 and, in panels (c) and (d), from 785 to 2335. For all plots we set $\Delta_2 = 0$ and $k_1 R = 50$. Taken from Ref. [1]. 44

Figure 8 – FWHM as a function of ρ and L for models with and without interacting terms. The full black curves are obtained by solving the full system of Equations (3.19)-(3.21), whereas dashed orange curves by turning off all dipole interactions. (a) and (c) were calculated in the EIT regime ($\Omega_2 = 0.5\Gamma \gg \Omega_1 = 0.1\Gamma$), while (b) and (d) were obtained for the CPT regime ($\Omega_2 = \Omega_1 = 0.5\Gamma$). In (a) and (b) we see the changes in the FWHM by varying the atomic density ρ, for a fixed cylinder thickness $k_1 L = 40$, while for (c) and (d) we vary $k_1 L$ for a fixed density $\rho/k_1^3 = 0.01$. For all plots we set $\Delta_2 = 0$ and $k_1 R = 50$, and the maximum number of atoms in the cloud in the simulations was $N = 3142$. Taken from Ref. [1]. 45

Figure 9 – Minimum value of transmission as a function of ρ and L. The full black curves are obtained by solving the full system of dynamical equations, whereas dashed orange curves by turning off all dipole interactions. (a) and (c) were calculated in the EIT regime ($\Omega_2 = 0.5\Gamma \gg \Omega_1 = 0.1\Gamma$), while (b) and (d) were obtained for the CPT regime ($\Omega_2 = \Omega_1 = 0.5\Gamma$). In (a) and (b) we see the changes in the FWHM by varying the atomic density ρ, for a fixed cylinder thickness $k_1 L = 40$, while for (c) and (d) we vary $k_1 L$ for a fixed density $\rho/k_1^3 = 0.01$. For all plots we set $\Delta_2 = 0$ and $k_1 R = 50$, and the maximum number of atoms in the cloud in the simulations was $N = 3142$. As a result of the asymmetry discussed in the text, we obtain different values of $T_{\min}$ for opposite detunings, around $\Delta_1 = \pm\sqrt{\Omega_1^2 + \Omega_2^2}/2$, so $T_{\min}$ refers to the lowest value between the two. Taken from Ref. [1]. 47

Figure 10 – STIRAP process in a cold cloud of three-level atoms. Panel (a) shows how the Rabi frequencies of the probe and control field change in time, starting in a condition where $\Omega_1 \ll \Omega_2$ and adiabatically reaching a regime where $\Omega_1 \gg \Omega_2$. Panel (b) shows how the average ground state population of the state $|1\rangle$ behaves for different densities. For all plots we set $\Omega_{\max} = 0.5\Gamma$, $t_0 = 10\Gamma$, $t_r = 60\Gamma$, $\Delta_1 = \Delta_2 = 0$, $k_1 L = 60$ and $k_1 R = 40$. The number of atoms N ranges from 1005 to 3015. Taken from Ref. [1]. 48

Figure 11 – a) Two non-degenerate qubits, with both ground states coupled to the bosonic mode of frequency ω_m, detuned by $\pm\Delta$. b) Level scheme of the same system, but now in the basis up to one excitation: $|G\rangle \otimes |0\rangle$, $|E\rangle = |G\rangle \otimes |1\rangle$, and $|\Psi_\pm\rangle = |\Phi_\pm\rangle \otimes |0\rangle$, where $|G\rangle = |g, g\rangle$ and $|\Phi_\pm\rangle = (|e, g\rangle \pm |g, e\rangle)/\sqrt{2}$. Here, g promotes transitions from $|E\rangle$ to $|\Psi_+\rangle$, while Δ from $|\Psi_+\rangle$ to $|\Psi_-\rangle$. We consider a pump field, of strength ε, continuously injecting energy into the mode to combat decay from the mode with rate κ. The inset in b) shows the entangled steady state partial density matrix, where the bosonic mode has been traced out. Taken from Ref. [2]. 53

Figure 12 – Entanglement generation using the steady-state method. (a) Colormap showing the concurrence of the steady state as a function of Δ/κ and g/κ. Points A to D are referred to in panel (d). Colormap showing the concurrence of the steady state as a function of g, Δ (given the constraint $\Delta = 0.1g$) and ε. (c) Concurrence as a function of the spontaneous decay rate Γ of each of the two qubits (top x-axis) and as a function of the detuning (bottom x-axis). (d) Concurrence as a function of time for different parameter sets, given in panel (a). The concurrence generally grows and then stabilises. The insets in panel (d) show the steady state partial density matrix of each curve, where the mode has been traced out. For all panels except (b), the pump strength was set to $\varepsilon = \kappa$. The spontaneous decay rate of each qubit was fixed at $\Gamma = 10^{-5}\kappa$, except for the red dashed curve in (c). The constant parameters at (c) are given by point D in panel (a). Taken from Ref. [2]. 56

Figure 13 – Entanglement generation - adiabatic method with tunable g and Δ. (a) Two two-level ions are trapped in a harmonic potential and coupled to the same phonon mode. The ions are subjected to a magnetic field gradient, which promotes different energy shifts to their excited states, recovering the system illustrated in Fig. 11(a). (b) Pictorial representation of the energy shifts in the ions excited states due to a magnetic field gradient, as a function of their position in the trap. (c) Time evolution of the parameters $g(t)$ and $\Delta(t)$ as described in Eq. (4.9) and (4.10), with the corresponding populations changes in (d). We considered for all simulations. Adopted parameters: $\Gamma = 10^{-3}\kappa$, $g_{\max} = \Delta_{\max} = 2 \times 10^{4}\kappa$, $t_0 = 4 \times 10^{-3}\kappa$, $\lambda = 10^{3}\kappa$. Taken from Ref. [2]. 58

Figure 14 – Entanglement generation - adiabatic method. (a) Time evolution of g and Δ, with Δ varying accordingly to Eq. (4.10) and a constant g. (b) Population changes over time. We considered $\Gamma = 10^{-3}\kappa$, $\Delta_{\max} = 2 \times 10^{5}\kappa$, $g = 2.5 \times 10^{3}\kappa$, $t_0 = 4 \times 10^{-3}/\kappa$, $\lambda = 5 \times 10^{2}\kappa$. Taken from Ref. [2]. 59

Figure 15 – The Autler-Townes effect. Left: The $|D\rangle \leftrightarrow |S\rangle$ resonance is weakly probed while levels $|S\rangle$ and $|D'\rangle$ are strongly coupled on a BSB transition. The splitting principles are the same for a RSB transition, solely the coupling strength dependency on the phonon number changes. Right: The system described in terms of dressed states. The splitting between the dressed states reveals the $|S\rangle \leftrightarrow |D'\rangle$ coupling strength Ω_C. 63

Figure 16 – Splitting of the Autler-Townes doublet. When the coupling field is resonant to a phonon-number-changing transition the splitting of the Autler-Townes doublet depends on the number of phonons in the system. (a) The coupling field was resonant to a BSB transition and the splitting scales with the phonon number n as $\sqrt{n+1}$. (b) The coupling field was resonant to a RSB transition and the splitting scales with $\sqrt{n}$. Error bars represent quantum projection noise (68% confidence intervals). (c) The blue and red data points were extracted from the doublet splitting in (a) and (b) via a fit (with the amplitude as a fitting parameter), and are described by $\sqrt{n+1}$ and $\sqrt{n}$ scalings, respectively. 64

Figure 17 – (a) Measurement sequence: The ion is initialised in $|D\rangle$ with phonon number n. First a π pulse on the $|D\rangle \leftrightarrow |S\rangle$ carrier transition is attempted while a phonon-number-changing transition is strongly coupled (in the figure a BSB trasition is shown). During this step the probe field is detuned such that the $|D\rangle \rightarrow |S\rangle$ transfer only occurs if n equals the test value m. Then any population in $|D'\rangle$ is transferred to $|S'\rangle$ before both S states are coupled to the fluorescing state $|f\rangle$. Finally, detection of fluorescence indicates $n = m$. (b) Experimental demonstration of the sequence in (a). The ion was prepared in different Fock states, and when the probed Fock state matched the detection, the prepared Fock state fluorescence was detected. (c) Experimental results when the transfer step used the $|D\rangle \leftrightarrow |S\rangle$ carrier transition instead, enabling a non-destructive measurement of the ion motion in the Fock basis. . . . 66

Figure 18 – Phonon number distributions. For a thermal distribution the Autler-Townes splitting shows multiple peaks at the different motional modes. The peak position is defined by the phonon number and the amplitude by the population probability of this mode. By scanning the Autler-Townes spectrum one can obtain therefore the thermal distribution of the ion. 67

Figure 19 – The ion is trapped using a linear Paul trap. The cooling, repump laser and the weak probe beam are under a 45° angle to the trap axis. The remaining lasers for operations on the qubit transition are applied from the radial as well as then angled direction. Detection was done with a photomultiplier tube (PMT) mounted at the top of the experiment. . . 88

Contents

1 OVERVIEW . . . 21

2 THEORETICAL BACKGROUND . . . 23
2.1 Jaynes-Cummings model . . . 23
2.2 Electromagnetically induced transparency . . . 25
2.2.1 Model . . . 25
2.2.2 Dark state . . . 26
2.2.3 Optical response . . . 27
2.2.4 Exact solution for the steady state . . . 30
2.3 Cavity electromagnetically induced transparency . . . 31
2.3.1 Model . . . 31
2.3.2 Dark state . . . 32
2.3.3 Transmission . . . 34

3 SENSITIVITY OF ELECTROMAGNETICALLY INDUCED TRANSPARENCY TO LIGHT-MEDIATED INTERACTIONS . . . 37
3.1 Introduction . . . 37
3.2 Microscopic model . . . 39
3.3 Collective Transparency Window . . . 42
3.4 Collective STIRAP . . . 46
3.5 Conclusion . . . 49

4 STEADY-STATE ENTANGLEMENT GENERATION FOR NON-DEGENERATE QUBITS . . . 51
4.1 Introduction . . . 51
4.2 Model . . . 52
4.3 Steady state entanglement production . . . 54
4.4 Adiabatic process . . . 57
4.5 Conclusion . . . 59

5 SINGLE-SHOT MEASUREMENTS OF PHONON NUMBER STATES USING THE AUTLER-TOWNES EFFECT . . . 61
5.1 Introduction . . . 61
5.2 Autler-Townes effect caused by coupling on a phonon-number-changing transition . . . 62

5.3 Pulse sequence to efficiently measure ion motion in the number state basis . . . 63
5.4 Limitations of the technique . . . 65
5.5 Conclusion . . . 67

6 OUTLOOK . . . 69

BIBLIOGRAPHY . . . 71

APPENDIX 83

APPENDIX A – SCATTERING CROSS SECTION AND OPTICAL DEPTH FOR A Λ THREE-LEVEL ATOM . . . 85

APPENDIX B – FOCK STATE DETECTOR . . . 87
B.1 Experimental setup . . . 87
B.2 Experimental parameters . . . 87
B.3 Autler-Townes line shape . . . 88
B.3.1 Red-sideband (RSB) . . . 89
B.3.2 Blue sideband (BSB) . . . 90

1 Overview

In the present manuscript, I will present the main results obtained during the last years in my doctoral project, under the supervision of Celso Jorge Villas-Bôas.

Since my master's degree, I have sought to specialize in the field of quantum optics, studying radiation-matter interaction focusing specially on the phenomenon of electromagnetically induced transparency (EIT) and its analogues. Therefore, I believe that the works that I will present here reflect some of this.

The initial idea for the project, to study how long-range interactions mediated by light affect the EIT phenomenon, emerged during an internal seminar session of the group, where each one presented a little of their work, when Celso suggested that alongside Carlos Eduardo Máximo, who was a postdoc specialist in multiple scattering, I should tackle this issue. This collaboration proved to be very fruitful, and I was able to learn a lot from Carlos about his research area, resulting in a publication in Physical Review A [1], entitled "Sensitivity of electromagnetically induced transparency to light-mediated interactions", which will be discussed in details over chapter 3.

In this work, we develop a new model taking into account light-mediated long-range interactions while considering two incident fields and a sample of three-level atoms. With this, we were able to study the changes in the EIT and CPT (coherent population trapping) phenomena, as well as the decrease in the efficiency of adiabatic population exchange by a STIRAP (stimulated Raman adiabatic passage) process, due to collective effects. The derivation of this new model opens doors for future studies of scattering in nonlinear optics.

In the meantime, Prof. Celso was contemplated with a collaboration project between Brazil and Sweden (CAPES-STINT), for a partnership with two very accomplished experimental groups from the University of Stockholm, led by Ana Predojević and Markus Hennrich. From this project came the opportunity of an exchange PhD, for which I am extremely grateful, especially to Celso, for the trust placed in me. From October 2019 to September 2020, I had the opportunity of working side by side with these two experimental groups, being responsible for the theory and numerical simulations related to the works developed during this period. It was an incredible experience. Everyone welcomed me with open arms and made me feel at home, also providing an excellent working environment, where I feel I have learnt a lot and developed myself professionally.

During my stay there, Celso and Romain Bachelard visited the University of Stockholm on a project-related work trip. During two weeks, we had the opportunity to have several face-to-face discussions that generated two main ideas for possible works,

both theoretical and experimental.

One of them arose from a discussion about the experimental system of coupled quantum dots, which are generally asymmetrical due to their production. Celso then had the idea of using this "technical issue" in favor of generating entangled states. In the work originating from this idea, we approached a system of two non-degenerate two-level systems coupled to a common bosonic mode. From there, we proposed two ways to generate entangled states in this system: in one of them, we produce an entangled steady state and in the other, we adiabatically transfer the population of the system to the entangled state. We believe that this is a versatile system and could be applied to a range of experimental platforms, and the dynamics and results can be easily interpreted with an EIT analogy. I would like to thank the authors of this work, which has been accepted by Physical Review A [2]: Gerard Higgings, Chi Zhang, Ana Predojević, Markus Hennrich, Romain Bachelard and Celso Jorge Villas-Bôas.

The second idea also emerged initially from a cavity EIT analogy, where the effective coupling of one of the transitions has an explicit dependence on the number of excitations of the field state. After much investigation into the feasibility of the proposal, the group led by Markus did an amazing job implementing the model in the trapped ions experiment and measuring in two ways, one destructive and one non-destructive, the Fock state of the phonon mode. I would like to thank the authors of this work: Marion Mallweger, Robin Thomm, Harry Parke, Natalia Kuk, Gerard Higgins, Romain Bachelard, Celso Jorge Villas-Bôas and Markus Hennrich.

This thesis is divided into four main parts. In the first part, we have a quick but fundamental theoretical background, presenting the basics of the interaction Hamiltonian and the EIT phenomenon in free space and in optical cavities. In the following three chapters, the three works mentioned above are presented, with each chapter having its own introduction and conclusions. Finally, we have an appendix presenting some details or accounts spared from the main text.

2 Theoretical background

The purpose of this chapter is to touch on some essential points for the understanding of the works that will be presented later. In it, we will address simple cases, indicating the essential steps to obtain the radiation-matter interaction Hamiltonian, as well as the system's dynamics considering incoherent processes, mentioning important steps, such as the approximations used and their respective validity. By the end, we should be able to understand the mechanisms behind EIT in free space and in cavities.

2.1 Jaynes-Cummings model

Let's start by studying one of the simplest systems of light-matter interaction, a two-level atom (or N non-interacting atoms), with ground state $|g\rangle$ and excited state $|e\rangle$, trapped inside an optical cavity. The atomic transition $|g\rangle \leftrightarrow |e\rangle$ is resonantly coupled by a single quantized electromagnetic mode with vacuum Rabi frequency g and frequency ω, as depicted in Fig.1.

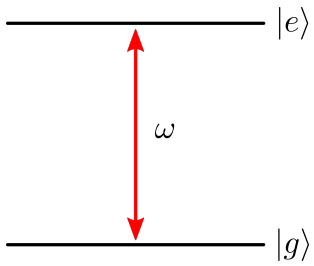

Figure 1 – Level scheme. A two-level atom, with ground and excited states $|g\rangle$ and $|e\rangle$, respectively, is coupled resonantly to a quantized mode of Rabi frequency g and frequency ω.

The total Hamiltonian that describes this system can be written as $\hat{H} = \hat{H}_0 + \hat{H}_{\text{int}}$, with

$$\hat{H}_0 = \omega_g \hat{\sigma}_{gg} + \omega_e \hat{\sigma}_{ee} + \omega \hat{a}^\dagger \hat{a}, \tag{2.1}$$

being the free energy Hamiltonian, considering $\hbar = 1$. The terms ω_n correspond to the respective frequency of atom's bare states, and $\hat{\sigma}_{nn} = |n\rangle\langle n|$ are the atomic population operators, for $n = e, g$. The operators $\hat{a}^\dagger$ and $\hat{a}$ are the creation and annihilation operators, respectively, acting on the mode.

The other part of the total Hamiltonian, $\hat{H}_{\text{int}}$, is where we effectively take into account the interaction between the atom and the field. Here, we will retain the description of the interaction to the dipole approximation, which is valid when the wavelength (λ)

of the incident radiation is much larger than the atomic dimensions ($\lambda \gg r_0$, being r_0 the atomic radius). In that case, we can consider the field uniform throughout atomic extension, and the interaction between the atom and the field can be written as

$$\hat{H}_{\text{int}} = -q_e \mathbf{r}.\hat{\mathbf{E}}, \tag{2.2}$$

where q_e is the electron charge, $\mathbf{r}$ is the electron's position vector and $\hat{\mathbf{E}}$ is the electromagnetic field operator. Doing some manipulation, we can rewrite part of this expression as

$$q_e \mathbf{r} = \sum_{n,m} q_e \left|n\right\rangle\!\left\langle n\right| \mathbf{r} \left|m\right\rangle\!\left\langle m\right| = \sum_{n,m} \mathbf{d}_{nm} \hat{\sigma}_{nm}, \tag{2.3}$$

being $\mathbf{d}_{nm} = q_e \langle n|\mathbf{r}|m\rangle$ the dipole matrix element of the transition $|g\rangle \leftrightarrow |e\rangle$, and $\hat{\sigma}_{nm} = |n\rangle\!\langle m|$ the raising/lowering atomic operator, for $n, m = e, g$ being $n \neq m$.

Next, we use the quantized electric field operator, calculated at the position of the atom in the dipole approximation [3]

$$\hat{\mathbf{E}} = \mathbf{E}_0 \left(\hat{a} + \hat{a}^\dagger\right), \tag{2.4}$$

where

$$\mathbf{E_0} = \sqrt{\frac{\omega}{2\epsilon_0 V}} \hat{\mathbf{k}}, \tag{2.5}$$

and V is the cavity volume, ϵ_0 is the electrical permittivity of the vacuum, and ω and $\hat{\mathbf{k}}$ are the frequency and unit vector of the electromagnetic field, respectively. Once more, $\hat{a}^\dagger$ and $\hat{a}$ represent the creation and annihilation operators, which act on the bosonic mode.

Finally, applying the rotating wave approximation (RWA), which is valid when the cavity mode and atomic transition frequencies are much higher than the atom-field coupling strength, i.e. $\omega \gg g$, we get

$$\hat{H}_{\text{int}} = g \left(\hat{a}\hat{\sigma}_{eg} + \hat{a}^\dagger \hat{\sigma}_{ge}\right), \tag{2.6}$$

where g is given by

$$g = -\sqrt{\frac{\omega}{2\epsilon_0 V}} \hat{\mathbf{k}}.\mathbf{d}_{ge}. \tag{2.7}$$

So, the total Hamiltonian describing this system reads

$$\hat{H} = \frac{\omega_0}{2}\hat{\sigma}_z + g\left(\hat{a}\hat{\sigma}_{eg} + \hat{a}^\dagger\hat{\sigma}_{ge}\right) + \omega\hat{a}\hat{a}^\dagger, \tag{2.8}$$

being the relative frequency $\omega_0 = (\omega_e - \omega_g)$ and the atomic operator $\hat{\sigma}_z = \hat{\sigma}_{ee} - \hat{\sigma}_{gg}$. The Hamiltonian from Eq. (2.8) is the so called Jaynes-Cummings Hamiltonian [4, 5]. It describes the coherent interaction between a qubit and a single quantized mode, being the basis for understanding the more complex models we are going to discuss.

2.2 Electromagnetically induced transparency

2.2.1 Model

Our goal here is to briefly discuss the fundamentals and mechanisms behind the electromagnetically induced transparency (EIT) phenomenon, which has already been substantially studied, in more detail, over the last decades [6]. The system that we will discuss in this section is composed of a three-level atom in a configuration of energy levels called Λ, as shown in Fig. 2, on which we shine two electromagnetic fields: a probe field of frequency ω_P coupling the transition $|1\rangle \leftrightarrow |3\rangle$ and Rabi frequency Ω_P, and a second field, which we will call the control field, coupling the other atomic transition $|2\rangle \leftrightarrow |3\rangle$ with frequency ω_c and Rabi frequency Ω_c.

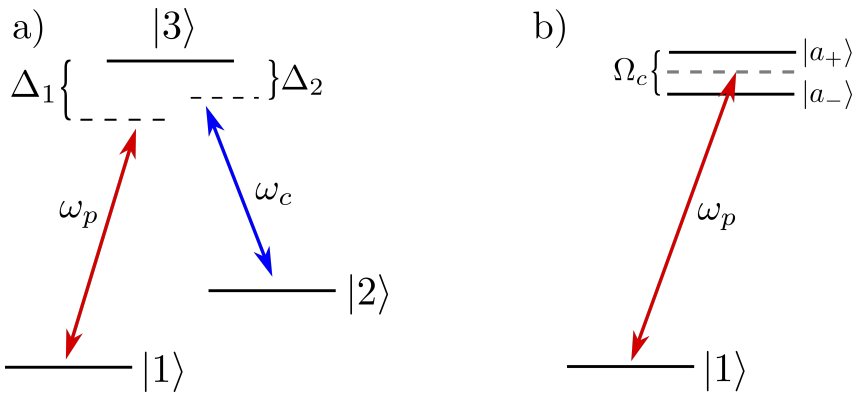

Figure 2 – Energy level diagrams. (a) Energy levels of a three-level atom in the Λ configuration in free space and in the presence of classical fields. (b) Effect of the control field on the atom, where the strong coupling of the transition $|2\rangle \leftrightarrow |3\rangle$ causes a splitting of $|3\rangle$ and $|2\rangle$ into two symmetric dressed states $|a_\pm\rangle$.

The Hamiltonian that describes this system can also be divided into two parts, such as $\hat{H} = \hat{H}_0 + \hat{H}_{\text{int}}$. The first one, $\hat{H}_0$ is a free Hamiltonian simply related to the energy levels of the bare atomic states, which can be written as

$$\hat{H}_0 = \omega_2 \hat{\sigma}_{22} + \omega_3 \hat{\sigma}_{33}, \tag{2.9}$$

where $\hat{\sigma}_{ii} = |i\rangle\langle i|$ are atomic operators, which give us information about the populations of the atomic states. Here, for simplicity, we assume $\hbar = 1$ and that the ground state $|1\rangle$ is at our zero energy. The second part, $\hat{H}_{\text{int}}$, describes the semi-classical interaction between two classic fields and the quantized atomic structure, given by

$$H_{\text{int}} = -\frac{\Omega_p}{2}\hat{\sigma}_{31}e^{-i\omega_p t} - \frac{\Omega_c}{2}\hat{\sigma}_{32}e^{-i\omega_c t} + H.c. \quad , \tag{2.10}$$

where $\hat{\sigma}_{ij} = |i\rangle\langle j|$ is the atomic raising/lowering operator, taking the system from $|j\rangle$ to $|i\rangle$ and $H.c.$ is the Hermitian conjugate.

For a better understanding of the system, it is convenient to go to the interaction representation. For this, we apply a unitary transformation $\hat{U}_0 = e^{-i\hat{H}_0 t}$ in the interaction Hamiltonian $\hat{H}_{\text{int}}$, resulting in

$$\hat{H}_I = -\frac{\Omega_p}{2}\hat{\sigma}_{31}e^{i\Delta_1 t} - \frac{\Omega_c}{2}\hat{\sigma}_{32}e^{i\Delta_2 t} - H.c. \quad , \tag{2.11}$$

where $\Delta_1 = \omega_3 - \omega_p$ and $\Delta_2 = \omega_3 - \omega_2 - \omega_c = \omega_{32} - \omega_c$.

In order to eliminate the time dependence in this Hamiltonian, we apply a second unitary transformation given by $U_1 = e^{i[\Delta_1\sigma_{33} - (\Delta_1 - \Delta_2)\sigma_{22}]t}$, so that

$$\hat{\tilde{H}}_I = \Delta_1\hat{\sigma}_{33} + (\Delta_1 - \Delta_2)\hat{\sigma}_{22} - \left(\frac{\Omega_p}{2}\hat{\sigma}_{31} + \frac{\Omega_c}{2}\hat{\sigma}_{32} + H.c\right). \tag{2.12}$$

2.2.2 Dark state

The time independent Hamiltonian in the interaction picture in Eq. (2.12) can also be written in its matrix form, for $\Delta = \Delta_1 = \Delta_2$, as

$$\hat{\tilde{H}}_I = -\frac{1}{2}\begin{pmatrix} 0 & 0 & \Omega_p \\ 0 & 0 & \Omega_c \\ \Omega_p & \Omega_c & -2\Delta \end{pmatrix}, \tag{2.13}$$

in the basis $b = \{|1\rangle, |2\rangle, |3\rangle\}$. Then, we can easily obtain the eigenenergies

$$\begin{aligned} E_0 =& 0, \\ E_\pm =& \frac{1}{2}\left[\Delta \pm \sqrt{\Delta^2 + \Omega_p^2 + \Omega_c^2}\right], \end{aligned} \tag{2.14}$$

and the respective eingenstates of the system

$$\begin{aligned} E_+ \rightarrow |a_+\rangle &= \sin(\theta)\sin(\phi)\,|1\rangle + \cos(\theta)\sin(\phi)\,|2\rangle + \cos(\phi)\,|3\rangle\,, \\ E_0 \rightarrow |a_0\rangle &= \cos(\theta)\,|1\rangle - \sin(\theta)\,|2\rangle\,, \\ E_- \rightarrow |a_-\rangle &= \sin(\theta)\cos(\phi)\,|1\rangle + \cos(\theta)\cos(\phi)\,|2\rangle - \sin(\phi)\,|3\rangle\,, \end{aligned} \tag{2.15}$$

being

$$\begin{aligned} \tan(\theta) =& \frac{\Omega_p}{\Omega_c}, \\ \tan(2\phi) =& \frac{\sqrt{\Omega_p^2 + \Omega_c^2}}{\Delta}. \end{aligned} \tag{2.16}$$

It is worth noting that the eigenstate $|a_0\rangle$ from Eq. (2.15), which has eigenenergy $E_0 = 0$, for any regime of Ω_c and Ω_p, is written solely in terms of the bare fundamental states $|1\rangle$ and $|2\rangle$, with no component related to the excited state $|3\rangle$. This means that if the system is in the $|a_0\rangle$ state the probability of emission or absorption is zero, so this

state is called the dark state. The other two symmetric eigenstates $|a_\pm\rangle$ are often called Autler-Townes doublet.

Next, we can proceed with an analysis where we consider two different parameter regimes, comparing the intensities of the classical fields Ω_P and Ω_c. When $|\Omega_P| \approx |\Omega_c|$ we are in the coherent population trapping (CPT) regime while when $|\Omega_P| \ll |\Omega_c|$ we are working in the EIT regime.

In the CPT regime, on resonance ($\Delta \to 0$), we have $\tan\theta \approx 1$, i.e, $\sin\theta \approx \cos\theta$, being $\theta \approx \pi/4$ and $\tan(2\phi) \to \infty$, in a way that $\phi = \pi/4$. Thus, the eigenstates become

$$\begin{aligned} |a_0\rangle =& \frac{1}{\sqrt{2}}\left(|1\rangle + |2\rangle\right), \\ |a_\pm\rangle =& \frac{1}{\sqrt{2}}\left[\frac{1}{\sqrt{2}}\left(|1\rangle + |2\rangle\right) \pm |3\rangle\right]. \end{aligned} \tag{2.17}$$

Now, in a resonant case of the EIT regime, we have $\tan(\theta) \approx 0$ and $\tan(2\phi) \to \infty$, resulting in

$$\begin{aligned} |a_0\rangle =& |1\rangle, \\ |a_\pm\rangle =& \frac{1}{\sqrt{2}}\left(|2\rangle \pm |3\rangle\right). \end{aligned} \tag{2.18}$$

Note that when the control field is very strong, the system is driven to the ground state $|1\rangle$, which is exactly the dark state when $\Delta \approx 0$. As discussed before, this state does not absorb or emit photons, so the system is transparent to the radiation around the resonance. It is also worth mentioning that in the EIT regime next to the resonance, the eigenenergies of $|a_\pm\rangle$ (dressed states), are equal to $E_\pm = \pm\Omega_c/2$, where the absorption maxima are, which means that the a strong control field coupling the transition $|1\rangle \leftrightarrow |3\rangle$ gives rise to an energy splitting proportional to its Rabi frequency, i.e, $E_+ - E_- = \Omega_c$.

2.2.3 Optical response

The macroscopic polarization of a medium can be approximated to a linear response to an external electromagnetic field, as

$$\mathbf{P} = \chi_e \mathbf{E}, \tag{2.19}$$

being χ_e the linear electrical susceptibility coefficient. Once we obtain an expression for this coefficient, we will be able to analyse the absorption and refractive index behaviors of the atomic medium through its imaginary and real parts, respectively [6].

In terms of the dipole moments d, the expectation value of the polarization reads

$$\langle P\rangle = \sum_{i=1}^{N} \frac{\langle d\rangle}{V} = \frac{N}{V}\,\mathrm{Tr}(\hat{\rho}d), \tag{2.20}$$

where N is the number of atoms in the sample contained inside a volume V, and $\hat{\rho}$ is the density matrix of the system, which can be written in a general form as

$$\begin{aligned}\hat{\rho} &= \hat{\rho}_{11}\hat{\sigma}_{11} + \hat{\rho}_{22}\hat{\sigma}_{22} + \hat{\rho}_{33}\hat{\sigma}_{33} \\ &+\Big(\hat{\rho}_{21}e^{-i\omega_{21}t}\hat{\sigma}_{21} + \hat{\rho}_{31}e^{-i\omega_{31}t}\hat{\sigma}_{31} + \hat{\rho}_{32}e^{-i\omega_{32}t}\hat{\sigma}_{32} + H.c.\Big) \quad . \end{aligned} \tag{2.21}$$

Given that the only dipole allowed transitions are $|1\rangle \leftrightarrow |3\rangle$ and $|2\rangle \leftrightarrow |3\rangle$, Eq. (2.20) becomes

$$\langle P\rangle = \frac{N}{V}\Big(d_{13}\rho_{31}e^{-i\omega_{31}t} + \mu_{23}\rho_{32}e^{-i\omega_{32}t} + H.c.\Big). \tag{2.22}$$

To continue our analysis, we must find an expression for each density matrix element in the steady state, i.e., for $\dot{\hat{\rho}} = 0$. The system's dynamics is obtained using a master equation [7], which is derived under some approximations that can be summarized in physical arguments as:

- Initial separability: there can be no correlation between the system and environment at $t = 0$, which means that the total density matrix can be written as a tensor product such as $\hat{\rho}_{\text{tot}}(0) = \hat{\rho}_{\text{sys}}(0) \otimes \hat{\rho}_{\text{env}}(0)$;
- Born approximation: assumes a weak coupling between the system and the environment, in a way that the environment state will not change due to the interaction with the system and the total density matrix remains separable thought the evolution time, i.e, $\hat{\rho}_{\text{tot}} = \hat{\rho}_{\text{sys}} \otimes \hat{\rho}_{\text{env}}$;
- Markov approximation: often refereed to as "short-memory environment", which assumes that the environment's correlation time is much shorter than the relevant system time scale;
- Zero temperature: assumes that the temperature is at $T = 0$K, which can be a reasonable approximation if we are working in the optical regime, where the mean number of thermal photons is negligible.

The master equation considers, besides the coherent evolution, the dissipative terms of the system, such as the spontaneous decay rate Γ_{ij} from the level $|i\rangle$ to the $|j\rangle$ and the dephasing rate γ_i related to the atomic state $|i\rangle$. The master equation we are using in this case reads

$$\begin{aligned}\frac{d\hat{\rho}}{dt} =& -i[\hat{\tilde{H}}, \hat{\rho}] + \sum_{l=1,2}\frac{\Gamma_{3l}}{2}\left(2\hat{\sigma}_{l3}\hat{\rho}\hat{\sigma}_{3l} - \hat{\sigma}_{33}\hat{\rho} - \hat{\rho}\hat{\sigma}_{33}\right) \\ &+ \sum_{j=2,3}\frac{\gamma_j}{2}\left(2\hat{\sigma}_{jj}\hat{\rho}\hat{\sigma}_{jj} - \hat{\sigma}_{jj}\hat{\rho} - \hat{\rho}\hat{\sigma}_{jj}\right). \end{aligned} \tag{2.23}$$

Calculating every element $\dot{\rho}_{ij} = \langle i|\dot{\hat{\rho}}|j\rangle$ for $i, j = 1, 2, 3$, and setting them individually to zero, we end up with an algebraic system of equations, which we can solve for the

steady state density matrix elements. In the EIT regime, i.e., considering $\Omega_c \gg \Omega_p$, all the population is asymptotically driven to the dark state $|a_0\rangle = |1\rangle$, making $\rho_{11} \approx 1$ and $\rho_{22} = \rho_{33} \approx 0$ good approximations for this regime. After some manipulation, we end up with

$$\rho_{31} \approx \frac{i\Omega_p(\gamma_{21} - 2i(\Delta_2 - \Delta_1))e^{i\Delta_1 t}}{(2i\Delta_1 + \gamma_{31})[\gamma_{21} - 2i(\Delta_2 - \Delta_1)] + \Omega_c^2}, \tag{2.24}$$

$$\rho_{32} \approx \frac{-i\Omega_p^2\Omega_c e^{i\Delta_2 t}}{(2i\Delta_2 + \gamma_{32})(-2i\Delta_1 + \gamma_{31})[\gamma_{21} + 2i(\Delta_2 - \Delta_1)] + \Omega_c^2}, \tag{2.25}$$

where $\gamma_{31} = \Gamma + \gamma_1$, $\gamma_{32} = \Gamma + \gamma_2 + \gamma_3$, and $\gamma_{21} = \gamma_2$, with $\Gamma = \Gamma_{31} + \Gamma_{32}$ being the total spontaneous decay rate from the excited state.

Substituting the results of Eqs. (2.24) and (2.25) into Eq. (2.22), we can rewrite the polarization as

$$\begin{aligned}\langle P\rangle \approx & \frac{N}{V}\frac{i\mu_{13}\Omega_p(\gamma_{21} - 2i\delta)e^{i\omega_p t}}{(2i\Delta + \gamma_{31})[\gamma_{21} - 2i\delta] + \Omega_c^2} \\ & + \frac{N}{V}\frac{-i\mu_{23}\Omega_p^2\Omega_c e^{i\omega_c t}}{(2i(\Delta - \delta) + \gamma_{32})(-2i\Delta + \gamma_{31})[\gamma_{21} + 2i\delta] + \Omega_c^2} + H.c. \quad ,\end{aligned} \tag{2.26}$$

where we have defined $\Delta = \Delta_1$ and $\delta = \Delta_2 - \Delta_1$. According to Eq. (2.19), if we consider the total electric field to be the sum of the probe and control fields, i.e., $\mathbf{E} = \mathbf{E_p}e^{-i\omega_p t} + \mathbf{E_c}e^{-i\omega_c t}$, the linear optical response term related to the probe field should be proportional to the oscillating term $e^{\pm i\omega_p t}$. Thus, defining $\Omega_p = d_{13}E_p/\epsilon_0$, the linear electrical susceptibility reads

$$\chi_e = \frac{|d_{13}|^2 N}{\epsilon_0 V}\frac{i(\gamma_{21} - 2i\delta)e^{i\omega_p t}}{(2i\Delta + \gamma_{31})[\gamma_{21} - 2i\delta] + \Omega_c^2}. \tag{2.27}$$

Figure 3, shows the effect of the control field in a three-level system within the EIT regime, where we can clearly see the drastic change in the optical properties caused by the EIT phenomenon, especially around the resonance. In the absorption spectrum, Fig. 3(a), we see a transparency window for the three-level system where in the two-level case we had maximum absorption.

EIT is a quantum interference phenomenon between the excitation paths of the system, and although it is defined in a regime where $\Omega_c \gg \Omega_p$, as mentioned before, this is a necessary but not sufficient condition. In addition, we must also take into account the width of the excited level, so that if we have $\Omega_c \gg \Gamma_3$, the absorption spectrum observed in an analyse similar to Fig.2 would simply be the absorption spectrum of an Autler-Townes process.

Figure 3(b) shows the dispersion spectrum, where we observe, instead of a smooth curve, an abrupt variation of the refractive index. It is because of this steep derivative, for example, that we are able to observe a reduction in the group velocity of light propagating

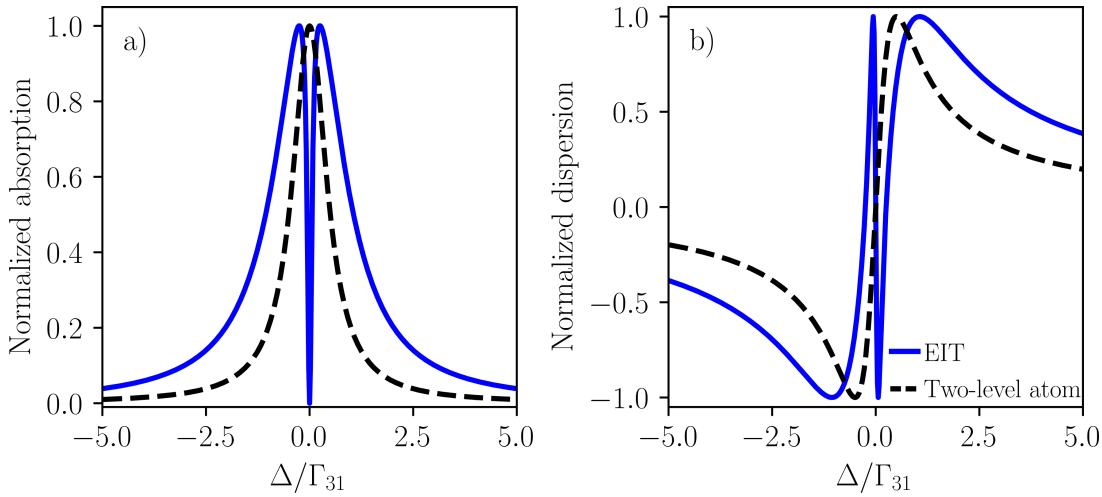

Figure 3 – Optical response. a) Normalized absorption as a function of the detuning for a two-level atom and a three-level atom in the EIT regime. b) Refraction index of a two-level atom and a three-level atom in the EIT regime. The black dashed curves refer to the two-level system atom while the blue filled ones to the three-level system. The system parameters were set to $\Omega_p = \Gamma_{31}/50$, $\gamma_2 = \gamma_3 = 0$. For the 2-level atom curves the additional parameters were set to $\Gamma_{32} = 0$ and $\Omega_c = 0$. For the 3-level atom EIT curves these parameters were chosen as $\Gamma_{32} = \Gamma_{31}$ and $\Omega_c = \Gamma_{31}/5$.

in an EIT medium [8]. This is the building block for a wide range of applications such as EIT based quantum memories [9, 10, 11].

2.2.4 Exact solution for the steady state

While obtaining the steady state solution, we assumed that $\Omega_c \gg \Omega_p$(EIT regime), which enabled us to make the approximations $\rho_{11} \approx 1$ and $\rho_{22} = \rho_{33} \approx 0$ and solve the problem in a simple way. However, we are also able to obtain an exact solution to the problem, i.e., the system of algebraic equations that arise from solving Eq. 2.23 in the steady state ($\dot{\hat{\rho}} = 0$), for any parameter regime. Despite the extensive and complicated expressions for the ρ_{ij}, the expressions for the optical susceptibilities of order $n = 1, 3$ and 5, with $\gamma_2 = \gamma_3 = \Delta_2 = 0$ are given by [12]

$$\chi_e^{(1)} = \frac{2\Delta}{2\Delta\left(2\Delta - i\Gamma\right) - \Omega_c^2}, \tag{2.28}$$

$$\chi_e^{(3)} = \frac{4\Delta^2\left(\frac{\Gamma^2\Gamma_{32}}{\Omega_c^2} - i\frac{\Gamma\Gamma_{32}}{2\Delta} + 3\Gamma - \Gamma_{31} + \frac{\Gamma_{31}\Omega_c^2}{2\Delta^2}\right)}{\Gamma_{31}\left(\Omega_c^2 - 2i\Delta\Gamma - 4\Delta^2\right)\left(\Omega_c^2 + 2i\Delta\Gamma - 4\Delta^2\right)^2}, \tag{2.29}$$

$$\chi_e^{(5)} = \frac{2\Delta\left(\frac{-16\Gamma^4\Gamma_{32}^2\Delta^4}{\Omega_c^4} + \frac{8\Gamma^2\Gamma_{32}\Delta^3}{\Omega_c^2}A + 4\Delta^2 B + 2\Delta C\Omega_c^2 - 3\Gamma_{31}^2\Omega_c^4\right)}{\Gamma_{31}^2\left(-2i\Gamma\Delta - 4\Delta^2 + \Omega_c^2\right)^2\left(2i\Gamma\Delta - 4\Delta^2 + \Omega_c^2\right)^3}, \tag{2.30}$$

with

$$A = (i\Gamma\Gamma_{32} - 10\Gamma\Delta + 2\Gamma_{31}\Delta) \tag{2.31}$$

$$B = \Gamma^2\left(\Gamma_{31}^2 - 2\Gamma_{31}\Gamma_{32} - \Gamma_{32}^2\right) + 4\Delta^2\left(-6\Gamma^2 + 3\Gamma\Gamma_{31} + \Gamma_{31}\Gamma_{32}\right) + 4i\Gamma^2\Gamma_{32}\Delta, \tag{2.32}$$

$$C = -2\Delta(3\Gamma(\Gamma + 3\Gamma_{31}) + \Gamma_{31}(\Gamma_{32} - 2\Gamma_{31})) + i\Gamma\Gamma_{32}(\Gamma + \Gamma_{31}). \tag{2.33}$$

2.3 Cavity electromagnetically induced transparency

2.3.1 Model

For this section, let us consider a system composed by a three-level atom trapped inside an optical cavity. The atom is in a Λ-level configuration, just like the one studied in the previous section, with two ground states $|1\rangle$ and $|2\rangle$, and an excited state $|3\rangle$, as represented in Figure 4. The transition $|1\rangle \leftrightarrow |3\rangle$ is coupled by the quantized mode of radiation inside the cavity with vacuum Rabi frequency $2g$ and frequency ω, while the second transition $|2\rangle \leftrightarrow |3\rangle$ is coupled by a classical control field with Rabi frequency $2\Omega_c$ and frequency ω_c. In addition, we have a probe field with strength ε and frequency ω_p injecting energy into the cavity mode.

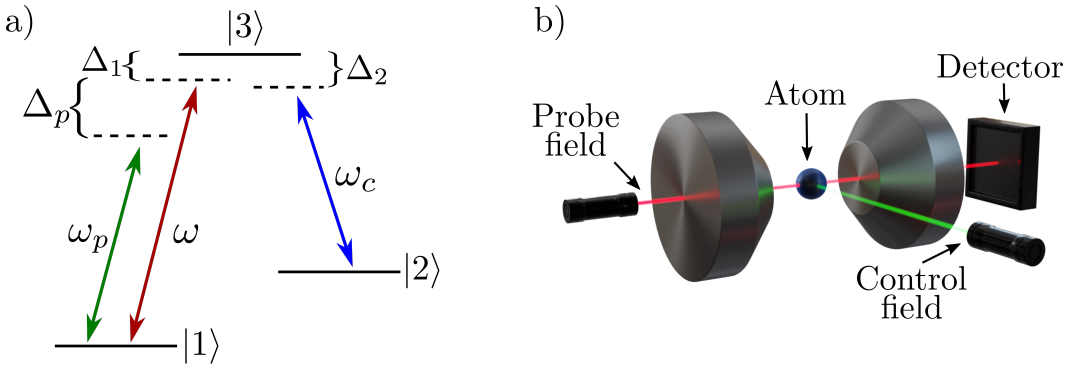

Figure 4 – (a) Level scheme of a three-level atom in a Λ configuration trapped inside an optical cavity. A classical control field with frequency ω_c and Rabi frequency $2\Omega_c$, couples one of the atomic transitions. The other atomic transition is coupled by the cavity mode of frequency ω and vacuum Rabi frequency $2g$. We also consider a probe field with strength ε and frequency ω_P. (b) Pictorial representation of the experimental observation of the EIT phenomenon with a probe and a control fields, both focusing on a trapped atom inside a linear optical cavity, and a properly positioned detector, in order to measure the transmission.

The process for obtaining the total Hamiltonian of this system is very similar to what we have been doing for the last sections, in a sense that it can also be written as a sum of the free Hamiltonian given by

$$\hat{H}_0 = \omega_3\hat{\sigma}_{33} + \omega_2\hat{\sigma}_{22} + \omega\hat{a}^\dagger\hat{a}, \tag{2.34}$$

which refers to the free energy of the atomic states and the electromagnetic field, very similar to Eq. 2.1, where we are considering an energy in which the ground state $|1\rangle$ is at zero energy.

Since we have both quantum and classical fields in the system, it is convenient to calculate the interaction of each one with the atom separately. For the interaction Hamiltonian of the classical control field, which we will call $H_{\text{int}}^{\text{class}}$, we assume that the control field can be written in an oscillatory manner as $\mathbf{E}(t) = \mathbf{E}_0 \cos(\omega_c t)$ and that it only couples the transition $|2\rangle \leftrightarrow |3\rangle$. Thus

$$H_{\text{int}}^{\text{class}} = \Omega_c(\hat{\sigma}_{32}e^{-i\omega_c t} + \hat{\sigma}_{23}e^{i\omega_c t}), \tag{2.35}$$

where $\Omega_c = \mathbf{d}_{23}.\mathbf{E}_0$ the Rabi frequency coupling the respective transition with the dipole matrix element $\mathbf{d}_{23}$. It is worth mentioning that here we used the rotating wave approximation (RWA), which is valid when $\omega_c \gg \Omega_c$.

On the other hand, the other part of the interaction Hamiltonian, referring to the quantized mode interacting with the transition $|1\rangle \leftrightarrow |3\rangle$, which we will call $H_{\text{int}}^{\text{quan}}$, is given by

$$\hat{H}_{\text{int}}^{quan} = g\left(\hat{a}\hat{\sigma}_{31} + \hat{a}^\dagger\hat{\sigma}_{13}\right), \tag{2.36}$$

just like the interaction in Eq. 2.6.

Finally, the Hamiltonian of the probe field H_p, in the rotating wave approximation (valid for $\omega_p \gg \varepsilon$), contributes to the total Hamiltonian as

$$\hat{H}_p = \varepsilon(\hat{a}e^{i\omega_p t} + \hat{a}^\dagger e^{-i\omega_p t}). \tag{2.37}$$

Therefore,substituting these expressions in the total Hamiltonian

$$\hat{H} = \hat{H}_0 + \hat{H}_{\text{int}}^{\text{class}} + \hat{H}_{\text{int}}^{\text{quan}+\hat{H}_p}, \tag{2.38}$$

and applying the consecutive unitary transformations $\hat{U}_0 = e^{-i\hat{H}_0 t}$ and $\hat{U}_1 = e^{-i\hat{H}_1 t}$, with $\hat{H}_1 = -\Delta_1\hat{\sigma}_{33} - (\Delta_1 - \Delta_2)\,\hat{\sigma}_{22} - \Delta_P\hat{\sigma}_{11} + \Delta_P\hat{a}^\dagger\hat{a}$ we end up with the time-independent Hamiltonian in the interaction picture

$$\hat{H}_I = \Delta_1\hat{\sigma}_{33} + (\Delta_1 - \Delta_2)\hat{\sigma}_{22} + \Delta_P\hat{\sigma}_{11} - \Delta_P\hat{a}^\dagger\hat{a} + (g\hat{a}\hat{\sigma}_{31} + \Omega_c\hat{\sigma}_{32} + \varepsilon\hat{a} + H.c.)\,, \tag{2.39}$$

where $\Delta_1 = \omega_3 - \omega$ and $\Delta_2 = (\omega_3 - \omega_2) - \omega_c$ are the detunings between the atomic transition frequencies and the respective fields and $\Delta_P = \omega - \omega_P$ the detuning between the cavity mode and the probe field frequencies.

2.3.2 Dark state

The Hamiltonian in Eq. (2.39) can be written in a matrix form in the complete basis $b = \{|1,n\rangle\,, |2,n-1\rangle\,, |3,n-1\rangle\}$, where $|j,m\rangle = |j\rangle \otimes |m\rangle$ for $j = 1,2,3$ and $|m\rangle$

being the cavity mode Fock state with m photons. In the absence of a probe field and considering complete resonance, i.e., $\varepsilon = 0$ and $\Delta_1 = \Delta_2 = \Delta_p = 0$, this Hamiltonian reads

$$\hat{H}_I = \begin{pmatrix} 0 & 0 & g\sqrt{n} \\ 0 & 0 & \Omega_c \\ g\sqrt{n} & \Omega_c & 0 \end{pmatrix}, \tag{2.40}$$

which, in turn, have three eigenenergies

$$\begin{aligned} E_0 =& 0, \\ E_\pm =& \pm\sqrt{ng^2 + \Omega_c^2}, \end{aligned} \tag{2.41}$$

with their respective eingenstates being

$$\begin{aligned} E_0 \to |a_0\rangle &= \mathcal{N}_0\left(|1,n\rangle - \frac{g\sqrt{n}}{\Omega_c}|2,n-1\rangle\right), \\ E_\pm \to |a_\pm\rangle &= \mathcal{N}_\pm\left[\pm\left(\frac{g\sqrt{n}}{\sqrt{ng^2+\Omega_c^2}}|1,n\rangle + \frac{\Omega_c}{\sqrt{ng^2+\Omega_c^2}}|2,n-1\rangle\right) + |3,n-1\rangle\right], \end{aligned} \tag{2.42}$$

where $\mathcal{N}_0$ and $\mathcal{N}_\pm$ are normalization constants.

Proceeding to an analysis for the different parameter regimes, like in the previous section, we now define the cavity coherent population trapping (CCPT) regime as $\Omega_c \sim g\sqrt{n}$ and the cavity electromagnetically induced transparency (CEIT) regime as $\Omega_c \gg g\sqrt{n}$.

The eigenstates for the CCPT regime are almost identical of those in the previous section

$$\begin{aligned} |a_0\rangle &= \frac{1}{\sqrt{2}}(|1,n\rangle - |2,n-1\rangle), \\ |a_\pm\rangle &= \frac{1}{\sqrt{2}}\left[\pm\frac{1}{\sqrt{2}}(|1,n\rangle + |2,n-1\rangle) + |3,n-1\rangle\right], \end{aligned} \tag{2.43}$$

where the dark state remains a superposition of the ground states.

The same occurs for the CEIT regime, where the eigenstates can be written as

$$\begin{aligned} |a_0\rangle &= |1,n\rangle\,, \\ |a_\pm\rangle &= \frac{1}{\sqrt{2}}(|3,n-1\rangle \pm |2,n-1\rangle), \end{aligned} \tag{2.44}$$

which are completely analogous to those obtained for the free space setup. The darkstate continues to have only a component in the ground atomic state $|1\rangle$, and the Autler-Townes doublet remains a superposition of the atomic states $|2\rangle$ and $|3\rangle$, being energetically separated by $E_+ - E_- = 2\Omega_c$. However, despite all the similarities, it is important to note that by exchanging a free-space probe field by a quantized cavity mode, we give rise to an effective coupling, between $|1,n\rangle$ and $|3,n-1\rangle$, that directly depends on the cavity mode Fock state excitation number $g_{\text{eff}} = \sqrt{ng^2 + \Omega_c^2}$. It is from this explicit dependence that came the initial idea for the proposal of a Fock state detector, used in the work presented in section 5.

2.3.3 Transmission

The dynamics of this system, including dissipation, is obtained through the following master equation

$$\begin{aligned}\frac{d\hat{\rho}}{dt} =& -i[\hat{H}_I, \hat{\rho}] + \frac{\kappa}{2}\left(2\hat{a}\hat{\rho}\hat{a}^\dagger - \hat{a}^\dagger\hat{a}\hat{\rho} - \hat{\rho}\hat{a}^\dagger\hat{a}\right) \\ &+ \sum_{k=1}^{N}\sum_{l=1,2}\frac{\Gamma_{3l}}{2}\left(2\hat{\sigma}_{l3}^{(k)}\hat{\rho}\hat{\sigma}_{3l}^{(k)} - \hat{\sigma}_{33}^{(k)}\hat{\rho} - \hat{\rho}\hat{\sigma}_{33}^{(k)}\right) \\ &+ \sum_{k=1}^{N}\sum_{j=2,3}\frac{\gamma_j}{2}\left(2\hat{\sigma}_{jj}^{(k)}\hat{\rho}\hat{\sigma}_{jj}^{(k)} - \hat{\sigma}_{jj}^{(k)}\hat{\rho} - \hat{\rho}\hat{\sigma}_{jj}^{(k)}\right), \end{aligned} \tag{2.45}$$

where Γ_{3l} is the spontaneous decay rate from the excited state $|3\rangle$ to the ground state $|l\rangle$ for $l = 1, 2$ and γ_j is the dephasing of the level $|j\rangle$, for $j = 2, 3$.

The transmission spectrum of the probe field is proportional to the expected mean number of photons inside the cavity, so that the normalized transmission can be defined here as $T = \left\langle \hat{a}^\dagger\hat{a} \right\rangle / |2\varepsilon/\kappa|^2$.

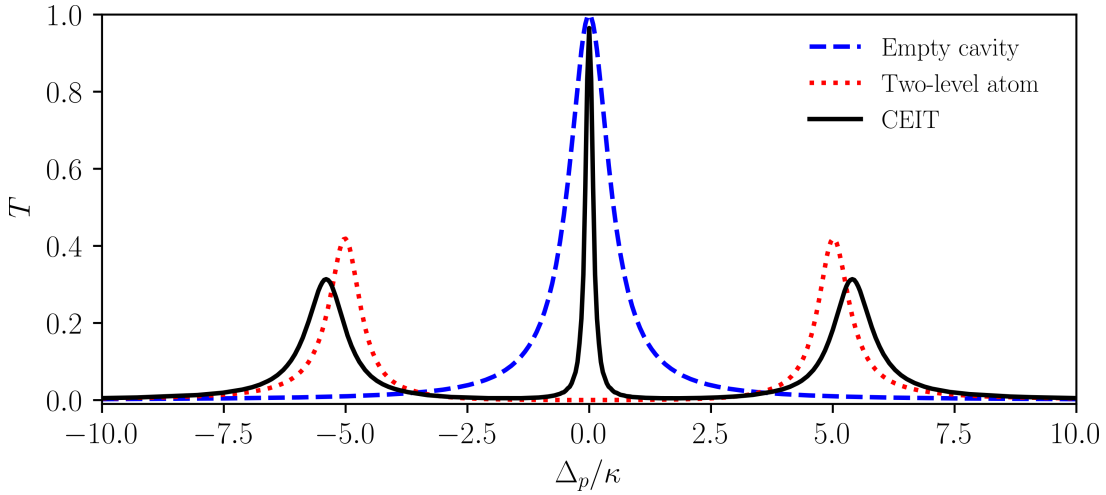

Figure 5 – Transmission spectrum. The dashed blue curve represents the empty cavity situation, with maximum transparency at $\Delta_p = 0$ and FWHM $= \kappa$. The dotted red curve refers to the case of a two-level atom inside the cavity, with transmission peaks located exactly at $\Delta_p = \pm g$. The solid black curve shows the CEIT transmission spectrum with maximum transparency at resonance, just like the empty cavity, but with much narrower FWHM. It is also possible to observe peripheral peaks, which appear at the Autler-Townes doublet resonance at $\Delta_p = \pm\sqrt{g^2 + \Omega_c^2}$. CEIT parameters: $g = 5\kappa$, $\Omega_c = 2\kappa$, $\varepsilon = \sqrt{0.01}\kappa$, $\Delta_1 = \Delta_2 = 0$ and $\Gamma_{31} = \Gamma_{32} = 0.5\kappa$. For the empty cavity curve $\Omega_c = 0$, and for the two-level atom $\Omega_c = 0$ and $\Gamma_{32} = 0$.

The steady-state transmission, calculated numerically through Eq. (2.45) for $\dot{\hat{\rho}} = 0$, can be seen in Fig.5. The CEIT system, just like the empty cavity, presents a maximum at resonance, however, with a much narrower transmission windows full width at half maximum (FWHM) [13, 14]. In addition to the central transparency window, it also

has two peripheral peaks, which are resonant to the Autler-Townes doublet around $\Delta_p = \pm\sqrt{g^2 + \Omega_c^2}$.

3 Sensitivity of electromagnetically induced transparency to light-mediated interactions

3.1 Introduction

Electromagnetically Induced Transparency (EIT) [15] is a quantum interference phenomenon in which an initially opaque ensemble of three-level atoms becomes transparent to a probe field due to the influence of a second field, known as the control field. The existence of a dark state in the atomic system is the reason why the absorption ceases when the probe field is tuned at resonance with a given atomic transition. In particular, when probe and control fields are of the same magnitude, such a dark state becomes a superposition of two atomic ground states, which gives origin to a Coherent Population Trapping (CPT) in the steady-state regime [16, 17].

EIT and CPT phenomena have been receiving substantial attention thanks to their vast list of applications [6]. For example, EIT is useful for the reduction of the group velocity of a light pulse which propagates through an atomic medium [8], for the narrowing of the transmission linewidth of optical cavities [13, 14], and for quantum memory implementations, where photonic states can be mapped and stored in single atoms trapped inside optical cavities [9, 10], or in an atomic ensemble [11]. For the latter, it has been theoretically demonstrated that the efficiency of quantum memory devices increases with the sample optical thickness [18, 19]. Indeed high efficiency ($> 90\%$) in retrieving quantum information has been achieved in cold-atom platforms only for high optical thickness [20, 21, 22], a regime where multiple scattering of light becomes relevant. This leads us to the unexplored question of how coherent collective scattering of light would affect EIT and CPT transparency windows and, consequently, all corresponding applications. The purpose of the present letter is to shine a light on this question.

In light scattering by cold atoms, effective light-mediated interactions emerge between all scatterers [23, 24, 25] owing to a strong suppression of the Doppler broadening by laser cooling techniques. Such optical dipole-dipole interactions give origin to several collective effects, such as superradiance [26, 27, 28], subradiance [29, 30, 31, 32, 33], coherent backscattering of light [34, 35], and cooperative Lamb shifts [36, 28], and cover long ranges in a similar fashion as Rydberg atomic interactions. Yet Rydberg interactions are Hamiltonian interactions that do not depend on light scattering to remain active, being even able to totally destroy EIT [37, 38, 39, 40]. On the other hand, light-mediated interactions are a consequence of the collective scattering of light in the atomic sample, so that any population of a dark state naturally reduces the atomic cooperation to some extent.

This is the reason why purely optical interactions should induce more subtle modifications in transparency windows, and it is not clear yet to which extent the EIT/CPT applications are affected.

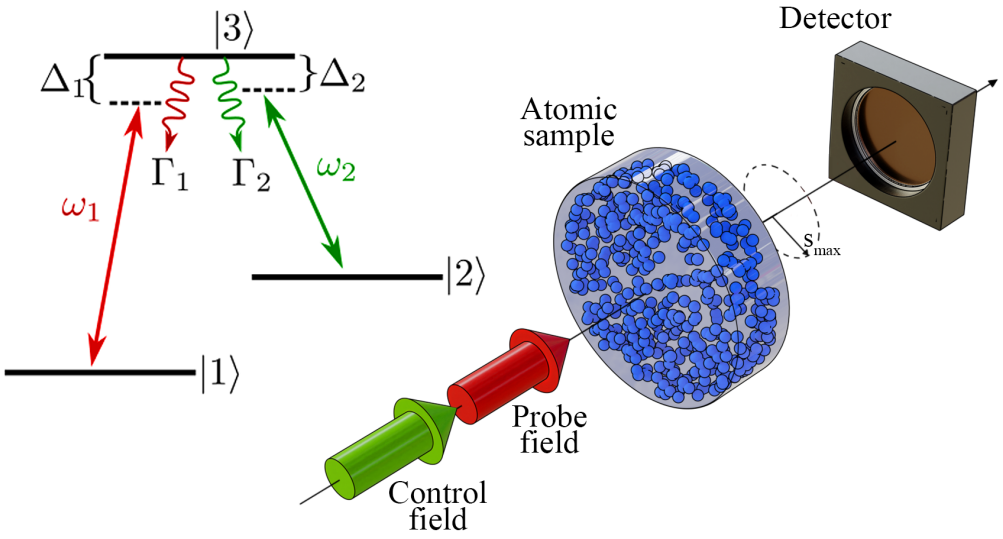

Figure 6 – A cylindrical and homogeneous cold cloud of N disordered three-level atoms scatters probe and control fields to the free space. The atomic levels are in a Λ configuration, as schematically shown on the left. The radius R of the cylindrical surface is much larger than its thickness L, measuring the probe field transmission in a disk of radius $s_{\max} < R$. Taken from Ref. [1].

In order to detect collective modifications on EIT/CPT phenomena, here we derive a microscopic coupled-dipole model that describes the multiple scattering of probe and control fields by cold ensembles of three-level atoms. Such a model represents a significant extension of the linear-optics coupled-dipole model [23, 24, 25, 41]. In the limit where polarization effects can be neglected, namely the dilute regime, we show that light-mediated interactions narrow the width of the transparency window at its Full Width at Half Maximum (FWHM). Furthermore, we analyse the Stimulated Raman Adiabatic Passage (STIRAP) to get a prospect of the multiple scattering effect on the fore-mentioned quantum memory applications. This EIT-based dynamical technique is a fundamental ingredient in writing and retrieving protocols for quantum memories [42]. While considering a complete vectorial description, we demonstrate that the efficiency of such a STIRAP process, in which the population is exchanged between the two ground states of the Λ-system, is substantially reduced by collective scattering of light even in the dilute regime. As our model combines long-range interactions mediated by light with two distinct incident fields, it opens a new route for the study of collective effects in nonlinear optics.

3.2 Microscopic model

We consider an ensemble of N point-like three-level atoms at zero temperature, with random positions $\mathbf{r}_j = (x_j, y_j, z_j)$, for $j = 1, ..., N$, decaying to the vacuum modes of the radiation field. Their Λ energy-level scheme is composed of two ground states, $|1\rangle$ and $|2\rangle$, and one excited state $|3\rangle$, as represented in Fig. 6. A probe field, of angular frequency ω_1 and Rabi frequency Ω_1, pumps the transition $|1\rangle \leftrightarrow |3\rangle$, of frequency ω_{31}, whereas a control field, of angular frequency ω_2 and Rabi frequency Ω_2, drives the transition $|2\rangle \leftrightarrow |3\rangle$, of frequency ω_{32}. Both fields are plane waves propagating in the direction of the wave vectors $\mathbf{k}_1$ and $\mathbf{k}_2$, respectively. The light-matter Hamiltonian that describes this system reads ($\hbar = 1$):

$$\begin{aligned}\hat{H} &= \sum_{\mathbf{k},\mathbf{s}} \nu_{\mathbf{k}} \left(\hat{a}^{\dagger}_{\mathbf{k},\mathbf{s}} \hat{a}_{\mathbf{k},\mathbf{s}} + \frac{1}{2}\right) + \sum_{j=1}^{N} \left[\sum_{n=1}^{3} \omega_{nn} \hat{\sigma}^{j}_{nn} \right. \\ &+ \sum_{n=1}^{2} \sum_{\mathbf{k},\mathbf{s}} g^{(n)}_{\mathbf{k},\mathbf{s}} \left(\hat{\sigma}^{j}_{n3} + \hat{\sigma}^{j}_{3n}\right) \left(\hat{a}^{\dagger}_{\mathbf{k},\mathbf{s}} e^{-i\mathbf{k}\cdot\mathbf{r}_j} + \hat{a}_{\mathbf{k},\mathbf{s}} e^{i\mathbf{k}\cdot\mathbf{r}_j}\right) \\ &\left. + \sum_{n=1}^{2} \frac{\Omega_n}{2} \left(\hat{\sigma}^{j}_{n3} e^{i\omega_n t - i\mathbf{k}_n\cdot\mathbf{r}_j} + \hat{\sigma}^{j}_{3n} e^{-i\omega_n t + i\mathbf{k}_n\cdot\mathbf{r}_j}\right)\right], \end{aligned} \tag{3.1}$$

where $\hat{\sigma}^{j}_{n3} = |n\rangle\langle 3|^j$ ($\hat{\sigma}^{j}_{3n} = |3\rangle\langle n|^j$) are the lowering (raising) atomic operators, and $\hat{\sigma}^{j}_{nn} = |n\rangle\langle n|^j$ are the atomic population operators. Each vacuum mode is characterized by its wave vector $\mathbf{k}$, polarization vector $\mathbf{s}$, and angular frequency $\nu_{\mathbf{k}}$, where $\hat{a}^{\dagger}_{\mathbf{k}}$ ($\hat{a}_{\mathbf{k}}$) is the corresponding creation (annihilation) operator. The exchange of photons between the atoms and the environment takes place with coupling strength $g^{(n)}_{\mathbf{k},\mathbf{s}} = \mathbf{s}\cdot\mathbf{d}_n\sqrt{\nu_{\mathbf{k}}/2\epsilon_0 V_{\mathbf{k}}}$, for $\mathbf{d}_n$, ϵ_0 and $V_{\mathbf{k}}$, respectively, the dipole matrix elements of the transitions, the vacuum permittivity and the mode volumes.

The explicit time dependence on the laser terms, appearing in the last line of Eq.(3.1), can be removed by applying two consecutive unitary transformations. First, we move to the interaction picture by applying $\hat{U}_0 = e^{-i\hat{H}_0 t}$, with

$$\hat{H}_0 = \sum_{j=1}^{N}\sum_{n=1}^{3} \omega_{nn}\hat{\sigma}^{j}_{nn} + \sum_{n=1}^{2}\sum_{\mathbf{k},\mathbf{s}} \nu_{n\mathbf{k}} \left(\hat{a}^{\dagger}_{\mathbf{k},\mathbf{s}}\hat{a}_{\mathbf{k},\mathbf{s}} + \frac{1}{2}\right) \tag{3.2}$$

representing the sum of the free energy terms, which results in the time dependent interaction Hamiltonian that can be written as

$$\begin{aligned}\hat{H}_I &= \frac{1}{2}\sum_{j=1}^{N}\sum_{n=1}^{2} \Omega_n \left(\hat{\sigma}^{j}_{n3} e^{i\Delta_n t - i\mathbf{k}_n\cdot\mathbf{r}_j} + \hat{\sigma}^{j}_{3n} e^{-i\Delta_n t + i\mathbf{k}_n\cdot\mathbf{r}_j}\right) \\ &+ \sum_{j=1}^{N}\sum_{n=1}^{2}\sum_{\mathbf{k},\mathbf{s}} g^{(n)}_{\mathbf{k},\mathbf{s}} \left(\hat{\sigma}^{j}_{n3}\hat{a}^{\dagger}_{\mathbf{k},\mathbf{s}} e^{i\Delta^{-}_{n\mathbf{k}} t - i\mathbf{k}_n\cdot\mathbf{r}_j} + \hat{\sigma}^{j}_{3n}\hat{a}_{\mathbf{k},\mathbf{s}} e^{-i\Delta^{-}_{n\mathbf{k}} t + i\mathbf{k}_n\cdot\mathbf{r}_j}\right. \\ &\left. + \hat{\sigma}^{j}_{3n}\hat{a}^{\dagger}_{n\mathbf{k}} e^{i\Delta^{+}_{n\mathbf{k}} t - i\mathbf{k}_n\cdot\mathbf{r}_j} + \hat{\sigma}^{j}_{n3}\hat{a}_{n\mathbf{k}} e^{-i\Delta^{+}_{n\mathbf{k}} t + i\mathbf{k}_n\cdot\mathbf{r}_j}\right), \end{aligned} \tag{3.3}$$

where we have defined the detunings $\Delta_n = \omega_n - \omega_{3n}$ and $\Delta^{\pm}_{n\mathbf{k}} = \nu_{n\mathbf{k}} \pm \omega_{3n}$. After that, we apply the unitary transformation $\hat{U}_1 = e^{-i\left[\sum_j (\Delta_1-\Delta_2)\hat{\sigma}^j_{22} + \Delta_1 \hat{\sigma}^j_{33}\right]t}$, finally obtaining

$$\begin{aligned}\hat{\mathcal{H}} &= \sum_{j=1}^{N}\left[(\Delta_1-\Delta_2)\,\hat{\sigma}^j_{22} + \Delta_1\hat{\sigma}^j_{33}\right] + \frac{1}{2}\sum_{j=1}^{N}\sum_{n=1}^{2}\Omega_n\left(\hat{\sigma}^j_{n3}e^{-i\mathbf{k}_n\cdot\mathbf{r}_j} + \hat{\sigma}^j_{3n}e^{i\mathbf{k}_n\cdot\mathbf{r}_j}\right)\\ &+\sum_{j=1}^{N}\sum_{n=1}^{2}\left(\hat{\sigma}^j_{n3}e^{-i\omega_n t} + \hat{\sigma}^j_{3n}e^{i\omega_n t}\right)\sum_{\mathbf{k},\mathbf{s}} g^{(n)}_{\mathbf{k},\mathbf{s}}\left(\hat{a}^{\dagger}_{\mathbf{k},\mathbf{s}}e^{i\nu_{\mathbf{k}}t - i\mathbf{k}\cdot\mathbf{r}_j} + \hat{a}_{\mathbf{k},\mathbf{s}}e^{-i\nu_{\mathbf{k}}t + i\mathbf{k}\cdot\mathbf{r}_j}\right). \quad (3.4)\end{aligned}$$

Note that the time dependence was transferred to the interaction between atoms and vacuum modes, which is the required expression for the next steps.

In order to obtain the expectation values dynamics for the atomic operators, we first evolve atom and photon operators in the Heisenberg representation, according to the Hamiltonian (3.4), ending up with

$$\frac{d\hat{a}_{\mathbf{k},\mathbf{s}}}{dt} = -i\sum_{n=1}^{2}\sum_{j=1}^{N} g^{(n)}_{\mathbf{k},\mathbf{s}}\left(\hat{\sigma}^j_{n3}e^{-i\omega_n t} + \hat{\sigma}^j_{3n}e^{i\omega_n t}\right)e^{i\nu_{n\mathbf{k}}t - i\mathbf{k}\cdot\mathbf{r}_j}, \quad (3.5)$$

$$\begin{aligned}\frac{d\hat{\sigma}^j_{13}}{dt} &= -i\Delta_1\hat{\sigma}^j_{13} - \frac{i}{2}\Omega_1\left(\hat{\sigma}^j_{11} - \hat{\sigma}^j_{33}\right)e^{i\mathbf{k}_1\cdot\mathbf{r}_j} - \frac{i}{2}\Omega_2\hat{\sigma}^j_{12}e^{i\mathbf{k}_2\cdot\mathbf{r}_j}\\ &-ie^{i\omega_1 t}\left(\hat{\sigma}^j_{11} - \hat{\sigma}^j_{33}\right)\sum_{\mathbf{k},\mathbf{s}} g^{(1)}_{\mathbf{k},\mathbf{s}}\left(\hat{a}^{\dagger}_{\mathbf{k},\mathbf{s}}e^{i\nu_{1\mathbf{k}}t - i\mathbf{k}\cdot\mathbf{r}_j} + \hat{a}_{\mathbf{k},\mathbf{s}}e^{-i\nu_{1\mathbf{k}}t + i\mathbf{k}\cdot\mathbf{r}_j}\right)\\ &-ie^{i\omega_2 t}\hat{\sigma}^j_{12}\sum_{\mathbf{k},\mathbf{s}} g^{(2)}_{\mathbf{k},\mathbf{s}}\left(\hat{a}^{\dagger}_{\mathbf{k},\mathbf{s}}e^{i\nu_{2\mathbf{k}}t - i\mathbf{k}\cdot\mathbf{r}_j} + \hat{a}_{\mathbf{k},\mathbf{s}}e^{-i\nu_{2\mathbf{k}}t + i\mathbf{k}\cdot\mathbf{r}_j}\right), \quad (3.6)\end{aligned}$$

$$\begin{aligned}\frac{d\hat{\sigma}^j_{23}}{dt} &= -i\Delta_2\hat{\sigma}^j_{23} - \frac{i}{2}\Omega_1\hat{\sigma}^j_{21}e^{i\mathbf{k}_1\cdot\mathbf{r}_j} - \frac{i}{2}\Omega_2\left(\hat{\sigma}^j_{22} - \hat{\sigma}^j_{33}\right)e^{i\mathbf{k}_2\cdot\mathbf{r}_j}\\ &-ie^{i\omega_1 t}\hat{\sigma}^j_{21}\sum_{\mathbf{k},\mathbf{s}} g^{(1)}_{\mathbf{k},\mathbf{s}}\left(\hat{a}^{\dagger}_{\mathbf{k},\mathbf{s}}e^{i\nu_{1\mathbf{k}}t - i\mathbf{k}\cdot\mathbf{r}_j} + \hat{a}_{\mathbf{k},\mathbf{s}}e^{-i\nu_{1\mathbf{k}}t + i\mathbf{k}\cdot\mathbf{r}_j}\right)\\ &-ie^{i\omega_2 t}\left(\hat{\sigma}^j_{22} - \hat{\sigma}^j_{33}\right)\sum_{\mathbf{k},\mathbf{s}} g^{(2)}_{\mathbf{k},\mathbf{s}}\left(\hat{a}^{\dagger}_{\mathbf{k},\mathbf{s}}e^{i\nu_{2\mathbf{k}}t - i\mathbf{k}\cdot\mathbf{r}_j} + \hat{a}_{\mathbf{k},\mathbf{s}}e^{-i\nu_{2\mathbf{k}}t + i\mathbf{k}\cdot\mathbf{r}_j}\right), \quad (3.7)\end{aligned}$$

$$\begin{aligned}\frac{d\hat{\sigma}^j_{12}}{dt} &= -i\left(\Delta_1-\Delta_2\right)\hat{\sigma}^j_{12} + \frac{i}{2}\Omega_1\hat{\sigma}^j_{32}e^{i\mathbf{k}_1\cdot\mathbf{r}_j} - \frac{i}{2}\Omega_2\hat{\sigma}^j_{13}e^{-i\mathbf{k}_2\cdot\mathbf{r}_j}\\ &+ie^{i\omega_1 t}\hat{\sigma}^j_{32}\sum_{\mathbf{k},\mathbf{s}} g^{(1)}_{\mathbf{k},\mathbf{s}}\left(\hat{a}^{\dagger}_{\mathbf{k},\mathbf{s}}e^{i\nu_{1\mathbf{k}}t - i\mathbf{k}\cdot\mathbf{r}_j} + \hat{a}_{\mathbf{k},\mathbf{s}}e^{-i\nu_{1\mathbf{k}}t + i\mathbf{k}\cdot\mathbf{r}_j}\right)\\ &-ie^{-i\omega_2 t}\hat{\sigma}^j_{13}\sum_{\mathbf{k},\mathbf{s}} g^{(2)}_{\mathbf{k},\mathbf{s}}\left(\hat{a}^{\dagger}_{\mathbf{k},\mathbf{s}}e^{i\nu_{2\mathbf{k}}t - i\mathbf{k}\cdot\mathbf{r}_j} + \hat{a}_{\mathbf{k},\mathbf{s}}e^{-i\nu_{2\mathbf{k}}t + i\mathbf{k}\cdot\mathbf{r}_j}\right), \quad (3.8)\end{aligned}$$

$$\begin{aligned}\frac{d\hat{\sigma}^j_{nn}}{dt} &= -\frac{i}{2}\Omega_n\left(\hat{\sigma}^j_{n3}e^{-i\mathbf{k}_n\cdot\mathbf{r}_j} - \hat{\sigma}^j_{3n}e^{i\mathbf{k}_n\cdot\mathbf{r}_j}\right)\\ &-i\sum_{\mathbf{k},\mathbf{s}} g^{(n)}_{\mathbf{k},\mathbf{s}}\left(\hat{\sigma}^j_{13}e^{-i\omega_n t} - \hat{\sigma}^j_{31}e^{i\omega_n t}\right)\left(\hat{a}^{\dagger}_{\mathbf{k},\mathbf{s}}e^{i\nu_{n\mathbf{k}}t - i\mathbf{k}\cdot\mathbf{r}_j} + \hat{a}_{\mathbf{k},\mathbf{s}}e^{-i\nu_{n\mathbf{k}}t + i\mathbf{k}\cdot\mathbf{r}_j}\right), \quad (3.9)\end{aligned}$$

for $n = 1, 2$.

Then, we can formally solve for the photon operator by integrating Eq. (3.5), where we neglect the vacuum fluctuation terms $\hat{a}_{\mathbf{k},\mathbf{s}}(0)$, obtaining

$$\hat{a}_{\mathbf{k},\mathbf{s}}(t) = -i\sum_{n=1}^{2}\sum_{j=1}^{N} g^{(n)}_{\mathbf{k},\mathbf{s}}\int_0^t dt'\left(\hat{\sigma}^j_{n3}e^{-i\omega_n t} + \hat{\sigma}^j_{3n}e^{i\omega_n t}\right)e^{i\nu_{n\mathbf{k}}t - i\mathbf{k}\cdot\mathbf{r}_j}. \quad (3.10)$$

Substituting Eq. (3.10) in the dipole equations Eqs.(3.6)-(3.9) [24, 43, 36], in the the Markov approximation, where we consider $\hat{\sigma}^l_{mn}(t-\tau) \approx \hat{\sigma}^l_{mn}(t)$, assuming that the photon-transit time is much shorter than the decay time (slow decay) [44], and also neglecting fasting oscillating terms proportional to $e^{2i\omega_n t}$, we finally obtain the following reduced dynamics:

$$\frac{d\hat{\sigma}^j_{nn}}{dt} = \frac{\Gamma_n}{2}\hat{\sigma}^j_{33} + \frac{1}{2}\left(\hat{\sigma}^j_{3n}\hat{\mathcal{F}}^j_n + \text{H.c.}\right), \tag{3.11}$$

$$\frac{d\hat{\sigma}^j_{n3}}{dt} = -\left(\frac{\Gamma}{2} + i\Delta_n\right)\hat{\sigma}^j_{n3} - \frac{1}{2}\left[\left(\hat{\sigma}^j_{nn} - \hat{\sigma}^j_{33}\right)\hat{\mathcal{F}}^j_n + \hat{\sigma}^j_{nm}\hat{\mathcal{F}}^j_m\right], \tag{3.12}$$

$$\frac{d\hat{\sigma}^j_{12}}{dt} = i\left(\Delta_2 - \Delta_1\right)\hat{\sigma}^j_{12} + \frac{1}{2}\left[\hat{\sigma}^j_{32}\hat{\mathcal{F}}^j_1 + \hat{\sigma}^j_{13}\left(\hat{\mathcal{F}}^j_2\right)^\dagger\right], \tag{3.13}$$

for $m, n = 1, 2$ with $m \neq n$, where we define the effective field operators

$$\hat{\mathcal{F}}^j_n \equiv i\hat{\mathbb{1}}\Omega_n e^{i\mathbf{k}_n\cdot\mathbf{r}_j} + \sum_{l\neq j}\hat{\sigma}^l_{n3}G^{jl}_n + \text{Noise}, \tag{3.14}$$

and the effective light-mediated interactions

$$G^{jl}_n \equiv 2\int_0^\infty d\tau e^{i\omega_n\tau}\sum_{\mathbf{k},\mathbf{s}}\left|g^{(n)}_{\mathbf{k},\mathbf{s}}\right|^2\left(e^{-i\nu_{\mathbf{k}}\tau + i\mathbf{k}\cdot\mathbf{r}_{jl}} - c.c.\right). \tag{3.15}$$

In Eqs. (3.11)-(3.13), the decay rates that determine the time scale of the problem are $\Gamma_n \equiv \text{Re}\left(G^{jj}_n\right)$, with $\Gamma \equiv \Gamma_1 + \Gamma_2$. Whereas in Eq. (3.15), we have defined $\mathbf{r}_{jl} \equiv \mathbf{r}_j - \mathbf{r}_l$ as the relative position between atoms j and l. Note that the upper limit of the time integral in Eq. (3.15) is now the infinity since the vacuum modes dynamics are much faster then the population dynamics.

Going to the spherically symmetric continuous integration

$$\sum_{\mathbf{k}} \to \frac{V}{(2\pi)^3}\int_0^\infty k^2 dk\int_0^\pi \sin\theta d\theta\int_0^{2\pi} d\phi, \tag{3.16}$$

which covers all possible wave vectors $\mathbf{k}$ [23, 24, 25], we end up with effective long-range interactions,

$$G^{jl}_n = \frac{3}{2}\frac{\Gamma_n e^{ik_n r_{jl}}}{ik_n r_{jl}}\left[1 + \frac{i}{k_n r_{jl}} - \frac{1}{k_n^2 r_{jl}^2} - \left(\frac{z_{jl}}{r_{jl}}\right)^2\left(1 + \frac{3i}{k_n r_{jl}} - \frac{3}{k_n^2 r_{jl}^2}\right)\right], \tag{3.17}$$

that decay with the euclidean distance $r_{jl} = |\mathbf{r}_{jl}|$ between atomic pairs. Here, we have defined $z_{jl} = z_j - z_l$, where z_j is the position of the *j-th* atom along the cylinder's longitudinal axis. For the derivation of the interactions G^{jl}_n, one takes into account the polarization of all vacuum modes in the radiation-matter Hamiltonian [36]. This is the reason of the name "vectorial" for the corresponding scattering model. However, dilute atomic clouds ($\rho/k_1^3 < 0.01$) are well described by the scalar approximation [45, 24]

$$G^{jl}_n \approx \frac{\Gamma_n e^{ik_n r_{jl}}}{ik_n r_{jl}}, \tag{3.18}$$

which can be obtained by not taking into account the polarization vectors $\mathbf{s}$ in the initial Hamiltonian $\hat{H}$. In this work, we consider the scalar model for the calculation of the transparency window, while both models are compared in the collective STIRAP analysis.

Returning to Eqs. (3.11)-(3.13), we now obtain the dynamical equations for the expectation values $\langle \cdot \rangle$ of the dipole operators $\hat{\sigma}^j_{nn}$. We consider that the total density matrix of the system can be approximated by the tensor product between the individual density matrices of each subsystem $\left(\hat{\rho} = \hat{\rho}^1 \otimes \hat{\rho}^2 \otimes ... \otimes \hat{\rho}^N\right)$, which in our case is a good approximation for incident fields such that $\Omega_n < \Gamma_n$ [46]. As a result, we can neglect the correlations between different dipoles $\langle \hat{\sigma}^j_{nm} \hat{\sigma}^l_{n'm'} \rangle \approx \langle \hat{\sigma}^j_{nm} \rangle \langle \hat{\sigma}^l_{n'm'} \rangle$, for $j \neq l$, while still keeping single-atom correlations $\langle \hat{\sigma}^j_{nm} \hat{\sigma}^j_{n'm'} \rangle$. This type of semiclassical approximation leads us to the following system of equations:

$$\frac{d\left\langle \hat{\sigma}^j_{nn} \right\rangle}{dt} = \frac{\Gamma_n}{2}\left\langle \hat{\sigma}^j_{33} \right\rangle + \mathrm{Re}\left(\left\langle \hat{\sigma}^j_{3n} \right\rangle \left\langle \hat{\mathcal{F}}^j_n \right\rangle\right), \tag{3.19}$$

$$\frac{d\left\langle \hat{\sigma}^j_{n3} \right\rangle}{dt} = -\left(\frac{\Gamma}{2} + i\Delta_n\right)\left\langle \hat{\sigma}^j_{n3} \right\rangle - \frac{1}{2}\left\langle \hat{\sigma}^j_{nm} \right\rangle \left\langle \hat{\mathcal{F}}^j_m \right\rangle - \frac{1}{2}\left(\left\langle \hat{\sigma}^j_{nn} \right\rangle - \left\langle \hat{\sigma}^j_{33} \right\rangle\right)\left\langle \hat{\mathcal{F}}^j_n \right\rangle, \tag{3.20}$$

$$\frac{d\left\langle \hat{\sigma}^j_{12} \right\rangle}{dt} = i\left(\Delta_2 - \Delta_1\right)\left\langle \hat{\sigma}^j_{12} \right\rangle + \frac{1}{2}\left(\left\langle \hat{\sigma}^j_{32} \right\rangle \left\langle \hat{\mathcal{F}}^j_1 \right\rangle + \left\langle \hat{\sigma}^j_{13} \right\rangle \left\langle \hat{\mathcal{F}}^j_2 \right\rangle^*\right), \tag{3.21}$$

for $m, n = 1, 2$ with $m \neq n$. Note that the contribution from noise operators disappears in the semiclassical approximation since $\left\langle \hat{a}_{\mathbf{k},\mathbf{s}}\left(0\right) \right\rangle = 0$ for a white noise reservoir. As another consequence of the semiclassical approximation, the expectation values

$$\left\langle \hat{\mathcal{F}}^j_n \right\rangle = i\Omega_n e^{i\mathbf{k}_n \cdot \mathbf{r}_j} + \sum_{l \neq j} G^{jl}_n \left\langle \hat{\sigma}^l_{n3} \right\rangle \tag{3.22}$$

act like mean fields exciting the atomic transitions. The first contribution comes from the incident fields, while the second contribution represents the influence of all the other atoms on a given atom j, described by the light-mediated interactions from Eq. (3.17) [47, 36].

Finally, we point out that the optical interactions G^{jl}_n are the main ingredient that distinguish Eqs. (3.19)-(3.21) from those that describe independent three-level atoms. Note that it couples the transition $|1\rangle \leftrightarrow |3\rangle$ of a given atom to the transition $|2\rangle \leftrightarrow |3\rangle$ from another atom. An effect neglected in single-scattering models but that here is essential for our many-atom analyses, as can be seen in the following.

3.3 Collective Transparency Window

The procedure adopted in most experiments to investigate the transparency properties of a medium relies on light transmission measurements [15, 6, 37, 38, 39]. In this context, the total scalar electric field operator [48, 24, 25],

$$\hat{E}\left(\mathbf{r}, t\right) = \hat{\mathbb{1}} E_1 e^{i\mathbf{k}_1 \cdot \mathbf{r}} - \frac{\Gamma_1}{2d_1} \sum_{j=1}^{N} \hat{\sigma}^j_{13}\left(t\right) \frac{e^{ik_1 |\mathbf{r} - \mathbf{r}_j|}}{k_1 \left|\mathbf{r} - \mathbf{r}_j\right|}, \tag{3.23}$$

is investigated around the transition frequency ω_{31}, within the spectral range where the contribution of the control field can be neglected. In Eq.(3.23), the probe field, of amplitude $E_1 \equiv \Omega_1/d_1$, interferes with its associated scattered field, and generates an intensity profile $I(\mathbf{r},t) \propto \left\langle \hat{E}^{\dagger}(\mathbf{r},t)\,\hat{E}(\mathbf{r},t)\right\rangle$ over the whole three-dimensional space. The symbol $\hat{\mathbb{1}}$ represents the identity operator of the atomic Hilbert space. To keep the consistence of our procedure, we also consider the semiclassical approximation for the intensity:

$$I(\mathbf{r},t) \propto \left|\left\langle \hat{E}(\mathbf{r},t)\right\rangle\right|^2 + \frac{\Gamma_1^2}{4d_1^2}\sum_{j=1}^{N}\frac{\left\langle \sigma_{33}^{j}(t)\right\rangle - \left|\left\langle \sigma_{13}^{j}(t)\right\rangle\right|^2}{k_1^2\left|\mathbf{r}-\mathbf{r}_j\right|^2}, \tag{3.24}$$

where only quantum correlations between different dipoles were again neglected.

In our simulations, probe and control fields propagate along the longitudinal axis of a cylinder with thickness L and radius R, where the random positions of the atoms are homogeneously distributed with a given average density $\rho = N/L\pi R^2$ (see Fig. 6) [49]. We then obtain the transmission T by numerically integrating the steady-state solution of Eq.(3.24) in a disk of area $\mathcal{A} = \pi s_{max}^2$, at the observation point z_0, for a radius of integration s_{max}. The result is divided by the incident power $E_1^2\pi s_{max}^2$, as in the following:

$$T = \frac{1}{E_1^2\pi s_{max}^2}\int d^2s I(\mathbf{s}, z_0, t\to\infty). \tag{3.25}$$

To minimize the power losses by diffraction effects around the cylinder edges, we chose $R \gg L$ and $s_{\max} < R$ [50]. Given that most experiments are carried out in the optical regime and the specific range of parameters we are adopting, the fundamental lengths L and R would be in the scale of μm. We calculate many realizations of the EIT transmission spectrum as a function of the probe field detuning Δ_1, keeping the radius R constant for different values of the density ρ and the sample thickness L, and take the average to reduce the fluctuations. The number of realizations can vary from dozens to thousand, depending on the number of scatterers, and it is increased until one sees no significant changes in the transmission curves. We focus on densities $\rho \leq 0.01k_1^3$ and optical thicknesses $b < 1$ (see Appendix A), where multiple scattering orders are already required to describe coherent light scattering by cold atoms [47]. Our goal is to show that EIT and applications are sensitive to coherent light-mediated interactions even for optically dilute regimes.

Figure 7 displays the transmission spectrum as a function of the sample density and thickness, in the limits where the scalar model remains a good approximation ($\rho \lesssim 0.01k_1^3$) [45]. In particular, Figs. 7(a) and 7(b) were obtained for $\Omega_2 \gg \Omega_1$, a regime usually named as the "EIT regime", while (c) and (d) for $\Omega_1 \sim \Omega_2$, the "CPT regime" [6]. Note that the transparency at the resonance line ($\Delta_1 = 0$) remains unchanged for EIT and CPT regimes, so light-mediated interactions are not able to reduce the transparency maximum as Rydberg interactions do. [37, 38, 39, 40]. Such a difference arises from the very nature of the interactions: Rydberg interactions do not depend on how the atoms scatter light, whereas optical interactions totally disappear when the system reaches a dark state [6].

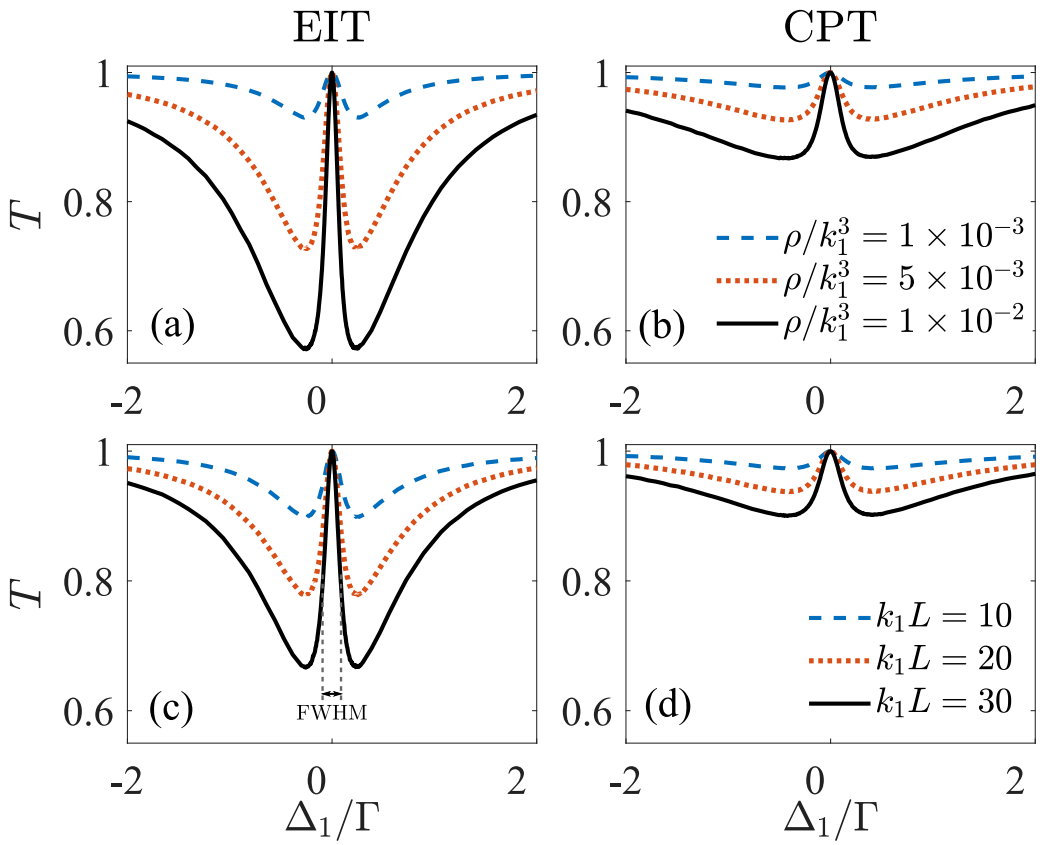

Figure 7 – Transmission spectrum as a function of the probe field detuning. (a) and (c) were calculated in the EIT regime ($\Omega_2 = 0.5\Gamma \gg \Omega_1 = 0.1\Gamma$), while (b) and (d) were obtained for the CPT regime ($\Omega_2 = \Omega_1 = 0.5\Gamma$). In (a) and (b) we see the changes in the transmission spectrum for different values of the atomic density ρ, for a fixed cylinder thickness $k_1L = 40$. While for (c) and (d) we vary k_1L for a fixed density $\rho/k_1^3 = 0.01$. In panels (a) and (b), the number of atoms N ranged from 314 to 3140 and, in panels (c) and (d), from 785 to 2335. For all plots we set $\Delta_2 = 0$ and $k_1R = 50$. Taken from Ref. [1].

Outside the resonance line, but still within the transparency window, we show that the FWHM is affected by collective effects for a not-so-low densities ($\rho < 0.01k_1^3$), a regime where recent works sought high efficiencies in quantum memories [20, 21, 22]. In Fig. 8, we exhibit the FWHM for EIT and CPT transparency windows, as a function of the sample density ρ and thickness L. We confront the results obtained from the full system of equations (3.19)-(3.21), where the multiple scattering of light is preserved, with those of totally independent atoms ($G_n^{jl} = 0$). The latter model predicts only single-scattering events, with no communication between the dipoles. Nevertheless, the scattered fields from each individual atom still interfere, thus being equivalent to highly rarefied atomic sample [51, 52]. As can be clearly noted in Figs. 8 (a-d), both models converge for very small densities and sample thickness (single-scattering regime), where weak incident fields ($\Omega_1, \Omega_2 \ll \Gamma_1, \Gamma_2$) leads to the limit FWHM $\propto (\Omega_1^2 + \Omega_2^2)/\Gamma$ [53]. Yet, as the density increases for a fixed thickness (and vice-versa), a substantial disagreement appears between

both models. The single-scattering model predicts a slow linear increment of EIT and CPT FWHM, while a practically linear narrowing of the transparency window is predicted by the complete interacting model even over the range where atomic clouds are still considered dilute ($\rho \lesssim 0.01k_1^3$). In particular, Figs. 8(a) and 8(c), obtained for the EIT regime, show narrowings of 34.2% and 27.8%, respectively, at the largest point of the horizontal axis. In the CPT regime (Figs. 8(b) and 8(d)), the narrowings are considerable smaller: 21.5% and 17.0%, respectively. Our results point out that higher-order scattering events are relevant for the calculation of the narrowing of the transparency window [47].

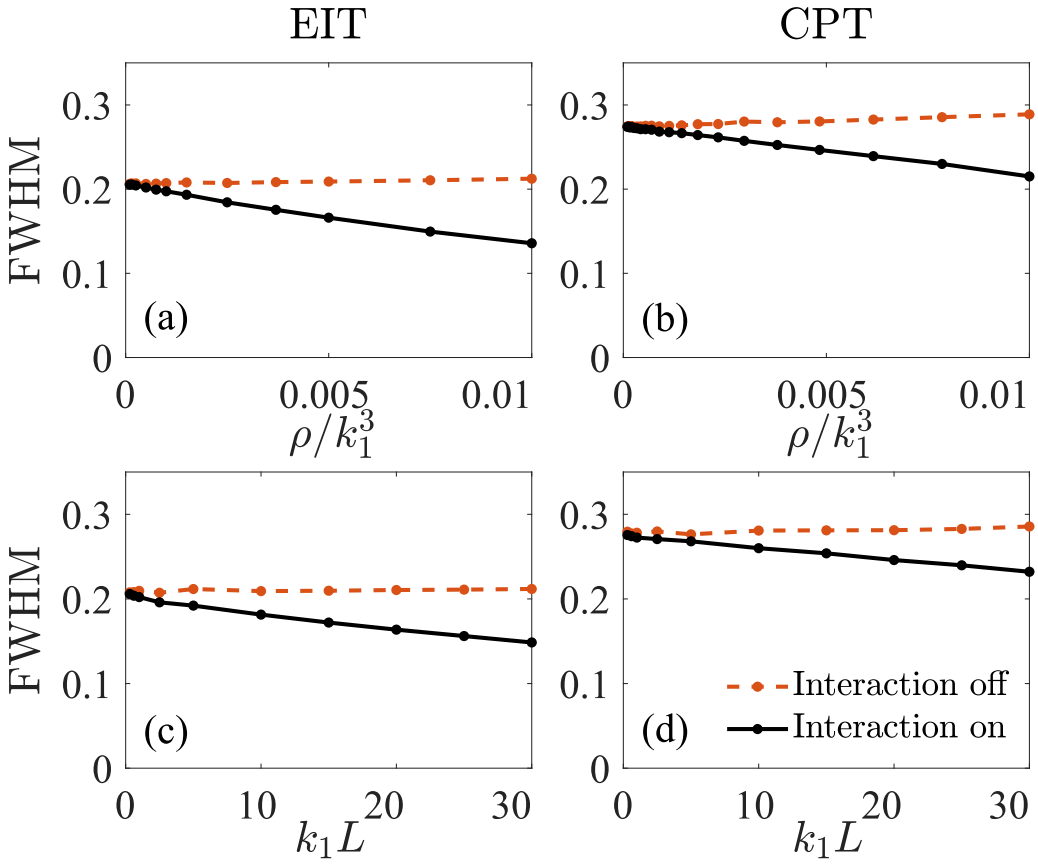

Figure 8 – FWHM as a function of ρ and L for models with and without interacting terms. The full black curves are obtained by solving the full system of Equations (3.19)-(3.21), whereas dashed orange curves by turning off all dipole interactions. (a) and (c) were calculated in the EIT regime ($\Omega_2 = 0.5\Gamma \gg \Omega_1 = 0.1\Gamma$), while (b) and (d) were obtained for the CPT regime ($\Omega_2 = \Omega_1 = 0.5\Gamma$). In (a) and (b) we see the changes in the FWHM by varying the atomic density ρ, for a fixed cylinder thickness $k_1L = 40$, while for (c) and (d) we vary k_1L for a fixed density $\rho/k_1^3 = 0.01$. For all plots we set $\Delta_2 = 0$ and $k_1R = 50$, and the maximum number of atoms in the cloud in the simulations was $N = 3142$. Taken from Ref. [1].

We would like to highlight that narrowing of the EIT FWHM have been already estimated empirically from Beer-Lambert's law [54, 6], where many physical processes, as for instance, Doppler effect and collisions, contribute to this spectral narrowing. In

these previous works, one deduces the scaling of the FWHM with the density from a naive extrapolation of the susceptibility for an ideal EIT non-interacting medium, where a Gaussian ansatz for the near-resonance transmittivity is considered [54, 6]. Our microscopic model, instead, predicts by first-principles the narrowing of the transparency window provided by multiple-scattering effects (non-ideal medium), with no empirical assumptions for the transmission spectrum.

In the transmission profile, we have detected an asymmetry between positive and negative detunings (a little higher transmission for positive detunings). Such asymmetric behavior has been observed since the first experimental realization of the EIT phenomenon [55] and was wrongly attributed to several different effects, as Fano Interference and noninterfering photoionization channels [55]. However, the origin of such asymmetry relies on the interference that emerges between incident and scattered fields, whose mathematical term is proportional to the detuning Δ_1 [56]. This feature is not unique to three-level systems.

Looking at the valleys of the transmission curves, we can see that minimum transmission $T_{\min}$ (around $\Delta_1 = \pm\sqrt{\Omega_1^2 + \Omega_2^2}/2$) gets drastically reduced for increasing ρ and L. Figures 9(a) and 9(c), obtained for the EIT regime, show a reduction of 42.9% and 33.4% in the minimum transmission, respectively, for the last points of the horizontal axis. Whereas Figs. 9(b) and 9(d), obtained for the CPT regime, show a smaller variation: $13,3\%$ and 10%, respectively. We infer that $T_{\min}$ is weakly affected by atomic interactions since the single-scattering model describes qualitatively well the reduction of the minimum transmission, over the regime where FWHM is incorrectly described by the same model. In other words, multiple scattering affects the FWHM even for not-so-high densities. The valleys of the transmission curves are actually modified for independent atoms when varying macroscopic parameters (ρ,L) because the incident intensity I_0 is kept constant over the detection area $\mathcal{A}$ at the same time that the number of absorbers changes.

3.4 Collective STIRAP

Now let us study how light-mediated interactions affect a coherent population transfer between the two ground states $|1\rangle \rightarrow |2\rangle$ via STIRAP [42], a key process for many quantum information applications, e.g., quantum memories [6]. To this goal, any slight probability of finding atoms in state $|1\rangle$ is deleterious for the process. Therefore, taking care of precision, henceforward we compare the predictions from scalar and full vectorial models. Initializing the system with all atoms in the ground state $|1\rangle$, we consider both

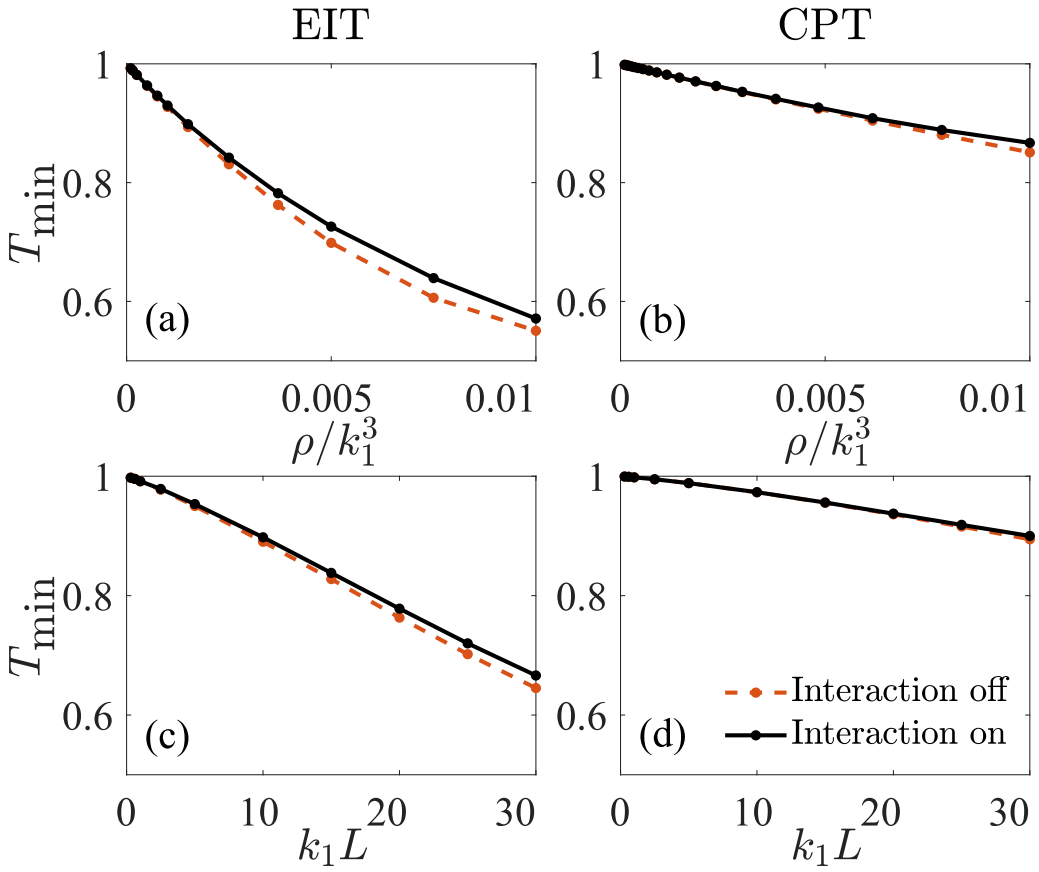

Figure 9 – Minimum value of transmission as a function of ρ and L. The full black curves are obtained by solving the full system of dynamical equations, whereas dashed orange curves by turning off all dipole interactions. (a) and (c) were calculated in the EIT regime ($\Omega_2 = 0.5\Gamma \gg \Omega_1 = 0.1\Gamma$), while (b) and (d) were obtained for the CPT regime ($\Omega_2 = \Omega_1 = 0.5\Gamma$). In (a) and (b) we see the changes in the FWHM by varying the atomic density ρ, for a fixed cylinder thickness $k_1 L = 40$, while for (c) and (d) we vary $k_1 L$ for a fixed density $\rho/k_1^3 = 0.01$. For all plots we set $\Delta_2 = 0$ and $k_1 R = 50$, and the maximum number of atoms in the cloud in the simulations was $N = 3142$. As a result of the asymmetry discussed in the text, we obtain different values of $T_{\min}$ for opposite detunings, around $\Delta_1 = \pm\sqrt{\Omega_1^2 + \Omega_2^2}/2$, so $T_{\min}$ refers to the lowest value between the two. Taken from Ref. [1].

fields varying in time as

$$\Omega_1(t) = \Omega_{\max}\left\{\theta(t-t_f) + \sin\left(\frac{\pi t}{2t_r}\right)[\theta(t-t_0) - \theta(t-t_f)]\right\}, \tag{3.26}$$

$$\Omega_2(t) = \Omega_{\max}\left\{1 - \theta(t-t_0) + \cos\left(\frac{\pi t}{2t_r}\right)[\theta(t-t_0) - \theta(t-t_f)]\right\}, \tag{3.27}$$

where $\Omega_{\max}$ represents the maximum value of the Rabi frequency of the fields, t_0 is the STIRAP process starting time, t_r is the time it takes for the sine (cosine) to reach its maximum (minimum), $t_f = t_0 + t_r$ is the instant where the variations in the fields end, and $\theta(x)$ is the Heaviside step function. The adiabaticity criterion is then fulfilled when $\Omega_1, \Omega_2 \gg \pi/2t_r$, and the population for independent atoms should be totally transferred

coherently to the ground state $|2\rangle$ without ever populating the leaky excited state $|3\rangle$. In the previous section, we have studied the system's optical response in the steady state for a fixed ratio Ω_1/Ω_2, which leads the system to the stationary dark state $|1\rangle$. In the STIRAP, however, this ratio changes from 0 to ∞. Now we initially prepare the system in $|1\rangle$, with the typical EIT configuration $\Omega_1 \gg \Omega_2$, and vary the parameters until we reach $\Omega_1 \ll \Omega_2$. This is the same regime as before but now with swapped roles for the two fields. The adiabatic theorem [57, 58] tells us that if the process is adiabatic, the system will now be at the new dark state $|2\rangle$.

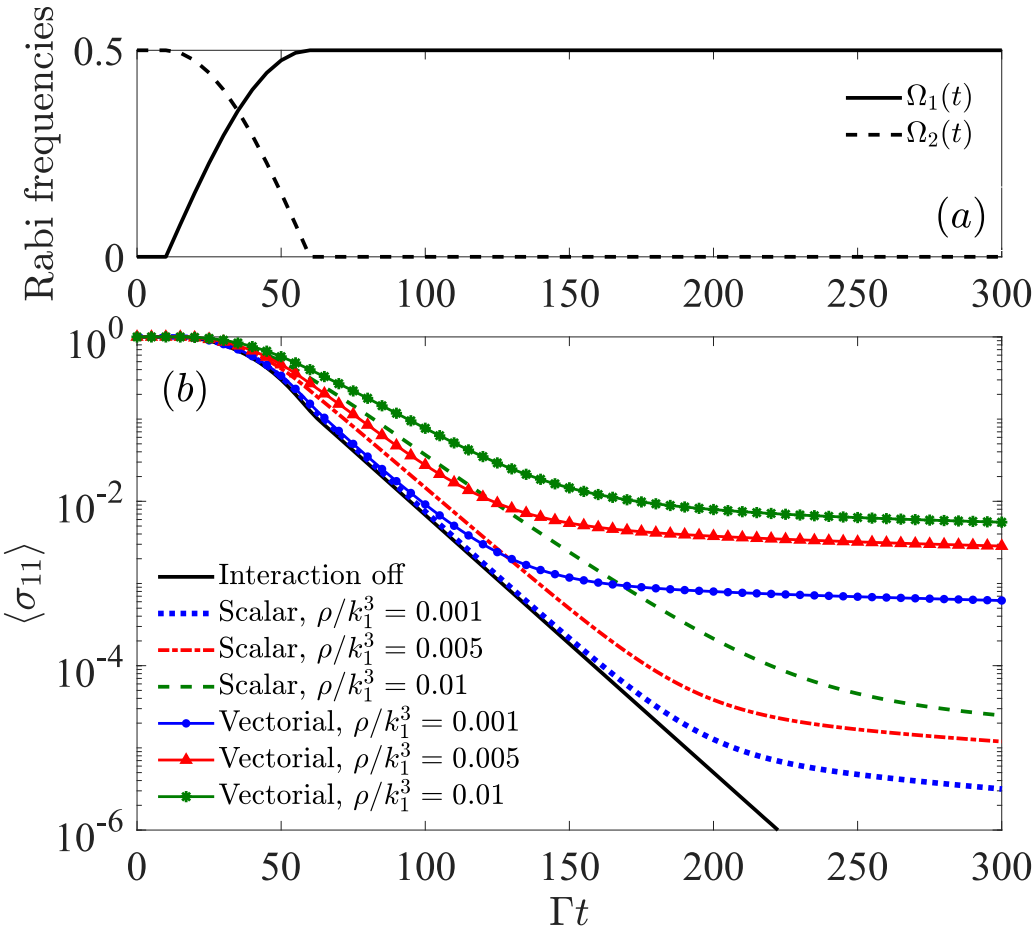

Figure 10 – STIRAP process in a cold cloud of three-level atoms. Panel (a) shows how the Rabi frequencies of the probe and control field change in time, starting in a condition where $\Omega_1 \ll \Omega_2$ and adiabatically reaching a regime where $\Omega_1 \gg \Omega_2$. Panel (b) shows how the average ground state population of the state $|1\rangle$ behaves for different densities. For all plots we set $\Omega_{\text{max}} = 0.5\Gamma$, $t_0 = 10\Gamma$, $t_r = 60\Gamma$, $\Delta_1 = \Delta_2 = 0$, $k_1 L = 60$ and $k_1 R = 40$. The number of atoms N ranges from 1005 to 3015. Taken from Ref. [1].

Panel (a) of Figure 10 shows the time variation of both fields, whereas painel (b) shows the average population $\langle\sigma_{11}\rangle$ of the ground state $|1\rangle$ throughout the process, for different values of density. Note that, after the STIRAP is over, the average population probability $\langle\sigma_{11}\rangle$ remains for both scalar and vectorial models over much longer times than

the noninteracting prediction. In particular, the vectorial model (represented by markers) shows a deviation around 1% ($\langle\sigma_{11}\rangle \approx 10^{-2}$) for $\rho/k_1^3 = 0.01$, two orders of magnitude higher than that from the scalar model ($\langle\sigma_{11}\rangle \approx 10^{-5}$). One could argue that such an error is not relevant. However, since the long-range interactions cannot be eliminated, they pose a fundamental limit for STIRAP based applications. For instance, from the results showed in Figure 10, a qualitative estimation of the efficiency loss in the writing process of a quantum memory can be made. If the long-range interactions reduce the capacity of storing a photonic state in the atomic basis with high fidelity, in a quantum algorithm where the memory has to be accessed thousands of times [59], these errors will propagate and it is expected to drastically reduce the practical overall information retrieval efficiency of the quantum memory device. Our result points out that the efficiency can be even worse for increasing densities.

3.5 Conclusion

In conclusion, we have derived a model that describes the light scattering by a cold ensemble of three-level atoms. In the scalar regime, we were able to investigate how light-mediated long-range interactions influence EIT and CPT phenomena, by simulating the light transmission spectrum. This analysis demonstrates that optical dipole-dipole interactions considerably narrow the transparency window for sufficiently dense and large atomic clouds, which can be useful for applications such as high-resolution spectroscopy. We have demonstrated that collective scattering also modifies a STIRAP process, showing that it spoils the population transfer between two atomic states. Although a propagating pulse model is required to infer a quantitative influence of these interactions on quantum memories, our microscopic analysis recreates the basic writing process of such devices and poses fundamental limitations to quantum memories.

Finally, we believe that our coupled-dipole model for three-level atoms, with control and probe fields, is useful for the study of many other situations. For example, it can be employed to investigate how nonlinear-optics effects [6, 60] are modified by collective scattering of light, as well as to understand if probe intensity profiles in space can be controlled by a control field. We can also investigate the modification of the efficiency for writing and generation of single photons in three-level systems via DLCZ protocol [61] for increasingly atomic densities.

4 Steady-state entanglement generation for non-degenerate qubits

4.1 Introduction

Entanglement is the clearest nonclassical signature of quantum physics. A composite system is considered to be entangled when the quantum state that describes it is inseparable, *i.e.*, it is impossible to write it as a product of the states of each subsystem [62]. In the last decades, entangled states have been the subject of great interest, presenting themselves as a resource for several quantum schemes and applications such as quantum communication [63, 64, 65], quantum computation [66], metrology [67] and quantum sensing [68].

The success of the aforementioned applications and tests often depends on the ability to generate long-lived entangled states. However, in a realistic situation, the system will interact with the environment. This will inevitably lead to the deterioration of the entangled state, which is sensitive to decoherence [62]. For this reason, entanglement preservation schemes have gained great prominence. Among the proposed methods to minimize unwanted decoherence, we should mention the use of decoherence-free subspaces [69, 70], quantum error correction codes [71, 72], weak measurements [73, 74] and the quantum Zeno effect [75, 76].

Instead of aiming to prevent decoherence, a different strategy involves engineering the system-environment interaction to *generate* entangled states, these are called dissipation-assisted entanglement generation methods [77, 78, 79]. Since this idea was presented, numerous implementations have been proposed and experimentally realized using several physical platforms, such as cavity QED [80, 81, 82, 83, 84], superconducting qubits [85, 86, 87, 88], macroscopic atomic ensembles [89, 90], Rydberg atoms [91, 92, 93] and trapped ions [94, 95, 96, 97, 98, 99]. Another widely studied approach is the creation of long-lived entangled states via stimulated Raman adiabatic passage (STIRAP) [100, 42], since it offers robustness against decoherence by not populating lossy states.

In this chapter we propose two new schemes for producing highly-entangled states in a system of two non-degenerate qubits. It is known that, in some systems, it is possible to manipulate the degree of entanglement between two qubits via Stark shifts of their electronic levels [101, 82, 102]. Here, however, we show that the symmetry in the energy shifts between the emitters with respect to the bosonic mode actually allows us to achieve a stronger entanglement. By considering their effective interaction through a bosonic mode, such as an optical cavity or a motional mode, we are able to achieve a stronger coupling between the qubits without needing to place the qubits particularly close together. This

interaction with the quantized mode provides a coupling regime strong enough so that the time scales of the effective interactions are much faster than the qubit relaxation, leading to higher degrees of entanglement. This shows that the distinguishability between the quantum emitters can be an advantage in the quest for the production highly-entangled states. We are able to achieve a maximally entangled steady state, which is maintained by injecting power via a pump field.

We show that the dynamics leading to the highly-entangled two-qubit state can be understood by comparison with the electromagnetically induced transparency (EIT) regime [103]. In that same analogy, but restricting ourselves to the subspace of just a single excitation, we are able to drive the system into an entangled state via a STIRAP-like process.

4.2 Model

Let us consider a system of two qubits, with different resonance frequencies $\omega_e^{(1)}$ and $\omega_e^{(2)}$, which are coupled to the same bosonic mode with frequency ω_m, as illustrated in Fig. 11(a). Here, the bosonic mode is symmetrically detuned from each of the qubits, so that $\omega_e^{(1)} = \omega_m - \Delta$ and $\omega_e^{(2)} = \omega_m + \Delta$. In the Schrödinger picture, the system Hamiltonian reads ($\hbar = 1$):

$$\hat{H} = \omega_e^{(1)}\hat{\sigma}_{ee}^{(1)} + \omega_e^{(2)}\hat{\sigma}_{ee}^{(2)} + \omega_m\hat{a}^\dagger\hat{a} + g\left[\hat{a}\left(\hat{\sigma}_+^{(1)} + \hat{\sigma}_+^{(2)}\right) + h.c.\right], \tag{4.1}$$

where $\hat{\sigma}_+^{(k)} = |e\rangle\langle g|$, $\hat{\sigma}_-^{(k)} = |g\rangle\langle e|$ and $\hat{\sigma}_{ee}^{(k)} = |e\rangle\langle e|$ are the raising, lowering and excited-state population operators, respectively, acting on the k-th qubit (with $k \in \{1, 2\}$). Without loss of generality, we define the ground state energy to be zero. $\hat{a}$ ($\hat{a}^\dagger$) is the annihilation (creation) operator of the bosonic mode, g is the coupling strength between the bosonic mode and each of the qubits, and *h.c.* stands for the Hermitian conjugate.

For convenience, we move to the interaction picture, make the rotating wave approximation, and move to a rotating referential of relative coordinates in which both qubits are stationary, thus eliminating the Hamiltonian time dependence. Then, Eq. (4.1) becomes

$$\hat{\mathcal{H}} = \Delta\left(\hat{\sigma}_{ee}^{(1)} - \hat{\sigma}_{ee}^{(2)}\right) + g\left[\hat{a}\left(\hat{\sigma}_+^{(1)} + \sigma_+^{(2)}\right) + h.c.\right]. \tag{4.2}$$

To account for decoherence, we consider our system to be in a weak system-environment coupling regime, which allows us to use the Lindblad master equation [7] at temperature $T = 0\,\mathrm{K}$. The assumption of zero temperature is reasonable since we work within the optical regime, where the number of thermal photons remains negligible even for room temperatures. Thus, we obtain the dynamical equations for the density matrix $\hat{\rho}$

$$\dot{\hat{\rho}} = -i\left[\hat{\mathcal{H}}, \hat{\rho}\right] + \hat{\mathscr{L}}_{\mathrm{q}}^{(1)} + \hat{\mathscr{L}}_{\mathrm{q}}^{(2)} + \hat{\mathscr{L}}_m, \tag{4.3}$$

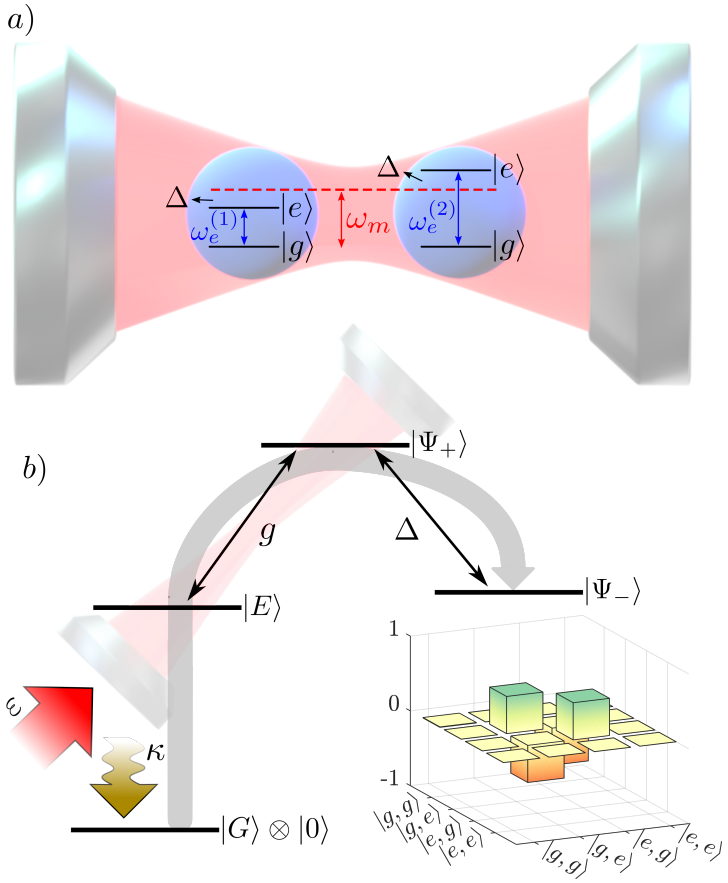

Figure 11 – a) Two non-degenerate qubits, with both ground states coupled to the bosonic mode of frequency ω_m, detuned by $\pm\Delta$. b) Level scheme of the same system, but now in the basis up to one excitation: $|G\rangle \otimes |0\rangle$, $|E\rangle = |G\rangle \otimes |1\rangle$, and $|\Psi_\pm\rangle = |\Phi_\pm\rangle \otimes |0\rangle$, where $|G\rangle = |g, g\rangle$ and $|\Phi_\pm\rangle = (|e, g\rangle \pm |g, e\rangle)/\sqrt{2}$. Here, g promotes transitions from $|E\rangle$ to $|\Psi_+\rangle$, while Δ from $|\Psi_+\rangle$ to $|\Psi_-\rangle$. We consider a pump field, of strength ε, continuously injecting energy into the mode to combat decay from the mode with rate κ. The inset in b) shows the entangled steady state partial density matrix, where the bosonic mode has been traced out. Taken from Ref. [2].

where

$$\hat{\mathscr{L}}_{\mathrm{q}}^{(k)} = \Gamma\left(2\hat{\sigma}_{-}^{(k)}\hat{\rho}\hat{\sigma}_{+}^{(k)} - \hat{\sigma}_{ee}^{(k)}\hat{\rho} - \hat{\rho}\hat{\sigma}_{ee}^{(k)}\right) \tag{4.4}$$

is the Lindblad term that accounts for the spontaneous decay from the excited state of the k-th qubit, with $k \in \{1, 2\}$ and Γ is the qubit decay rate, here assumed the same for both qubits. The Lindblad term

$$\hat{\mathscr{L}}_{m} = \kappa\left(2\hat{a}\hat{\rho}\hat{a}^{\dagger} - \hat{a}^{\dagger}\hat{a}\hat{\rho} - \hat{\rho}\hat{a}^{\dagger}\hat{a}\right) \tag{4.5}$$

accounts for the decay of the bosonic mode, where κ is the decay rate.

4.3 Steady state entanglement production

To describe the main mechanism responsible for the generation of entanglement, we restrict ourselves, for the moment, to the single-excitation subspace, which is composed of the following three states: $|E\rangle = |G\rangle \otimes |1\rangle$ and $|\Psi_\pm\rangle = |\Phi_\pm\rangle \otimes |0\rangle$, where $|G\rangle = |g,g\rangle$ and $|\Phi_\pm\rangle = (|e,g\rangle \pm |g,e\rangle)/\sqrt{2}$. $|\Phi_\pm\rangle$ are maximally entangled two-qubit states. In this subspace, the reduced Hamiltonian is:

$$\hat{\tilde{\mathcal{H}}} = \Delta|\Psi_-\rangle\langle\Psi_+| + \sqrt{2}g|\Psi_+\rangle\langle E| + h.c.\ . \tag{4.6}$$

In analogy with the typical three-level Λ systems, we consider that $|E\rangle$ and $|\Psi_-\rangle$ play the roles of the two ground states, while $|\Psi_+\rangle$ is the excited state, as depicted in Fig. 11(b). According to Eq. (4.6), the transitions $|E\rangle \leftrightarrow |\Psi_+\rangle$ and $|\Psi_-\rangle \leftrightarrow |\Psi_+\rangle$ have effective coupling strengths $\sqrt{2}g$ and Δ, respectively. The Hamiltonian in Eq. (4.6) has a *dark eigenstate* (an eigenstate without a $|\Psi_+\rangle$ component) given by

$$|D\rangle = -\frac{\Delta}{\sqrt{\Delta^2+2g^2}}|E\rangle + \frac{\sqrt{2}g}{\sqrt{\Delta^2+2g^2}}|\Psi_-\rangle. \tag{4.7}$$

Just as in other three-level systems [103], when the condition $g \gg \Delta$ is fulfilled, the dark state $|D\rangle$ transforms to $|\Psi_-\rangle$, which is our maximally entangled target state.

A significant difference between our system and a typical three-level Λ-system is the fact that neither $|E\rangle$ nor $|\Psi_-\rangle$ are actually ground states. Because of this, the system keeps spontaneously decaying to the true zero energy ground state $|G\rangle \otimes |0\rangle$. For this reason, the analogy becomes more accurate as the mode dissipation rate κ and the spontaneous decay rate Γ become negligible ($\kappa, \Gamma \ll g, \Delta$). Then the system effectively remains in the one-excitation subspace. One way to circumvent the decay and maintain the system in the one-excitation subspace is to keep injecting energy into the mode. We consider this energy injection as an additional term

$$\hat{H}_{\text{pump}} = \varepsilon\left(\hat{a}^\dagger + \hat{a}\right) \tag{4.8}$$

of the system's Hamiltonian, where ε is the pump strength.

To characterize the steady-state entanglement between the qubits, we choose the monotone quantifier concurrence [104, 105]. We numerically simulate the full system dynamics,considering the decoherence and also higher excited states. The concurrence is derived from the steady-state density matrix, which we obtain using the Quantum Toolbox in Python (QuTiP) [106], after the bosonic mode is traced out.

As shown in Fig. 12(a), we obtain a strong entanglement within a large region of parameters Δ and g for $\varepsilon = \kappa$. Moreover, we see that satisfying the EIT condition $g \gg \Delta$ is a necessary but not sufficient condition to reach our maximally entangled target state. We have chosen four sets of parameters to illustrate the system dynamics: A shows the

situation where $g \ll \Delta$ and the population is led to the respective dark state, which has a $|G\rangle$ character [see Eq. (4.7)], and no entanglement is observed; in B, we have $g = \Delta$ which leads to a weakly entangled dark state given by a mixture of $|g, g\rangle$ and $|\Phi_-\rangle$; in C we have an interesting situation where the EIT condition $g \gg \Delta$ is fulfilled, the dark state assumes a $|\Phi_-\rangle$ character, but the detuning is so small that it takes too long to populate $|\Phi_-\rangle$, and since the system keeps decaying to the true ground state $|G\rangle \otimes |0\rangle$, the entanglement is affected; D shows a near-optimal situation, with $g \gg \Delta$ and $\Delta \gg \Gamma$, driving approximately all the population to the dark state $|\Phi_-\rangle$.

In a similar way, Fig. 12(b) shows a map of concurrence in the steady state as a function of g and ε, with the constraint $\Delta = 0.1g$. This ratio between g and Δ was chosen to obtain maximum concurrence based on the results shown in Fig. 12(a). We can see that for the adopted spontaneous decay rate, for small and large values of ε the concurrence tends to zero, but in between those limits, it presents a maximum plateau for $g > \kappa$. The value $\varepsilon = \kappa$ is close to the point where it is possible to obtain a high degree of entanglement even for weak coupling strengths ($g \lesssim \kappa$).

In Fig. 12(c) we show the behavior of the concurrence as a function of the detuning for a fixed value of $g = \kappa$. We observe that the concurrence decreases significantly when we move away from the optimal point $\Delta \approx 0.1g$. This finding is in accordance with what was previously discussed for the parameters sets A and C. This optimal ratio between g and Δ is influenced by the system's decay rate Γ. A reduced value of Γ allows us to achieve entanglement for smaller detunings. For $\Gamma = 0$, even an infinitesimal detuning would eventually take the system to $|\Phi_-\rangle$. Figure 12(c) shows that the spontaneous decay reduces the entanglement even for the optimal case D; the concurrence decreases exponentially for $\Gamma > 5 \times 10^{-4}\kappa$.

Focusing on the entanglement dynamics, we show in Fig. 12(d) the concurrence over time for the cases A, B, C and D, where we observe different time scales to achieve the maximum entanglement for each curve, respectively. We also include a visual representation of the time evolved partial density matrix, where the bosonic mode has been traced out, showing that we achieve the maximally entangled target state $|\Phi_-\rangle$ for the near-optimal set of parameters D.

So far, we have adopted a generic description of the system, since our scheme proves to be quite versatile in terms of how many experimental platforms it could be implemented: optical cavities with neutral atoms coupled to the same cavity mode [107, 108], superconducting artificial atoms coupled to waveguides [109, 110], and ions trapped in the same harmonic potential, coupled via laser with Jaynes-Cummings type interaction and interaction with a collective vibrational mode [111].

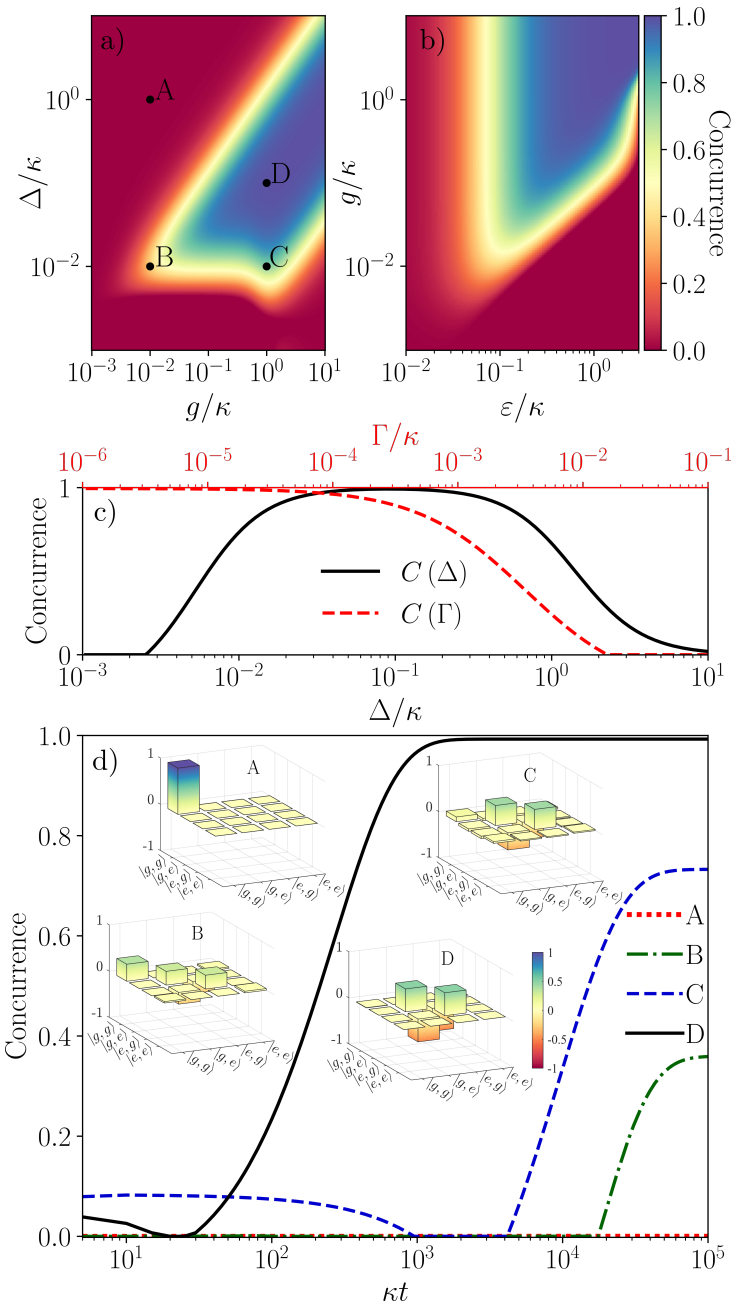

Figure 12 – Entanglement generation using the steady-state method. (a) Colormap showing the concurrence of the steady state as a function of Δ/κ and g/κ. Points A to D are referred to in panel (d). Colormap showing the concurrence of the steady state as a function of g, Δ (given the constraint $\Delta = 0.1g$) and ε. (c) Concurrence as a function of the spontaneous decay rate Γ of each of the two qubits (top x-axis) and as a function of the detuning (bottom x-axis). (d) Concurrence as a function of time for different parameter sets, given in panel (a). The concurrence generally grows and then stabilises. The insets in panel (d) show the steady state partial density matrix of each curve, where the mode has been traced out. For all panels except (b), the pump strength was set to $\varepsilon = \kappa$. The spontaneous decay rate of each qubit was fixed at $\Gamma = 10^{-5}\kappa$, except for the red dashed curve in (c). The constant parameters at (c) are given by point D in panel (a). Taken from Ref. [2].

4.4 Adiabatic process

Inspired by the schemes to counteract decoherence developed for multilevel atoms, we propose a STIRAP-like process to efficiently populate the entangled state $|\Psi_-\rangle$. For the sake of clarity and simplicity, during this section we will restrict ourselves to the physical system of trapped ions.

To this end, let us consider the case of two ions confined in a harmonic potential, as depicted in Fig. 13(a). In addition, let us also consider that two electronic levels of the ions are driven by a monochromatic laser close to resonance. The ions are subjected to a magnetic field gradient, thus allowing them to experience different energy shifts of their excited states, resembling the system illustrated in Fig. 11(a). The bosonic mode is formed by the external degrees of freedom of the ions. For simplicity, we will only consider the collective center-of-mass motional mode described by a harmonic oscillator of frequency ω_m. Absorption and stimulated emission of photons due to the interaction with the laser lead to electronic transitions, but due to the momentum of the absorbed and emitted photon may also change the ions' motional state, thus coupling the internal electronic and the external phonon dynamics of the ions [112, 113, 114]. In the Lamb-Dicke regime, the laser can be tuned in frequency to be either directly in resonance to the atomic transition, where the motional state is preserved, or in resonance to a blue or red sideband, where a phonon is generated or annihilated upon absorption of a laser photon. When tuned the red motional sideband resonance, we recover a Hamiltonian in the form of Eq. (4.2).

To perform the adiabatic population transfer between the two dark states of the one-excitation subspace (see Eq. (4.7)), the system must be initially prepared in the state $|E\rangle$, which consists of the two ions in the ground state and the motional state with one excitation; the latter can be prepared by exciting one of the ions and then by letting it exchange energy with the vibration mode via a red sideband interaction. The initial state $|E\rangle$ corresponds to the dark state when $\Delta \gg g$. By reversing this condition to $g \gg \Delta$ the dark state adiabatically transforms to $|\Psi_-\rangle$. In the proposed implementation, we can manipulate both the coupling strength g and the detuning Δ by changing the power of a laser resonant to the red sideband transition and by varying the magnetic field gradient, respectively. To illustrate, we here consider the time variation of g and Δ as

$$g(t) = \frac{g_{\max}}{2}\left[1 + \tanh \lambda(t - t_0)\right], \tag{4.9}$$

$$\Delta(t) = \frac{\Delta_{\max}}{2}\left[1 - \tanh \lambda(t - t_0)\right], \tag{4.10}$$

where $g_{\max}$ and $\Delta_{\max}$ are respectively the maximum values of the coupling constant and the detuning. The parameter t_0 is the time at which this function reaches its respective half maximum value $\Delta_{\max}/2$. The adiabaticity of the process is controlled by λ, which determines the time scale of the parameter swap and, consequently, how fast the parameters are changed. The specific choice of function is not crucial to the method, as long as it

guarantees an near-adiabatic inversion of parameters. The parameter swap previously described by Eqs. (4.9) and (4.10) is shown in Fig.13(c).

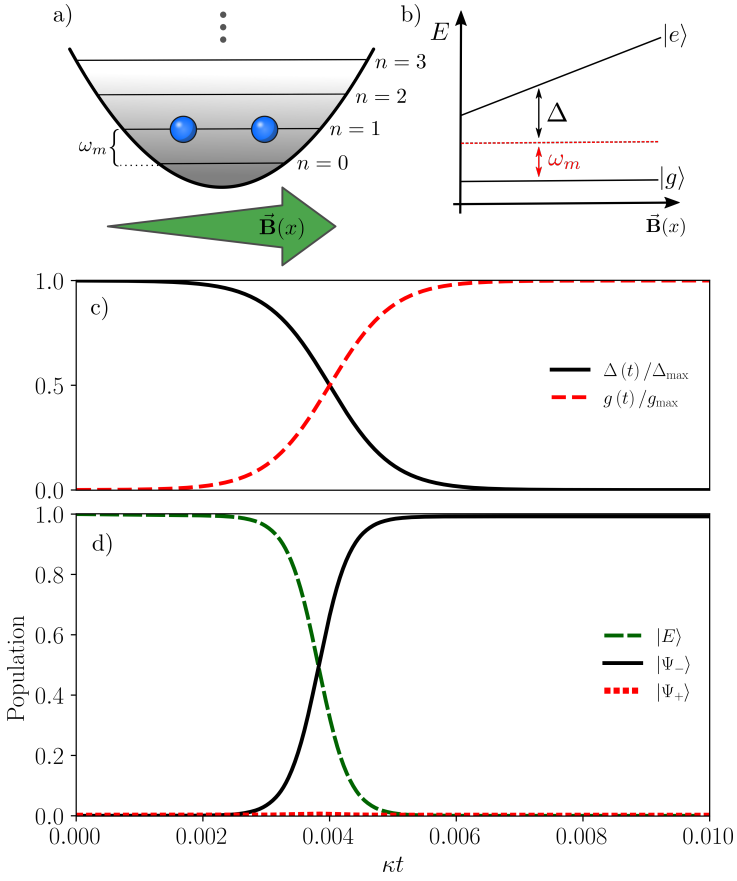

Figure 13 – Entanglement generation - adiabatic method with tunable g and Δ. (a) Two two-level ions are trapped in a harmonic potential and coupled to the same phonon mode. The ions are subjected to a magnetic field gradient, which promotes different energy shifts to their excited states, recovering the system illustrated in Fig. 11(a). (b) Pictorial representation of the energy shifts in the ions excited states due to a magnetic field gradient, as a function of their position in the trap. (c) Time evolution of the parameters $g(t)$ and $\Delta(t)$ as described in Eq. (4.9) and (4.10), with the corresponding populations changes in (d). We considered for all simulations. Adopted parameters: $\Gamma = 10^{-3}\kappa$, $g_{\max} = \Delta_{\max} = 2 \times 10^4\kappa$, $t_0 = 4 \times 10^{-3}\kappa$, $\lambda = 10^3\kappa$. Taken from Ref. [2].

In Fig. 13(d), we can see how the populations in the three states of the single excitation subspace evolve through time, showing that we coherently transfer the population from $|E\rangle$ to $|\Psi_-\rangle$ ($\langle|\Psi_-\rangle\langle\Psi_-|\rangle > 0.99$) before the mode dissipation starts to be relevant.

This scheme can also be applied to other experimental platforms. However, these might not allow a perfect control over both parameters at the same time, e.g., a fixed g and a tunable Δ as observed in systems where the coupling constant sometimes is an intrinsic value, such as in superconducting circuits. It is important to mention that the parameter swap we are proposing, although very similar to the ones observed in Raman chirped adiabatic passages (RCAP), does not involve any changes in the fields frequencies during

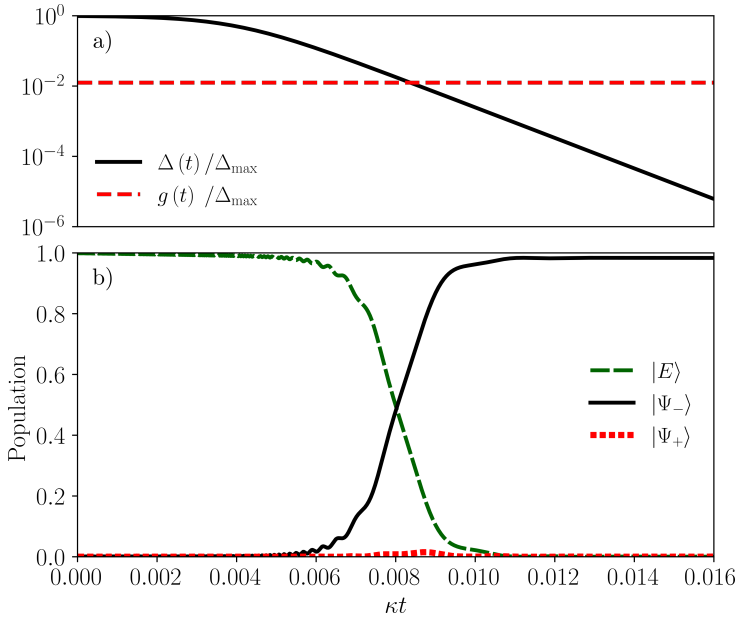

Figure 14 – Entanglement generation - adiabatic method. (a) Time evolution of g and Δ, with Δ varying accordingly to Eq. (4.10) and a constant g. (b) Population changes over time. We considered $\Gamma = 10^{-3}\kappa$, $\Delta_{\max} = 2\times10^{5}\kappa$, $g = 2.5\times10^{3}\kappa$, $t_0 = 4\times10^{-3}/\kappa$, $\lambda = 5\times10^{2}\kappa$. Taken from Ref. [2].

the process. With that being said, in order to show that even in this situation we can achieve a high degree of entanglement, we assume g to be constant and we vary Δ in time, according to (4.10) as shown in Fig. 14(a). Setting the value of g that ensures the initial and final conditions $\Delta \gg g$ and $g \gg \Delta$, respectively, we make the parameter swapping as smooth as possible. On the other hand, the lack of control over g restricts the time scale of the population transfer to maintain the adiabaticity during the parameter swap. Nevertheless, one can still perform a STIRAP-like process, obtaining a highly entangled final state, as shown in 14(b), with a negligible population of the state $|\Psi_+\rangle$.

4.5 Conclusion

In conclusion, here we presented two novel strategies for producing maximally entangled states in a system of two non-degenerate qubits coupled to a single bosonic mode. In both cases, we use a direct analogy with ordinary three-level atomic systems in the Λ-configuration and the EIT phenomenon, which allows us to draw a parallel with the processes of optical pumping and adiabatic population transfer.

In the first proposed scheme, we show, that it is possible to generate steady state entanglement with concurrence $C > 0.99$. Moreover, we show that the symmetry between the qubits with respect to the bosonic mode is beneficial for the generation of entanglement. As for the second scheme, we generate a highly entangled state by means of an adiabatic process, and we achieve a population over 99% in the state $|\Psi_-\rangle$. We emphasize that this

was done even considering non-ideal situations, where there is no complete control over g and Δ. In ideal cases, where both parameters can be controlled simultaneously, the adiabatic process can be controlled more efficiently, which leads to a perfectly coherent transfer of populations.

The results presented in this work, besides indicating new ways to generate highly entangled states in a simple way, have potential application in several experimental platforms, such as trapped ions and quantum dots molecules coupled to a cavity mode.

5 Single-shot measurements of phonon number states using the Autler-Townes effect

5.1 Introduction

The motional degree of freedom is intrinsic to many trapped ion experiments: The paradigmatic approach to trapped ion quantum information processing uses electronic states to store information while the motional modes shared by a chain of ions enable entangling operations between ion qubits [115]. In other experiments, however, the motional modes can play a more active role. For instance, in a recent experiment the motional degree of freedom was used for storing quantum information [116], allowing trapped ions to be used for continuous variable quantum information processing. The motional modes can also be a very important tool for the development of technological applications and for studying the fundamentals of general physics: in quantum logic spectroscopy [117], which is key to the workings of the most precise atomic clocks [118], the collective motion serves as a bus. Trapped ion motion also acts as the working medium in studies of thermodynamics in small systems [119, 120, 121]. Moreover, non-classical states of ion motion offer metrological advantages [122, 123, 124]. Investigations of the dynamics of phonon pair creation after drastic trap potential changes are a possibility to simulate particle creation, thus creating a link between quantum information processing and cosmology [125]. Other works also looked into measurements of local phonons and their tracking which would broaden the possibilities of quantum simulations [126, 127].

Various schemes exist to measure trapped ion motion [128, 129, 130, 119, 131, 132, 126, 133], yet efficient measurement schemes are sought after. Some techniques are maximally efficient, but suffer from additional limitations: The method using the cross-Kerr nonlinearity [132, 134, 135] only works within a narrow range of trapping parameters. The method using composite pulse sequences [126] requires multiple coherent rotations on a phonon-number-changing transition, and runs into problems when the phonon number is nine or higher [1].

Schemes for resolving Fock states have been proposed in superconducting circuits [136, 137], where a qubit is coupled to a bosonic mode in a strong dispersive interaction regime. The AC Stark shift resulting from the coupling splits the qubit spectrum, turning it into an anharmonic ladder where the dressed states energies are proportional to the dispersive coupling rate and, consequently, to the number of photons in the system. Fock

[1] This difficulty arises because the blue sideband coupling strengths for the transition from $0 \rightarrow 1$ quanta and the transition from $8 \rightarrow 9$ quanta are related by an integer multiple ($\sqrt{9} = 3$)

states have also been measured in a non-demolition detection scheme using the AC Stark shift of the transition of Rydberg atoms when interacting with photons in a cavity [138].

In this work, we introduce a new technique based on the Autler-Townes effect [139] to measure a motional mode in the number (Fock) basis in a single shot. The technique also allows quantum non-demolition measurements of Fock states of a particular motional mode and can be used to determine the phonon distribution. We demonstrate the workings of the method using a single trapped $^{88}Sr^{+}$ ion in a linear Paul trap.

5.2 Autler-Townes effect caused by coupling on a phonon-number-changing transition

The Autler-Townes effect arises in three-level systems (denoted in this work as $\{|S\rangle, |D\rangle, |D'\rangle\}$, see Fig. 15). The coupling of two levels ($\{|S\rangle, |D'\rangle\}$) by, e.g., a laser field, is described by the Hamiltonian

$$H = \frac{\hbar}{2}\begin{pmatrix} 0 & \Omega_C \\ \Omega_C & -2\Delta_C \end{pmatrix}, \tag{5.1}$$

where Ω_C is the coupling strength and $\Delta_C = \omega_0 - \omega_L$ is the detuning of the resonance ω_0 from the laser field frequency ω_L. When the coupling field is resonant ($\Delta_C = 0$) the dressed eigenstates are $(|S\rangle \pm |D'\rangle)/\sqrt{2}$, and their eigenenergies are $\pm\hbar\Omega_C/2$, respectively.

The spectral resonance for the transition from level $|D\rangle$ to level $|S\rangle$ is split into a doublet if $|S\rangle$ is strongly coupled to the level $|D'\rangle$. Each of the doublet peaks corresponds to the excitation of dressed eigenstates $(|S\rangle \pm |D'\rangle)/\sqrt{2}$ when $\Delta_C = 0$. This is called the Autler-Townes effect [139], and it is sketched in Fig. 15 for a coupling to the blue sideband (BSB) transition of the radial mode. The splitting behaviour is the same when coupling to a radial red sideband (RSB) transition. The splitting between the doublet peaks is proportional to the strength of the $|S\rangle \leftrightarrow |D'\rangle$ coupling, Ω_C. When $|S\rangle \leftrightarrow |D'\rangle$ is a phonon-number-changing transition, Ω_C becomes sensitive to the population of the respective motional mode [140]. This allows us to use the Autler-Townes doublet to probe the phonon number.

We demonstrated this by preparing a single trapped $^{88}Sr^{+}$ ion in electronic state $|D\rangle$ with one of its radial motional modes in a number state with n quanta. We then probed the $|D, n\rangle \leftrightarrow |S, n\rangle$ carrier resonance while strongly coupling the BSB transition, $|S, n\rangle \leftrightarrow |D', n+1\rangle$. The resultant spectrum displays an Autler-Townes doublet with a phonon-number dependent splitting which scales as $\sqrt{n+1}$, see Fig. 16(c).

The experiment was repeated, but this time the strong coupling field was applied to a RSB transition $|S, n\rangle$ to $|D', n-1\rangle$. The resultant spectrum again displays an Autler-Townes doublet, however in this case the splitting increases as $\sqrt{n}$, see Fig. 16(b). For

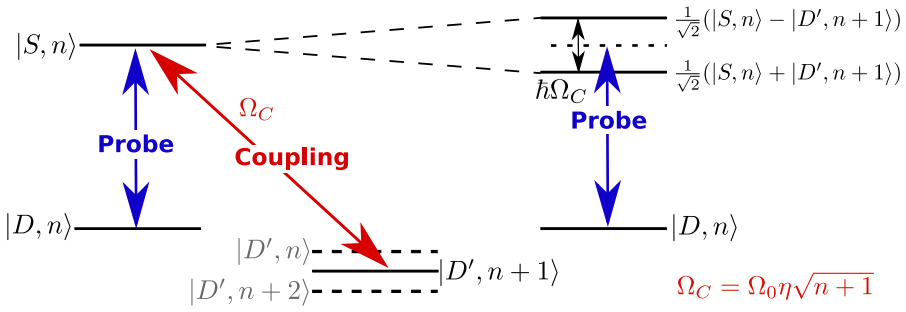

Figure 15 – The Autler-Townes effect. Left: The $|D\rangle \leftrightarrow |S\rangle$ resonance is weakly probed while levels $|S\rangle$ and $|D'\rangle$ are strongly coupled on a BSB transition. The splitting principles are the same for a RSB transition, solely the coupling strength dependency on the phonon number changes. Right: The system described in terms of dressed states. The splitting between the dressed states reveals the $|S\rangle \leftrightarrow |D'\rangle$ coupling strength Ω_C.

both experiments the excitation amplitude of the Autler-Townes doublet decreases with an increasing phonon number because it also leads to coupling strength changes of the probe. Next, we extracted the doublet splittings from Figs. 16(a) and (b) by fitting the experimental data, and we confirm the respective $\sqrt{n+1}$ and $\sqrt{n}$ scalings in Fig. 16(c). The scalings of the doublet splittings are the same as the ones of the strengths of the phonon-number changing transitions for a typical laser-ion interaction [115]. For both the coupling to the RSB and the BSB transition the scaling of the splitting is proportional to the initial coupling strength Ω_0. In Fig. 16, the splitting of the RSB scaling reaches larger values for increasing phonon number because of the higher value of Ω_0 for this scan.

5.3 Pulse sequence to efficiently measure ion motion in the number state basis

For the measurements presented we employed states $|D\rangle \equiv \left|4^2D_{5/2}\,, m_J = -\frac{1}{2}\right\rangle$, $|S\rangle \equiv \left|5^2S_{1/2}\,, m_J = -\frac{1}{2}\right\rangle$, $|S'\rangle \equiv \left|5^2S_{1/2}\,, m_J = \frac{1}{2}\right\rangle$ and $|D'\rangle \equiv \left|4^2D_{5/2}\,, m_J = -\frac{3}{2}\right\rangle$. To prepare phonon number states we cooled an ion to its motional ground state of $|S\rangle$ before iteratively applying π pulses on first the BSB to state $|D\rangle$ and then the carrier transitions back to state $|S\rangle$, as described in [128]. Before the experimental sequence, a a last π pulse is applied to initializes the ion in state $|D\rangle$. To achieve high fidelity preparation of phonon number states we also included multiple state-dependent fluorescence detection steps, performed on the $|S\rangle \equiv 5^2S_{1/2}\,, m_J = -\frac{1}{2}$ transition, during the phonon number preparation, as described in the supplemental material of ref. [141]. Finally, a π pulse was applied on the transition from $|D'\rangle$ to $|S'\rangle$ to increase the signal strength from the S manifold. This last pulse is needed since after the Autler-Townes splitting the ion is in a combination of state $|S\rangle$ and $|D'\rangle$, however the fluorescence detection only shows

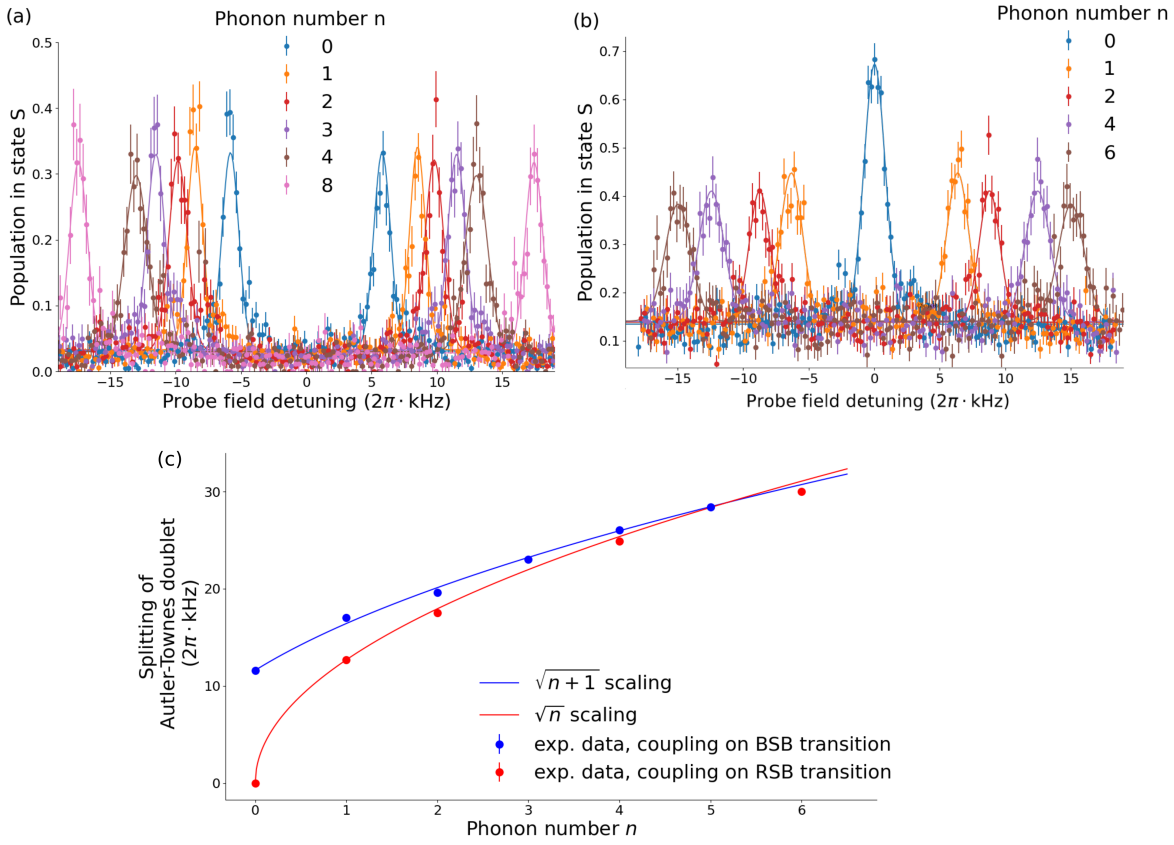

Figure 16 – Splitting of the Autler-Townes doublet. When the coupling field is resonant to a phonon-number-changing transition the splitting of the Autler-Townes doublet depends on the number of phonons in the system. (a) The coupling field was resonant to a BSB transition and the splitting scales with the phonon number n as $\sqrt{n+1}$. (b) The coupling field was resonant to a RSB transition and the splitting scales with $\sqrt{n}$. Error bars represent quantum projection noise (68% confidence intervals). (c) The blue and red data points were extracted from the doublet splitting in (a) and (b) via a fit (with the amplitude as a fitting parameter), and are described by $\sqrt{n+1}$ and $\sqrt{n}$ scalings, respectively.

a signal if the ion is initialized in the S manifold. Fluorescence detection was used to distinguish population in $|S\rangle$ and $|S'\rangle$ from population in $|D\rangle$ and $|D'\rangle$. In this way, the method can be used to test whether a trapped ion system has a particular phonon number in a particular mode with almost unit efficiency. The pulse sequence is shown in Fig. 17(a).

Using the same pulse scheme as in Fig. 17(a) one can detect the ion's motional state by keeping the probe beam to a fixed frequency. Figure 17(b) shows the results when we prepared the ion in different phonon number states, between 0 and 8, and then tested whether or not the ion has a particular number of phonons in this range. For these measurements the coupling beam was resonant to the BSB transition. Each particular test relies on a priori knowledge of the expected peak positions, which can come from,

e.g., spectra as in Fig. 16 or by measuring the frequency of Rabi oscillations on the BSB transition for a ground-state-cooled ion.

The method can be repeatedly applied in a single experimental run until the phonon number is determined. The method tests whether the system has a particular phonon number by controlling the detuning of the probe field. If the result is negative, the ion remains undisturbed in $|D, n\rangle$ and thus the method may be repeated to test for other phonon numbers until a positive result is achieved.

In the method described thus far, fluorescence indicates a positive result, and because fluorescence detection involves scattering many photons, the method corresponds to a destructive (demolition) measurement. By changing the transfer step to a π-pulse on the $|S\rangle \leftrightarrow |D\rangle$ carrier transition, *lack* of fluorescence indicates a positive result, as shown by the experimental data in Fig. 17(c). This alternate method enacts a non-demolition measurement in the phonon-number basis, and can be used to prepare ions in phonon number states. Usually after each BSB π pulse for the phonon preparation a postselection is performed. This method can be used with just one postselection step after the excitation via the Autler-Townes splitting, thus making it more efficient.

When the ion is in a particular Fock state, it is reflected by Autler-Townes splitting with the coupling strength depending on the phonon number. However, if we now look at a thermal distribution, the ion has multiple motional modes. Each motional mode leads to a different splitting for the Autler-Townes doublet. The thermal state manifests as not just one set of symmetric peaks but multiple at the different coupling strengths. The heights of the different Autler-Townes peaks can then be used to determine the probability of the motional mode, and thus the phonon distribution of the thermal sate can be characterized as shown in Fig. 18.

The thermal distribution in Fig. 18 was created by shortening the cooling cycle before the Autler-Townes splitting scan, such that the ion did not reach its motional ground state. With shorter cooling cycles, it is more likely to populate higher motional modes, leading to a higher average phonon number. Four Gaussians on each side of the Autler-Townes splitting are detected in Fig. 18, with the peak position defining the phonon number and the peak height corresponding to its population.

5.4 Limitations of the technique

The resolving power of our technique is determined by the resonance linewidths (see Appendix B.3) and by the splitting between resonances. The splitting between neighbouring resonances decreases as $\sim n^{-1/2}$, making the technique less powerful for larger n. This drawback is common to other phonon measurement methods [128, 129, 130, 119, 131, 132, 126, 133]. Larger splittings can be achieved by using a stronger coupling field, though

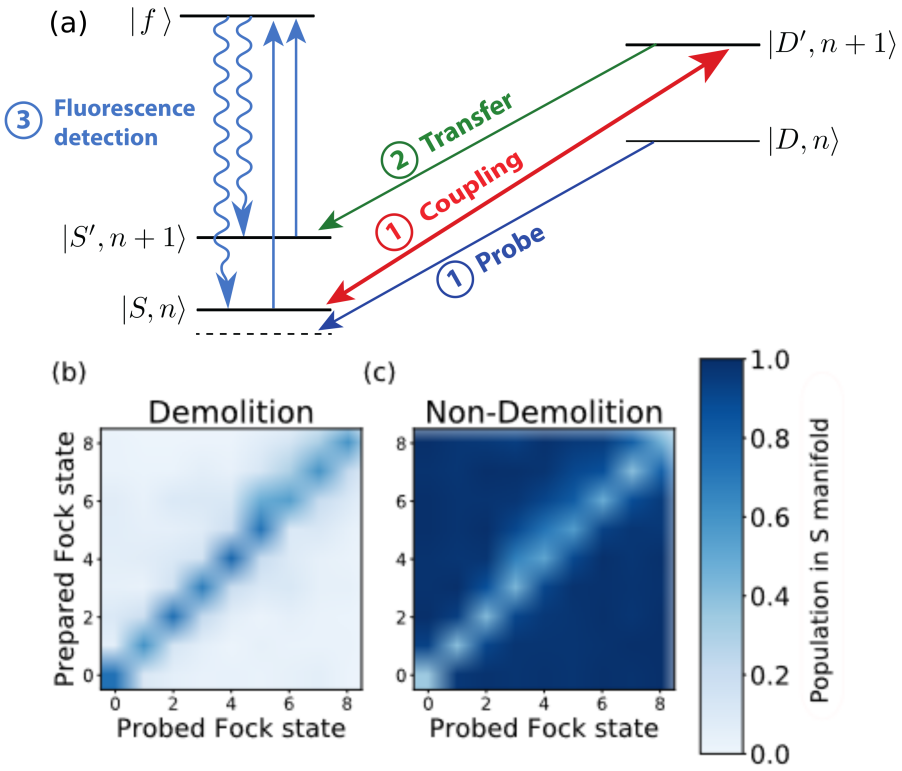

Figure 17 – (a) Measurement sequence: The ion is initialised in $|D\rangle$ with phonon number n. First a π pulse on the $|D\rangle \leftrightarrow |S\rangle$ carrier transition is attempted while a phonon-number-changing transition is strongly coupled (in the figure a BSB trasition is shown). During this step the probe field is detuned such that the $|D\rangle \rightarrow |S\rangle$ transfer only occurs if n equals the test value m. Then any population in $|D'\rangle$ is transferred to $|S'\rangle$ before both S states are coupled to the fluorescing state $|f\rangle$. Finally, detection of fluorescence indicates $n = m$. (b) Experimental demonstration of the sequence in (a). The ion was prepared in different Fock states, and when the probed Fock state matched the detection, the prepared Fock state fluorescence was detected. (c) Experimental results when the transfer step used the $|D\rangle \leftrightarrow |S\rangle$ carrier transition instead, enabling a non-destructive measurement of the ion motion in the Fock basis.

this can also cause a higher background signal due to unwanted excitations of other levels. Furthermore, as the strength of the coupling field is increased, the AC-Stark shifts increase due to coupling to other levels and coupling field intensity fluctuations cause larger broadening of the resonances [142]. This effect can be mitigated by using another field with the opposite detuning from the resonance [143].

The spectral linewidth may be limited by the laser linewidth, magnetic field noise or Fourier broadening. Longer probe times are required to reduce Fourier broadening, but this comes at the expense of increasing the sensitivity to anomalous heating which changes the ion's motional state [144].

A further point to note is that the first-order description of the coupling strength

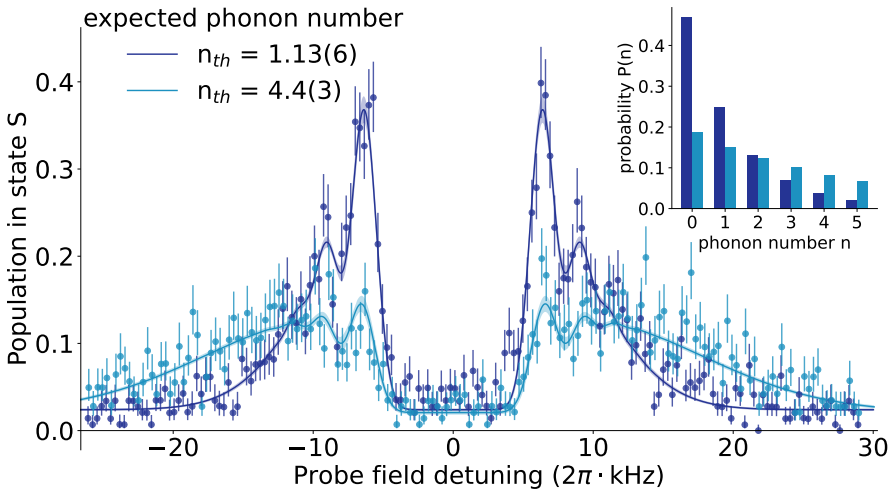

Figure 18 – Phonon number distributions. For a thermal distribution the Autler-Townes splitting shows multiple peaks at the different motional modes. The peak position is defined by the phonon number and the amplitude by the population probability of this mode. By scanning the Autler-Townes spectrum one can obtain therefore the thermal distribution of the ion.

scaling $\sim \sqrt{n+1}$ for BSB transitions and $\sim \sqrt{n}$ for RSB transitions breaks down when $\eta^2(2n+1) \not\ll 1$, where η is the Lamb-Dicke parameter. In this regime the coupling strengths are best described using Bessel functions [122].

However, an advantage of our method for resolving Fock states in comparison to the ones already proposed for superconducting circuits [136, 137] might be the applicability in systems with weaker couplings. Schemes in superconducting circuits often require an ultra-strong coupling, due to the large detuning Δ with $g^2/\Delta \gg \kappa, \Gamma$, where $g = i\eta\Omega_P$, in order to dispersively resolve single photons. The decay rate is defined as Γ and the field dissipation by κ. The strong coupling used in our scheme is achievable even in cavity QED systems [145], requiring only that $g^2 \gg \kappa, \Gamma$.

5.5 Conclusion

We introduced and demonstrated a method to measure trapped ion motion in the number basis. It relies on the Autler-Townes effect where the splitting is dependent on the motional mode when coupling to a phonon number changing transition. We showed the expected scaling depending on BSB or RSB coupling and demonstrated that this method can be used to create Fock states. The method can be repeatedly applied in a single experimental run until a positive result is achieved. Otherwise the method can enact a non-demolition measurement, and prepare trapped ions in phonon number states. A scan of the Autler-Townes spectrum allows one to determine the probabilities of individual

modes of a thermal distribution. If the individual excitation efficiency of the Autler-Townes doublet is high enough, one could also use the Autler-Townes effect to create a Fock state from a thermal distribution. The motional mode which should be excited then defines the frequency detuning of the laser from the Autler-Townes doublet of the motional ground state. As shown, it scales as $\sqrt{n+1}$ for coupling of a BSB transition and $\sqrt{n}$ for coupling to a RSB transition. The method requires a system in which a quantum harmonic oscillator can be coupled to a three-level quantum system. It can therefore also be applied to other systems such as superconducting qubits.

6 Outlook

During this thesis, we have reviewed the main results achieved during this doctoral project. As stated in the overview, these results are divided into three works, which were presented in this document as chapters, with each one approaching a different topic in quantum optics. So, in this outlook, let us summarize the main results from each individual work, state some final considerations, and possible extensions.

In the first work we have discussed here, we have derived a microscopic model that describes the EIT phenomenon in the multiple scattering regime. With this model in hands, we considered a scalar description of the scattering to show that the light-mediated long-range interactions that emerge between the dipoles narrow the EIT transparency window for increasing densities and sample sizes. And using a vectorial description, we showed that near-field interacting terms can critically affect the atomic population transfer in a STIRAP process. This result points out that standard STIRAP-based quantum memories in cold atomic ensembles would not reach high enough efficiencies for quantum information processing applications even in dilute regimes.

This result, however, only provides a qualitative glimpse of how much the interactions would actually affect the efficiency of these quantum memory devices. A direct extension of this work consists of considering a light pulse propagating through the sample and simulating an actual writing and reading process. However, this would require taking into account retardation terms in the operators of the system, making the numerical solution of the system even more computationally demanding.

Following that, we presented a scheme to dissipatively produce steady-state entanglement in a two-qubit system, via an interaction with a bosonic mode. The system is driven into a stationary entangled state, while we compensate for the mode dissipation by injecting energy via a coherent pump field. We also presented a scheme which allows us to adiabatically transfer all the population to the desired entangled state.

As stated in the conclusion of the chapter where we present these results, we hope that this process has potential application in several systems, such as trapped ions and quantum dots. A next step for this work may be the application of these schemes in a specific experimental platform. In the numerical results we presented, the system parameters were adjusted to maximize the degree of entanglement. However, we can see that it is possible to obtain a high degree of entanglement even when we relax these parameters. In fact, during my stay at the University of Stockholm, we had already discussed the feasibility of using these ideas to obtain entangled states in the trapped ion system, but at that time, the coherence time of the system would be a limiting factor to the

efficiency of the process. Hopefully with future upgrades to the experimental system, our colleagues from the University of Stockholm will be able to perform these measurements.

Finally, we presented a single-shot method to measure Fock states in the number basis, which relies on probing an Autler-Townes splitting that arises when two levels are strongly coupled via a phonon-number changing transition. The method was implemented using a single trapped ion, where it can be used in a non-demolition fashion to prepare specific phonon number states, and we have showed that the Autler-Townes splitting can be used to measure phonon number distributions. A possible extension to this work that we have already discussed among the authors would be engineering, using carrier and phonon-number changing pulses, generalized NOON states in a system of multiple trapped ions.

So, we truly believe that the value of these works lies not only on their results themselves but also on the range of possible extensions and future studies that can be derived from them to answer unexplored questions.

Bibliography

1 OLIVEIRA, M. H.; MÁXIMO, C. E.; VILLAS-BOAS, C. J. Sensitivity of electromagnetically induced transparency to light-mediated interactions. *Phys. Rev. A*, American Physical Society, v. 104, p. 063704, Dec 2021. Disponível em: <https://link.aps.org/doi/10.1103/PhysRevA.104.063704>. Cited 8 times on pages 14, 15, 21, 38, 44, 45, 47, and 48.

2 OLIVEIRA, M. H. et al. Steady-state entanglement generation for non-degenerate qubits. *arXiv preprint arXiv:2205.10590 (Accepted by Physical Review A)*, 2022. Cited 7 times on pages 15, 16, 22, 53, 56, 58, and 59.

3 SCULLY, M. O.; ZUBAIRY, M. S. *Quantum optics*. [S.l.]: AAPT, 1999. Cited on page 24.

4 JAYNES, E. T.; CUMMINGS, F. W. Comparison of quantum and semiclassical radiation theories with application to the beam maser. *Proceedings of the IEEE*, IEEE, v. 51, n. 1, p. 89–109, 1963. Cited on page 24.

5 SHORE, B. W.; KNIGHT, P. L. The jaynes-cummings model. *Journal of Modern Optics*, Taylor & Francis, v. 40, n. 7, p. 1195–1238, 1993. Cited on page 24.

6 FLEISCHHAUER, M.; IMAMOGLU, A.; MARANGOS, J. P. Electromagnetically induced transparency: Optics in coherent media. *Reviews of modern physics*, APS, v. 77, n. 2, p. 633, 2005. Cited 8 times on pages 25, 27, 37, 42, 43, 45, 46, and 49.

7 BREUER, H.; PETRUCCIONE, F.; PETRUCCIONE, S. *The Theory of Open Quantum Systems*. Oxford University Press, 2002. ISBN 9780198520634. Disponível em: <https://books.google.com.br/books?id=0Yx5VzaMYm8C>. Cited 2 times on pages 28 and 52.

8 HAU, L. V. et al. Light speed reduction to 17 metres per second in an ultracold atomic gas. *Nature*, Nature Publishing Group, v. 397, n. 6720, p. 594–598, 1999. Cited 2 times on pages 30 and 37.

9 SPECHT, H. P. et al. A single-atom quantum memory. *Nature*, Nature Publishing Group, v. 473, n. 7346, p. 190–193, 2011. Cited 2 times on pages 30 and 37.

10 OLIVEIRA, R. et al. A multitasking device based on electromagnetically induced transparency in optical cavities. *Quantum Information Processing*, Springer, v. 17, n. 11, p. 1–17, 2018. Cited 2 times on pages 30 and 37.

11 LIU, C. et al. Observation of coherent optical information storage in an atomic medium using halted light pulses. *Nature*, Nature Publishing Group, v. 409, n. 6819, p. 490–493, 2001. Cited 2 times on pages 30 and 37.

12 BORGES, H.; OLIVEIRA, M.; VILLAS-BOAS, C. Influence of the asymmetric excited state decay on coherent population trapping. *Scientific reports*, Nature Publishing Group, v. 7, n. 1, p. 7132, 2017. Cited on page 30.

13 WANG, H. et al. Cavity-linewidth narrowing by means of electromagnetically induced transparency. *Optics letters*, Optical Society of America, v. 25, n. 23, p. 1732–1734, 2000. Cited 2 times on pages 34 and 37.

14 LUKIN, M. D. et al. Intracavity electromagnetically induced transparency. *Optics letters*, Optical Society of America, v. 23, n. 4, p. 295–297, 1998. Cited 2 times on pages 34 and 37.

15 HARRIS, S. E.; FIELD, J. E.; IMAMOGLU, A. Nonlinear optical processes using electromagnetically induced transparency. *Phys. Rev. Lett.*, American Physical Society, v. 64, p. 1107–1110, Mar 1990. Disponível em: <https://link.aps.org/doi/10.1103/PhysRevLett.64.1107>. Cited 2 times on pages 37 and 42.

16 ALZETTA, G. et al. An experimental method for the observation of r.f. transitions and laser beat resonances in oriented na vapour. *Il Nuovo Cimento B (1971-1996)*, Springer, v. 36, n. 1, p. 5–20, 1976. Cited on page 37.

17 ARIMONDO, E.; ORRIOLS, G. Nonabsorbing atomic coherences by coherent two-photon transitions in a three-level optical pumping. *Nuovo Cimento Lettere*, v. 17, p. 333–338, 1976. Cited on page 37.

18 GORSHKOV, A. V. et al. Universal approach to optimal photon storage in atomic media. *Physical review letters*, APS, v. 98, n. 12, p. 123601, 2007. Cited on page 37.

19 MA, L.; SLATTERY, O.; TANG, X. Optical quantum memory based on electromagnetically induced transparency. *Journal of Optics*, IOP Publishing, v. 19, n. 4, p. 043001, 2017. Cited on page 37.

20 HSIAO, Y.-F. et al. Highly efficient coherent optical memory based on electromagnetically induced transparency. *Phys. Rev. Lett.*, American Physical Society, v. 120, p. 183602, May 2018. Disponível em: <https://link.aps.org/doi/10.1103/PhysRevLett.120.183602>. Cited 2 times on pages 37 and 44.

21 VERNAZ-GRIS, P. et al. Highly-efficient quantum memory for polarization qubits in a spatially-multiplexed cold atomic ensemble. *Nature communications*, Nature Publishing Group, v. 9, n. 1, p. 363, 2018. Cited 2 times on pages 37 and 44.

22 WANG, Y. et al. Efficient quantum memory for single-photon polarization qubits. *Nature Photonics*, Nature Publishing Group, v. 13, n. 5, p. 346, 2019. Cited 2 times on pages 37 and 44.

23 SVIDZINSKY, A. A.; CHANG, J.-T.; SCULLY, M. O. Cooperative spontaneous emission of n atoms: Many-body eigenstates, the effect of virtual lamb shift processes, and analogy with radiation of n classical oscillators. *Physical Review A*, APS, v. 81, n. 5, p. 053821, 2010. Cited 3 times on pages 37, 38, and 41.

24 BIENAIMé, T. et al. Atom and photon measurement in cooperative scattering by cold atoms. *Journal of Modern Optics*, Taylor & Francis, v. 58, n. 21, p. 1942–1950, 2011. Cited 4 times on pages 37, 38, 41, and 42.

25 BIENAIMé, T. et al. Cooperativity in light scattering by cold atoms. *Fortschritte der Physik*, v. 61, n. 2-3, p. 377–392, 2013. Cited 4 times on pages 37, 38, 41, and 42.

26 OLIVEIRA, R. A. de et al. Single-photon superradiance in cold atoms. *Phys. Rev. A*, American Physical Society, v. 90, p. 023848, Aug 2014. Disponível em: <https://link.aps.org/doi/10.1103/PhysRevA.90.023848>. Cited on page 37.

27 ARAÚJO, M. O. et al. Superradiance in a large and dilute cloud of cold atoms in the linear-optics regime. *Phys. Rev. Lett.*, American Physical Society, v. 117, p. 073002, Aug 2016. Disponível em: <https://link.aps.org/doi/10.1103/PhysRevLett.117.073002>. Cited on page 37.

28 ROOF, S. J. et al. Observation of single-photon superradiance and the cooperative lamb shift in an extended sample of cold atoms. *Phys. Rev. Lett.*, American Physical Society, v. 117, p. 073003, Aug 2016. Disponível em: <https://link.aps.org/doi/10.1103/PhysRevLett.117.073003>. Cited on page 37.

29 GUERIN, W.; ARAÚJO, M. O.; KAISER, R. Subradiance in a large cloud of cold atoms. *Phys. Rev. Lett.*, American Physical Society, v. 116, p. 083601, Feb 2016. Disponível em: <https://link.aps.org/doi/10.1103/PhysRevLett.116.083601>. Cited on page 37.

30 COTTIER, F.; KAISER, R.; BACHELARD, R. Role of disorder in super- and subradiance of cold atomic clouds. *Phys. Rev. A*, American Physical Society, v. 98, p. 013622, Jul 2018. Disponível em: <https://link.aps.org/doi/10.1103/PhysRevA.98.013622>. Cited on page 37.

31 WEISS, P. et al. Subradiance and radiation trapping in cold atoms. *New Journal of Physics*, IOP Publishing, v. 20, n. 6, p. 063024, jun 2018. Disponível em: <https://doi.org/10.1088%2F1367-2630%2Faac5d0>. Cited on page 37.

32 ORIOLI, A. Piñeiro; REY, A. M. Dark states of multilevel fermionic atoms in doubly filled optical lattices. *Phys. Rev. Lett.*, American Physical Society, v. 123, p. 223601, Nov 2019. Disponível em: <https://link.aps.org/doi/10.1103/PhysRevLett.123.223601>. Cited on page 37.

33 ORIOLI, A. Piñeiro; REY, A. M. Subradiance of multilevel fermionic atoms in arrays with filling $n \geq 2$. *Phys. Rev. A*, American Physical Society, v. 101, p. 043816, Apr 2020. Disponível em: <https://link.aps.org/doi/10.1103/PhysRevA.101.043816>. Cited on page 37.

34 LABEYRIE, G. et al. Coherent backscattering of light by cold atoms. *Phys. Rev. Lett.*, American Physical Society, v. 83, p. 5266–5269, Dec 1999. Disponível em: <https://link.aps.org/doi/10.1103/PhysRevLett.83.5266>. Cited on page 37.

35 CHABÉ, J. et al. Coherent and incoherent multiple scattering. *Phys. Rev. A*, American Physical Society, v. 89, p. 043833, Apr 2014. Disponível em: <https://link.aps.org/doi/10.1103/PhysRevA.89.043833>. Cited 2 times on pages 37 and 86.

36 ZHU, B. et al. Light scattering from dense cold atomic media. *Phys. Rev. A*, American Physical Society, v. 94, p. 023612, Aug 2016. Disponível em: <https://link.aps.org/doi/10.1103/PhysRevA.94.023612>. Cited 3 times on pages 37, 41, and 42.

37 WEATHERILL, K. J. et al. Electromagnetically induced transparency of an interacting cold rydberg ensemble. *Journal of Physics B: Atomic, Molecular and Optical Physics*, IOP Publishing, v. 41, n. 20, p. 201002, oct 2008. Cited 3 times on pages 37, 42, and 43.

38 PRITCHARD, J. D. et al. Cooperative atom-light interaction in a blockaded rydberg ensemble. *Phys. Rev. Lett.*, American Physical Society, v. 105, p. 193603, Nov 2010. Disponível em: <https://link.aps.org/doi/10.1103/PhysRevLett.105.193603>. Cited 3 times on pages 37, 42, and 43.

39 PETROSYAN, D.; OTTERBACH, J.; FLEISCHHAUER, M. Electromagnetically induced transparency with rydberg atoms. *Phys. Rev. Lett.*, American Physical Society, v. 107, p. 213601, Nov 2011. Disponível em: <https://link.aps.org/doi/10.1103/PhysRevLett.107.213601>. Cited 3 times on pages 37, 42, and 43.

40 ZHANG, Q.; BAI, Z.; HUANG, G. Fast-responding property of electromagnetically induced transparency in rydberg atoms. *Physical Review A*, APS, v. 97, n. 4, p. 043821, 2018. Cited 2 times on pages 37 and 43.

41 SOKOLOV, I. M.; GUERIN, W. Comparison of three approaches to light scattering by dilute cold atomic ensembles. *J. Opt. Soc. Am. B*, OSA, v. 36, n. 8, p. 2030–2037, Aug 2019. Disponível em: <http://josab.osa.org/abstract.cfm?URI=josab-36-8-2030>. Cited on page 38.

42 BERGMANN, K. et al. Roadmap on STIRAP applications. *Journal of Physics B: Atomic, Molecular and Optical Physics*, IOP Publishing, v. 52, n. 20, p. 202001, sep 2019. Disponível em: <https://doi.org/10.1088/1361-6455/ab3995>. Cited 3 times on pages 38, 46, and 51.

43 MÁXIMO, C. E. et al. Spatial and temporal localization of light in two dimensions. *Phys. Rev. A*, American Physical Society, v. 92, p. 062702, Dec 2015. Disponível em: <https://link.aps.org/doi/10.1103/PhysRevA.92.062702>. Cited on page 41.

44 MÁXIMO, C. E. et al. Spatial and temporal localization of light in two dimensions. *Phys. Rev. A*, American Physical Society, v. 92, p. 062702, Dec 2015. Disponível em: <https://link.aps.org/doi/10.1103/PhysRevA.92.062702>. Cited on page 41.

45 SKIPETROV, S. E.; SOKOLOV, I. M. Absence of anderson localization of light in a random ensemble of point scatterers. *Phys. Rev. Lett.*, American Physical Society, v. 112, p. 023905, Jan 2014. Disponível em: <https://link.aps.org/doi/10.1103/PhysRevLett.112.023905>. Cited 2 times on pages 41 and 43.

46 KRÄMER, S.; RITSCH, H. Generalized mean-field approach to simulate the dynamics of large open spin ensembles with long range interactions. *The European Physical Journal D*, v. 69, n. 12, p. 282, Dec 2015. ISSN 1434-6079. Disponível em: <https://doi.org/10.1140/epjd/e2015-60266-5>. Cited on page 42.

47 ROUABAH, M.-T. et al. Coherence effects in scattering order expansion of light by atomic clouds. *JOSA A*, Optical Society of America, v. 31, n. 5, p. 1031–1039, 2014. Cited 3 times on pages 42, 43, and 45.

48 BACHELARD, R.; PIOVELLA, N.; COURTEILLE, P. W. Cooperative scattering and radiation pressure force in dense atomic clouds. *Phys. Rev. A*, American Physical Society, v. 84, p. 013821, Jul 2011. Disponível em: <https://link.aps.org/doi/10.1103/PhysRevA.84.013821>. Cited on page 42.

49 SKIPETROV, S. E.; SOKOLOV, I. M. Transport of light through a dense ensemble of cold atoms in a static electric field. *Phys. Rev. A*, American Physical Society, v. 100, p. 013821, Jul 2019. Disponível em: <https://link.aps.org/doi/10.1103/PhysRevA.100.013821>. Cited on page 43.

50 JAVANAINEN, J. et al. Exact electrodynamics versus standard optics for a slab of cold dense gas. *Physical Review A*, APS, v. 96, n. 3, p. 033835, 2017. Cited on page 43.

51 MáXIMO, C. E. et al. Atomic lighthouse effect. *J. Opt. Soc. Am. A*, OSA, v. 31, n. 11, p. 2511–2517, Nov 2014. Disponível em: <http://josaa.osa.org/abstract.cfm?URI=josaa-31-11-2511>. Cited on page 44.

52 MORIYA, P. H. et al. Coherent backscattering of inelastic photons from atoms and their mirror images. *Phys. Rev. A*, American Physical Society, v. 94, p. 053806, Nov 2016. Disponível em: <https://link.aps.org/doi/10.1103/PhysRevA.94.053806>. Cited on page 44.

53 GRAY, H. R.; WHITLEY, R. M.; STROUD, C. R. Coherent trapping of atomic populations. *Opt. Lett.*, OSA, v. 3, n. 6, p. 218–220, Dec 1978. Disponível em: <http://ol.osa.org/abstract.cfm?URI=ol-3-6-218>. Cited on page 44.

54 LUKIN, M. D. et al. Spectroscopy in dense coherent media: Line narrowing and interference effects. *Phys. Rev. Lett.*, American Physical Society, v. 79, p. 2959–2962, Oct 1997. Disponível em: <https://link.aps.org/doi/10.1103/PhysRevLett.79.2959>. Cited 2 times on pages 45 and 46.

55 BOLLER, K.-J.; IMAMOĞLU, A.; HARRIS, S. E. Observation of electromagnetically induced transparency. *Physical Review Letters*, APS, v. 66, n. 20, p. 2593, 1991. Cited on page 46.

56 JENNEWEIN, S. et al. Coherent scattering of near-resonant light by a dense microscopic cold atomic cloud. *Phys. Rev. Lett.*, American Physical Society, v. 116, p. 233601, Jun 2016. Disponível em: <https://link.aps.org/doi/10.1103/PhysRevLett.116.233601>. Cited on page 46.

57 SAKURAI, J. J.; COMMINS, E. D. *Modern quantum mechanics, revised edition*. [S.l.]: American Association of Physics Teachers, 1995. Cited on page 48.

58 GRIFFITHS, D. J. *Introduction to quantum mechanics*. [S.l.]: Pearson International Edition (Pearson Prentice Hall, Upper Saddle River, 2005), 1960. Cited on page 48.

59 NIELSEN, M. A.; CHUANG, I. *Quantum computation and quantum information*. [S.l.]: American Association of Physics Teachers, 2002. Cited on page 49.

60 BINNINGER, T. et al. Nonlinear quantum transport of light in a cold atomic cloud. *Phys. Rev. A*, American Physical Society, v. 100, p. 033816, Sep 2019. Disponível em: <https://link.aps.org/doi/10.1103/PhysRevA.100.033816>. Cited on page 49.

61 DUAN, L.-M. et al. Long-distance quantum communication with atomic ensembles and linear optics. *Nature*, Nature Publishing Group, v. 414, n. 6862, p. 413–418, 2001. Cited on page 49.

62 HORODECKI, R. et al. Quantum entanglement. *Reviews of modern physics*, APS, v. 81, n. 2, p. 865, 2009. Cited on page 51.

63 EKERT, A. K. Quantum cryptography based on bell's theorem. *Physical review letters*, APS, v. 67, n. 6, p. 661, 1991. Cited on page 51.

64 BENNETT, C. H. et al. Teleporting an unknown quantum state via dual classical and einstein-podolsky-rosen channels. *Physical review letters*, APS, v. 70, n. 13, p. 1895, 1993. Cited on page 51.

65 BENNETT, C. H.; DIVINCENZO, D. P. Quantum information and computation. *nature*, Nature Publishing Group, v. 404, n. 6775, p. 247–255, 2000. Cited on page 51.

66 GOTTESMAN, D.; CHUANG, I. L. Demonstrating the viability of universal quantum computation using teleportation and single-qubit operations. *Nature*, Nature Publishing Group, v. 402, n. 6760, p. 390–393, 1999. Cited on page 51.

67 GIOVANNETTI, V.; LLOYD, S.; MACCONE, L. Quantum metrology. *Physical review letters*, APS, v. 96, n. 1, p. 010401, 2006. Cited on page 51.

68 DEGEN, C. L.; REINHARD, F.; CAPPELLARO, P. Quantum sensing. *Reviews of modern physics*, APS, v. 89, n. 3, p. 035002, 2017. Cited on page 51.

69 LIDAR, D. A.; CHUANG, I. L.; WHALEY, K. B. Decoherence-free subspaces for quantum computation. *Physical Review Letters*, APS, v. 81, n. 12, p. 2594, 1998. Cited on page 51.

70 VIOLA, L.; LLOYD, S. Dynamical suppression of decoherence in two-state quantum systems. *Phys. Rev. A*, American Physical Society, v. 58, p. 2733–2744, Oct 1998. Disponível em: <https://link.aps.org/doi/10.1103/PhysRevA.58.2733>. Cited on page 51.

71 STEANE, A. M. Error correcting codes in quantum theory. *Physical Review Letters*, APS, v. 77, n. 5, p. 793, 1996. Cited on page 51.

72 KNILL, E.; LAFLAMME, R. Theory of quantum error-correcting codes. *Phys. Rev. A*, American Physical Society, v. 55, p. 900–911, Feb 1997. Disponível em: <https://link.aps.org/doi/10.1103/PhysRevA.55.900>. Cited on page 51.

73 SUN, Q. et al. Reversing entanglement change by a weak measurement. *Phys. Rev. A*, American Physical Society, v. 82, p. 052323, Nov 2010. Disponível em: <https://link.aps.org/doi/10.1103/PhysRevA.82.052323>. Cited on page 51.

74 KIM, Y.-S. et al. Protecting entanglement from decoherence using weak measurement and quantum measurement reversal. *Nature Physics*, Nature Publishing Group, v. 8, n. 2, p. 117–120, 2012. Cited on page 51.

75 FACCHI, P.; LIDAR, D.; PASCAZIO, S. Unification of dynamical decoupling and the quantum zeno effect. *Physical Review A*, APS, v. 69, n. 3, p. 032314, 2004. Cited on page 51.

76 MANISCALCO, S. et al. Protecting entanglement via the quantum zeno effect. *Physical review letters*, APS, v. 100, n. 9, p. 090503, 2008. Cited on page 51.

77 DIEHL, S. et al. Quantum states and phases in driven open quantum systems with cold atoms. *Nature Physics*, Nature Publishing Group, v. 4, n. 11, p. 878–883, 2008. Cited on page 51.

78 KRAUS, B. et al. Preparation of entangled states by quantum markov processes. *Physical Review A*, APS, v. 78, n. 4, p. 042307, 2008. Cited on page 51.

79 VERSTRAETE, F.; WOLF, M. M.; CIRAC, J. I. Quantum computation and quantum-state engineering driven by dissipation. *Nature physics*, Nature Publishing Group, v. 5, n. 9, p. 633–636, 2009. Cited on page 51.

80 PLENIO, M. B. et al. Cavity-loss-induced generation of entangled atoms. *Physical Review A*, APS, v. 59, n. 3, p. 2468, 1999. Cited on page 51.

81 NICOLOSI, S. et al. Dissipation-induced stationary entanglement in dipole-dipole interacting atomic samples. *Physical Review A*, APS, v. 70, n. 2, p. 022511, 2004. Cited on page 51.

82 WANG, X.; SCHIRMER, S. G. Generating maximal entanglement between non-interacting atoms by collective decay and symmetry breaking. *arXiv preprint arXiv:1005.2114*, 2010. Cited on page 51.

83 KASTORYANO, M. J.; REITER, F.; SØRENSEN, A. S. Dissipative preparation of entanglement in optical cavities. *Physical review letters*, APS, v. 106, n. 9, p. 090502, 2011. Cited on page 51.

84 VALLE, E. D. Steady-state entanglement of two coupled qubits. *JOSA B*, Optical Society of America, v. 28, n. 2, p. 228–235, 2011. Cited on page 51.

85 SHANKAR, S. et al. Autonomously stabilized entanglement between two superconducting quantum bits. *Nature*, Nature Publishing Group, v. 504, n. 7480, p. 419–422, 2013. Cited on page 51.

86 KIMCHI-SCHWARTZ, M. et al. Stabilizing entanglement via symmetry-selective bath engineering in superconducting qubits. *Physical review letters*, APS, v. 116, n. 24, p. 240503, 2016. Cited on page 51.

87 LIU, Y. et al. Comparing and combining measurement-based and driven-dissipative entanglement stabilization. *Physical Review X*, APS, v. 6, n. 1, p. 011022, 2016. Cited on page 51.

88 DOUCET, E. et al. High fidelity dissipation engineering using parametric interactions. *Physical Review Research*, APS, v. 2, n. 2, p. 023370, 2020. Cited on page 51.

89 KRAUTER, H. et al. Entanglement generated by dissipation and steady state entanglement of two macroscopic objects. *Physical review letters*, APS, v. 107, n. 8, p. 080503, 2011. Cited on page 51.

90 SANTOS, A. C. et al. Generating long-lived entangled states with free-space collective spontaneous emission. *arXiv preprint arXiv:2110.15033*, 2021. Cited on page 51.

91 RAO, D. B.; MØLMER, K. Dark entangled steady states of interacting rydberg atoms. *Physical review letters*, APS, v. 111, n. 3, p. 033606, 2013. Cited on page 51.

92 CARR, A. W.; SAFFMAN, M. Preparation of entangled and antiferromagnetic states by dissipative rydberg pumping. *Phys. Rev. Lett.*, American Physical Society, v. 111, p. 033607, Jul 2013. Disponível em: <https://link.aps.org/doi/10.1103/PhysRevLett.111.033607>. Cited on page 51.

93 SHAO, X. et al. Dissipative preparation of steady greenberger-horne-zeilinger states for rydberg atoms with quantum zeno dynamics. *Physical Review A*, APS, v. 96, n. 6, p. 062315, 2017. Cited on page 51.

94 BARREIRO, J. T. et al. An open-system quantum simulator with trapped ions. *Nature*, Nature Publishing Group, v. 470, n. 7335, p. 486–491, 2011. Cited on page 51.

95 LIN, Y. et al. Dissipative production of a maximally entangled steady state of two quantum bits. *Nature*, Nature Publishing Group, v. 504, n. 7480, p. 415–418, 2013. Cited on page 51.

96 BENTLEY, C. et al. Detection-enhanced steady state entanglement with ions. *Physical Review Letters*, APS, v. 113, n. 4, p. 040501, 2014. Cited on page 51.

97 HORN, K. P. et al. Quantum optimal control of the dissipative production of a maximally entangled state. *New Journal of Physics*, IOP Publishing, v. 20, n. 12, p. 123010, 2018. Cited on page 51.

98 COLE, D. C. et al. Dissipative preparation of w states in trapped ion systems. *New Journal of Physics*, IOP Publishing, v. 23, n. 7, p. 073001, 2021. Cited on page 51.

99 COLE, D. C. et al. Resource-efficient dissipative entanglement of two trapped-ion qubits. *Physical Review Letters*, APS, v. 128, n. 8, p. 080502, 2022. Cited on page 51.

100 VITANOV, N. V. et al. Stimulated raman adiabatic passage in physics, chemistry, and beyond. *Rev. Mod. Phys.*, American Physical Society, v. 89, p. 015006, Mar 2017. Disponível em: <https://link.aps.org/doi/10.1103/RevModPhys.89.015006>. Cited on page 51.

101 HETTICH, C. et al. Nanometer resolution and coherent optical dipole coupling of two individual molecules. *Science*, v. 298, n. 5592, p. 385–389, 2002. Disponível em: <https://www.science.org/doi/abs/10.1126/science.1075606>. Cited on page 51.

102 TREBBIA, J.-B. et al. Tailoring the degree of entanglement of two coherently coupled quantum emitters. *arXiv preprint arXiv:2109.10584*, 2021. Cited on page 51.

103 FLEISCHHAUER, M.; IMAMOGLU, A.; MARANGOS, J. P. Electromagnetically induced transparency: Optics in coherent media. *Reviews of modern physics*, APS, v. 77, n. 2, p. 633, 2005. Cited 2 times on pages 52 and 54.

104 HILL, S.; WOOTTERS, W. K. Entanglement of a pair of quantum bits. *Phys. Rev. Lett.*, American Physical Society, v. 78, p. 5022–5025, Jun 1997. Disponível em: <https://link.aps.org/doi/10.1103/PhysRevLett.78.5022>. Cited on page 54.

105 WOOTTERS, W. K. Entanglement of formation of an arbitrary state of two qubits. *Phys. Rev. Lett.*, American Physical Society, v. 80, p. 2245–2248, Mar 1998. Disponível em: <https://link.aps.org/doi/10.1103/PhysRevLett.80.2245>. Cited on page 54.

106 JOHANSSON, J.; NATION, P.; NORI, F. Qutip 2: A python framework for the dynamics of open quantum systems. *Computer Physics Communications*, v. 184, n. 4, p. 1234–1240, 2013. ISSN 0010-4655. Disponível em: <https://www.sciencedirect.com/science/article/pii/S0010465512003955>. Cited on page 54.

107 NEUZNER, A. et al. Interference and dynamics of light from a distance-controlled atom pair in an optical cavity. *Nature Photonics*, Nature Publishing Group, v. 10, n. 5, p. 303–306, 2016. Cited on page 55.

108 WELTE, S. et al. Photon-mediated quantum gate between two neutral atoms in an optical cavity. *Phys. Rev. X*, American Physical Society, v. 8, p. 011018, Feb 2018. Disponível em: <https://link.aps.org/doi/10.1103/PhysRevX.8.011018>. Cited on page 55.

109 MAJER, J. et al. Coupling superconducting qubits via a cavity bus. *Nature*, Nature Publishing Group, v. 449, n. 7161, p. 443–447, 2007. Cited on page 55.

110 CHOW, J. M. et al. Simple all-microwave entangling gate for fixed-frequency superconducting qubits. *Physical review letters*, APS, v. 107, n. 8, p. 080502, 2011. Cited on page 55.

111 BLATT, R.; WINELAND, D. Entangled states of trapped atomic ions. *Nature*, Nature Publishing Group, v. 453, n. 7198, p. 1008–1015, 2008. Cited on page 55.

112 HÄFFNER, H.; ROOS, C. F.; BLATT, R. Quantum computing with trapped ions. *Physics reports*, Elsevier, v. 469, n. 4, p. 155–203, 2008. Cited on page 57.

113 BLATT, R.; ROOS, C. F. Quantum simulations with trapped ions. *Nature Physics*, Nature Publishing Group, v. 8, n. 4, p. 277–284, 2012. Cited on page 57.

114 ESTÈVE, D.; RAIMOND, J.-M.; DALIBARD, J. *Quantum entanglement and information processing: lecture notes of the Les Houches Summer School 2003*. [S.l.]: Elsevier, 2004. v. 79. Cited on page 57.

115 LEIBFRIED, D. et al. Quantum dynamics of single trapped ions. *Rev. Mod. Phys.*, American Physical Society, v. 75, p. 281–324, Mar 2003. Disponível em: <https://link.aps.org/doi/10.1103/RevModPhys.75.281>. Cited 2 times on pages 61 and 63.

116 FLÜHMANN, C. et al. Encoding a qubit in a trapped-ion mechanical oscillator. *Nature*, v. 566, n. 7745, p. 513–517, Feb 2019. ISSN 1476-4687. Disponível em: <https://doi.org/10.1038/s41586-019-0960-6>. Cited on page 61.

117 SCHMIDT, P. O. et al. Spectroscopy using quantum logic. *Science*, American Association for the Advancement of Science, v. 309, n. 5735, p. 749–752, 2005. ISSN 0036-8075. Disponível em: <https://science.sciencemag.org/content/309/5735/749>. Cited on page 61.

118 BREWER, S. M. et al. $^{27}al^{+}$ quantum-logic clock with a systematic uncertainty below 10^{-18}. *Phys. Rev. Lett.*, American Physical Society, v. 123, p. 033201, Jul 2019. Disponível em: <https://link.aps.org/doi/10.1103/PhysRevLett.123.033201>. Cited on page 61.

119 AN, S. et al. Experimental test of the quantum Jarzynski equality with a trapped-ion system. *Nat. Phys.*, Nature Publishing Group SN -, v. 11, p. 193, Dec 2014. Disponível em: <https://doi.org/10.1038/nphys3197>. Cited 2 times on pages 61 and 65.

120 ROSSNAGEL, J. et al. A single-atom heat engine. *Science*, American Association for the Advancement of Science, v. 352, n. 6283, p. 325–329, 2016. ISSN 0036-8075. Disponível em: <https://science.sciencemag.org/content/352/6283/325>. Cited on page 61.

121 LINDENFELS, D. von et al. Spin heat engine coupled to a harmonic-oscillator flywheel. *Phys. Rev. Lett.*, American Physical Society, v. 123, p. 080602, Aug 2019. Disponível em: <https://link.aps.org/doi/10.1103/PhysRevLett.123.080602>. Cited on page 61.

122 MCCORMICK, K. C. et al. Quantum-enhanced sensing of a single-ion mechanical oscillator. *Nature*, v. 572, n. 7767, p. 86–90, Aug 2019. ISSN 1476-4687. Disponível em: <https://doi.org/10.1038/s41586-019-1421-y>. Cited 2 times on pages 61 and 67.

123 WOLF, F. et al. Motional fock states for quantum-enhanced amplitude and phase measurements with trapped ions. *Nature Communications*, v. 10, n. 1, p. 2929, Jul 2019. ISSN 2041-1723. Disponível em: <https://doi.org/10.1038/s41467-019-10576-4>. Cited on page 61.

124 ZHANG, J. et al. Noon states of nine quantized vibrations in two radial modes of a trapped ion. *Phys. Rev. Lett.*, American Physical Society, v. 121, p. 160502, Oct 2018. Disponível em: <https://link.aps.org/doi/10.1103/PhysRevLett.121.160502>. Cited on page 61.

125 WITTEMER, M. et al. Phonon pair creation by inflating quantum fluctuations in an ion trap. *Phys. Rev. Lett.*, American Physical Society, v. 123, p. 180502, Oct 2019. Disponível em: <https://link.aps.org/doi/10.1103/PhysRevLett.123.180502>. Cited on page 61.

126 OHIRA, R.; MUKAIYAMA, T.; TOYODA, K. Phonon-number-resolving detection of multiple local phonon modes in trapped ions. *Phys. Rev. A*, American Physical Society, v. 100, p. 060301, Dec 2019. Disponível em: <https://link.aps.org/doi/10.1103/PhysRevA.100.060301>. Cited 2 times on pages 61 and 65.

127 TAMURA, M.; MUKAIYAMA, T.; TOYODA, K. Quantum walks of a phonon in trapped ions. *Phys. Rev. Lett.*, American Physical Society, v. 124, p. 200501, May 2020. Disponível em: <https://link.aps.org/doi/10.1103/PhysRevLett.124.200501>. Cited on page 61.

128 MEEKHOF, D. M. et al. Generation of nonclassical motional states of a trapped atom. *Phys. Rev. Lett.*, American Physical Society, v. 76, p. 1796–1799, Mar 1996. Disponível em: <https://link.aps.org/doi/10.1103/PhysRevLett.76.1796>. Cited 3 times on pages 61, 63, and 65.

129 LEIBFRIED, D. et al. Experimental determination of the motional quantum state of a trapped atom. *Phys. Rev. Lett.*, American Physical Society, v. 77, p. 4281–4285, Nov 1996. Disponível em: <https://link.aps.org/doi/10.1103/PhysRevLett.77.4281>. Cited 2 times on pages 61 and 65.

130 SHEN, C.; ZHANG, Z.; DUAN, L.-M. Scalable implementation of boson sampling with trapped ions. *Phys. Rev. Lett.*, American Physical Society, v. 112, p. 050504, Feb 2014. Disponível em: <https://link.aps.org/doi/10.1103/PhysRevLett.112.050504>. Cited 2 times on pages 61 and 65.

131 UM, M. et al. Phonon arithmetic in a trapped ion system. *Nature Communications*, v. 7, n. 1, p. 11410, Apr 2016. ISSN 2041-1723. Disponível em: <https://doi.org/10.1038/ncomms11410>. Cited 2 times on pages 61 and 65.

132 DING, S. et al. Cross-kerr nonlinearity for phonon counting. *Phys. Rev. Lett.*, American Physical Society, v. 119, p. 193602, Nov 2017. Disponível em: <https://link.aps.org/doi/10.1103/PhysRevLett.119.193602>. Cited 2 times on pages 61 and 65.

133 MEIR, Z. et al. Single-shot energy measurement of a single atom and the direct reconstruction of its energy distribution. *Phys. Rev. A*, American Physical Society, v. 96, p. 020701, Aug 2017. Disponível em: <https://link.aps.org/doi/10.1103/PhysRevA.96.020701>. Cited 2 times on pages 61 and 65.

134 ROOS, C. F. et al. Nonlinear coupling of continuous variables at the single quantum level. *Phys. Rev. A*, American Physical Society, v. 77, p. 040302, Apr 2008. Disponível em: <https://link.aps.org/doi/10.1103/PhysRevA.77.040302>. Cited on page 61.

135 MARQUET, C.; SCHMIDT-KALER, F.; JAMES, D. F. V. Phonon–phonon interactions due to non-linear effects in a linear ion trap. *Applied Physics B*, v. 76, n. 3, p. 199–208, Mar 2003. ISSN 1432-0649. Disponível em: <https://doi.org/10.1007/s00340-003-1097-7>. Cited on page 61.

136 SCHUSTER, D. I. et al. Resolving photon number states in a superconducting circuit. *Nature*, v. 445, n. 7127, p. 515–518, Feb 2007. ISSN 1476-4687. Disponível em: <https://doi.org/10.1038/nature05461>. Cited 2 times on pages 61 and 67.

137 ARRANGOIZ-ARRIOLA, P. et al. Resolving the energy levels of a nanomechanical oscillator. *Nature*, Nature Publishing Group, v. 571, n. 7766, p. 537–540, 2019. Cited 2 times on pages 61 and 67.

138 GUERLIN, C. et al. Progressive field-state collapse and quantum non-demolition photon counting. *Nature*, v. 448, p. 889–893, Aug 2007. ISSN 1476-4687. Disponível em: <https://doi.org/10.1038/nature06057>. Cited on page 62.

139 AUTLER, S. H.; TOWNES, C. H. Stark effect in rapidly varying fields. *Phys. Rev.*, American Physical Society, v. 100, p. 703–722, Oct 1955. Disponível em: <https://link.aps.org/doi/10.1103/PhysRev.100.703>. Cited on page 62.

140 SØRENSEN, A.; MØLMER, K. Quantum computation with ions in thermal motion. *Phys. Rev. Lett.*, American Physical Society, v. 82, p. 1971–1974, Mar 1999. Disponível em: <https://link.aps.org/doi/10.1103/PhysRevLett.82.1971>. Cited on page 62.

141 HIGGINS, G. et al. Highly polarizable rydberg ion in a paul trap. *Phys. Rev. Lett.*, American Physical Society, v. 123, p. 153602, Oct 2019. Disponível em: <https://link.aps.org/doi/10.1103/PhysRevLett.123.153602>. Cited on page 63.

142 DELONE, N. B.; KRAINOV, V. P. AC stark shift of atomic energy levels. *Physics-Uspekhi*, Uspekhi Fizicheskikh Nauk (UFN) Journal, v. 42, n. 7, p. 669–687, jul 1999. Disponível em: <https://doi.org/10.1070/pu1999v042n07abeh000557>. Cited on page 66.

143 HÄFFNER, H. et al. Precision measurement and compensation of optical stark shifts for an ion-trap quantum processor. *Phys. Rev. Lett.*, American Physical Society, v. 90, p. 143602, Apr 2003. Disponível em: <https://link.aps.org/doi/10.1103/PhysRevLett.90.143602>. Cited on page 66.

144 BROWNNUTT, M. et al. Ion-trap measurements of electric-field noise near surfaces. *Rev. Mod. Phys.*, American Physical Society, v. 87, p. 1419–1482, Dec 2015. Disponível em: <https://link.aps.org/doi/10.1103/RevModPhys.87.1419>. Cited on page 66.

145 SAMES, C. et al. Continuous parametric feedback cooling of a single atom in an optical cavity. *Physical Review A*, APS, v. 97, n. 5, p. 053404, 2018. Cited on page 67.

146 GUERIN, W.; ROUABAH, M.; KAISER, R. Light interacting with atomic ensembles: collective, cooperative and mesoscopic effects. *Journal of Modern Optics*, Taylor & Francis, v. 64, n. 9, p. 895–907, 2017. Cited on page 86.

147 AKKERMANS, E.; MONTAMBAUX, G. *Mesoscopic physics of electrons and photons*. [S.l.]: Cambridge university press, 2007. Cited on page 86.

148 SHENG, P. *Introduction to wave scattering, localization and mesoscopic phenomena*. [S.l.]: Springer, 2006. v. 88. Cited on page 86.

Appendix

APPENDIX A – Scattering cross section and optical depth for a Λ three-level atom

In order to estimate the optical thickness for three-level atoms, we consider the main dynamical equations Eqs. (3.19)-(3.21) for the particular case of a single atom:

$$\frac{d\left\langle\hat{\sigma}_{nn}\right\rangle}{dt} = \frac{\Gamma_n}{2}\left\langle\hat{\sigma}_{33}\right\rangle - \frac{i}{2}\Omega_n\left(\left\langle\hat{\sigma}_{n3}\right\rangle - \left\langle\hat{\sigma}_{3n}\right\rangle\right), \tag{A.1}$$

$$\frac{d\left\langle\hat{\sigma}_{12}\right\rangle}{dt} = -i\left(\Delta_1 - \Delta_2\right)\left\langle\hat{\sigma}_{12}\right\rangle + \frac{i}{2}\Omega_1\left\langle\hat{\sigma}_{32}\right\rangle - \frac{i}{2}\Omega_2\left\langle\hat{\sigma}_{13}\right\rangle, \tag{A.2}$$

$$\frac{d\left\langle\hat{\sigma}_{n3}\right\rangle}{dt} = -\left[\frac{\left(\Gamma_1+\Gamma_2\right)}{2} + i\Delta_n\right]\left\langle\hat{\sigma}_{n3}\right\rangle - \frac{i}{2}\Omega_n\left(\left\langle\hat{\sigma}_{nn}\right\rangle - \left\langle\hat{\sigma}_{33}\right\rangle\right) - \frac{i}{2}\Omega_m\left\langle\hat{\sigma}_{12}\right\rangle, \tag{A.3}$$

for $m, n = 1, 2$, with $m \neq n$. In the steady state, the expectation value of the excited state population is given by

$$\left\langle\sigma_{33}\right\rangle_{ss} = \frac{4\Gamma\Delta_1^2\Omega_1^2\Omega_2^2}{\Gamma_2\Omega_1^2 A + \Omega_2^2 B}, \tag{A.4}$$

where

$$A = 4\Gamma^2\Delta_1^2 + \left(\Omega_1^2 + \Omega_2^2\right)^2, \tag{A.5}$$

$$B = \Gamma_1\left(4\Delta_1^2\left(\Gamma^2 - 2\Omega_2^2\right) + 16\Delta_1^4 + \left(\Omega_1^2 + \Omega_2^2\right)^2\right) + 8\Gamma\Delta_1^2\Omega_1^2. \tag{A.6}$$

Expression (A.4) allows us to obtain the scattering cross section $\sigma_{sc} = P_{sc}/I_0$, where P_{sc} represents the scattered power, and $I_0 \propto \left(\Omega_1/d_1\right)^2$ the incident field intensity.

In order to obtain P_{sc}, we consider the scalar scattered field (3.23) in the far-field approximation:

$$E_{sc}^{(far)}(r, \hat{\mathbf{k}}) \approx -\frac{\Gamma_1}{2d_1}\frac{e^{ik_1 r}}{k_1 r}\hat{\sigma}_{13}e^{-\hat{\mathbf{k}}.\mathbf{r}_0}, \tag{A.7}$$

where $\mathbf{r}_0$ is the position of the atom, and $\hat{\mathbf{k}}$ a unitary vector of observation in spherical coordinates. Since the scattered intensity is proportional to $I_{sc} \propto \left\langle E_{sc}^{\dagger} E_{sc}\right\rangle$, we then obtain

$$I_{sc}(r) \propto \left(\frac{\Gamma_1}{2d_1 k_1 r}\right)^2 \left\langle\hat{\sigma}_{33}\right\rangle_{ss}. \tag{A.8}$$

The integration of this intensity over an spherical shell results in the scattered power

$$P_{sc} \propto \left(\frac{\Gamma_1}{2d_1 k_1}\right)^2 \left\langle\hat{\sigma}_{33}\right\rangle_{ss} \int_0^{2\pi}\int_0^{\pi} \sin(\theta) d\theta d\phi \tag{A.9}$$

$$\propto \pi\left(\frac{\Gamma_1}{d_1 k_1}\right)^2 \left\langle\hat{\sigma}_{33}\right\rangle_{ss}. \tag{A.10}$$

Consequently, the scattering cross section for this three-level Λ system can be expressed as

$$\sigma_{sc} = \pi \left(\frac{\Gamma_1}{k_1 \Omega_1} \right)^2 \langle \hat{\sigma}_{33} \rangle_{ss} \,, \tag{A.11}$$

with $\langle \hat{\sigma}_{33} \rangle_{ss}$ given by Eq. (A.4). Finally, we can calculate the optical thickness for this system integrating the density over the cylinder propagation direction [146, 35]

$$\begin{aligned} b &= \sigma_{sc} \int_{-L/2}^{L/2} \rho\,(0,0,z)\, dz & \text{(A.12)} \\ &= \sigma_{sc} \rho L & \text{(A.13)} \\ &= \left(\frac{\Gamma_1}{\Omega_1} \right)^2 \langle \hat{\sigma}_{33} \rangle_{ss} \, \frac{N}{k_1^2 R^2}, & \text{(A.14)} \end{aligned}$$

where we used the fact that the average density $\rho = N/\pi R^2 L$ is constant over space [147, 148, 146]. Therefore, when varying L for a fixed homogeneous density, we are changing the optical thickness. Around the FWHM ($\Delta_1 = 0.125\Gamma$), we obtain $b \approx 0.36$ for $\rho = 0.01 k_1^3$ and $k_1 L = 40$, in the EIT regime: $\Gamma_1/\Gamma = \Gamma_2/\Gamma = 0.5$, $\Omega_1 = 0.1\Gamma$ and $\Omega_2 = 0.5\Gamma$.

APPENDIX B – Fock state detector

B.1 Experimental setup

The $^{88}Sr^{+}$ ion is trapped in a linear Paul trap. During a single experimental cycle the ion is first Doppler cooled using the $5^2S_{1/2} \leftrightarrow 5^2P_{1/2}$ transition. Afterwards, sideband cooling on the radial modes is applied to reach the motional ground state. After these steps the ion is in the state $|S\rangle \equiv \left|5^2S_{1/2}\,, m_J = -\frac{1}{2}\right\rangle$. Before the sequence of the Autler-Townes splitting, the ion is initialized in $|D\rangle \equiv \left|4^2D_{5/2}\,, m_J = -\frac{1}{2}\right\rangle$ via a π-pulse on the carrier transition.

For the weak probe, a laser beam at 45° angle to the longitudinal trapping axis was used. The remaining pulses on the qubit transition were performed with a beam coming from the radial direction (at a 90° to the trap axis). The fluorescence light is detected with a photomultiplier tube (PMT) mounted above the trap chamber. A sketch of the setup is shown in Fig. 19. The fluorescence detection is done via the $5^2S_{1/2} \leftrightarrow 5^2P_{1/2}$ transition. Photons are therefore only detected if the ion is in state $|S\rangle$.

B.2 Experimental parameters

For scans involving the Autler-Townes splitting, a probe time of 700 µs was used. For the strong coupling pulses, in both cases, one of the two radial motional modes was used.

For the Autler-Townes scheme in which the coupling was performed on a blue sideband (BSB) transition the Lamb-Dicke parameter was $\eta = 0.0609$. The radial sideband which was used for the coupling was detuned from the carrier transition by $\Delta = 2\pi \cdot 1.3433\,\text{MHz}$ and the coupling strength was $\Omega_C = 2\pi \cdot 10.05(11)\,\text{kHz}$.

The Lamb-Dicke parameter for the scans with red sideband (RSB) coupling was $\eta = 0.0605$. The radial sidband was detuned by $-2\pi \cdot 1.36\,\text{MHz}$ from the carrier transition and the coupling strength was $\Omega_C = 2\pi \cdot 11.08(11)\,\text{kHz}$ in this case.

To create the thermal distribution of phonons in Fig. 4 in the main text, the length of the sideband pulse in the cooling sequence was reduced. The optimized cooling on the RSB transition was set to be at 2500 µs. For the scan with $n_{th} = 1.13(6)$ the cooling time was reduced to 400 µs. The thermal distribution with $n_{th} = 4.4(3)$ was produced by cooling only for 200 µs.

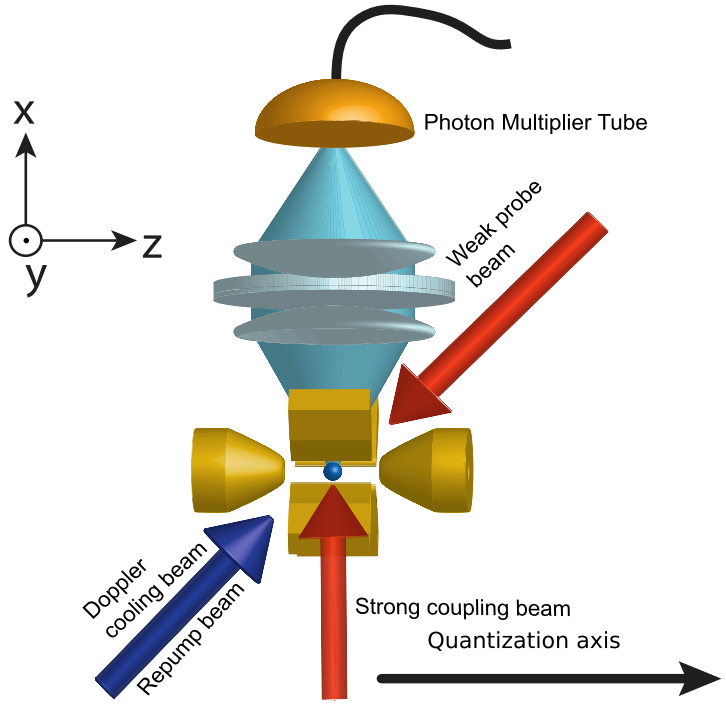

Figure 19 – The ion is trapped using a linear Paul trap. The cooling, repump laser and the weak probe beam are under a 45° angle to the trap axis. The remaining lasers for operations on the qubit transition are applied from the radial as well as then angled direction. Detection was done with a photomultiplier tube (PMT) mounted at the top of the experiment.

B.3 Autler-Townes line shape

Consider a three-level atomic system in a V level configuration, with a ground state $|S\rangle$ and excited states $|D\rangle$ and $|D'\rangle$. A probe field with Rabi frequency Ω_P and frequency ω_P couples the transition $|S\rangle \leftrightarrow |D\rangle$ while a control field of Rabi frequency Ω_C and frequency ω_C couples the transition $|S\rangle \leftrightarrow |D'\rangle$. The Hamiltonian that describes this system can be written as $H = H_0 + H_{int}$, with

$$H_0 = \omega_{D'}\sigma_{D'D'} + \omega_D\sigma_{DD} + \nu a^\dagger a \tag{B.1}$$

the term related to the atom's internal degrees of freedom and the free energy of the motional mode. ω_D and $\omega_{D'}$ are the frequencies of the states $|D\rangle$ and $|D'\rangle$, respectively, and ν is the motional mode frequency. The second term of the total Hamiltonian,

$$\begin{aligned} H_{int} \;=\; & \Omega_P\left(\sigma_{SD} + \sigma_{DS}\right)\left[e^{i(\omega_P t+\phi_P)} + e^{-i(\omega_P t+\phi_P)}\right] \\ & +\Omega_C\left(\sigma_{SD'} + \sigma_{D'S}\right)\left\{e^{i\left[\eta\left(a^\dagger+a\right)-\omega_C t+\phi_C\right]} + e^{-i\left[\eta\left(a^\dagger+a\right)-\omega_C t+\phi_C\right]}\right\} \end{aligned} \tag{B.2}$$

is the one containing all the interacting terms, where σ_{ii}, with $i = D, D'$ representing the population operators and $\sigma_{mn} = |m\rangle\langle n|$ the lowering and raising atomic operators,

which promote transitions from state $|m\rangle$ to $|n\rangle$, for $m \neq n$ and $m, n = S, D, D'$. η is the Lamb-Dicke parameter, ϕ_P and ϕ_C are the phases of the probe and control fields, respectively, and $a^\dagger(a)$ represents the creation (annihilation) operator acting on the Fock space. Here we have considered that the classical probe field does not couple the motional degrees of freedom of the atom.

For convenience, we move to the interaction picture using the unitary transformation $U_0 = e^{-iH_0 t}$. Then, applying the Rotating Wave Approximation (RWA), in the Lamb-Dicke and low excitation regimes, i.e. $\eta \ll 1$ and $\eta\sqrt{\langle (a^\dagger + a)^2 \rangle} \ll 1$, the Hamiltonian reads

$$H_I = \Omega_C \sigma_{SD'} e^{i(\Delta_C t + \phi_C)} \left[1 + i\eta \left(a^\dagger e^{i\nu t} + a e^{-i\nu t}\right)\right] + \Omega_P \sigma_{SD} e^{i(\Delta_P t - \phi_P)} + H.c., \quad \text{(B.3)}$$

where $H.c.$ represents the Hermitian conjugate.

Choosing a particular phase and considering a resonant probe field, the Hamiltonian becomes

$$H_I = \Omega_C \sigma_{SD'} e^{i\Delta_C t} \left[1 + i\eta \left(a^\dagger e^{i\nu t} + a e^{-i\nu t}\right)\right] + \Omega_P \sigma_{SD} + H.c. \quad , \quad \text{(B.4)}$$

where we notice that there are three possible resonances for the coupling field: $\Delta_C = 0$, which leads to a carrier transition where the number of excitations in bosonic mode is not affected by the control field, $\Delta_C = -\nu$, that couples to the first red sideband (RSB) transition, and $\Delta_C = \nu$, coupling the first blue sideband (BSB) transition.

Next we obtain the lineshape for both the RSB and BSB transitions. It is important to stress that the linewidths predicted in this appendix are nothing more than a prediction for an ideal case. During the experiment, other sources of noise are present, such as fluctuations in laser intensity, pulse lengths, and motional heating. These noise sources cannot be neglected, and are generally predominant in the determination of the lineshapes.

B.3.1 Red-sideband (RSB)

Considering $\Delta_C = -\nu$, the Hamiltonian in Eq.B.4 can be rewritten as

$$H = \Omega_P \sigma_{SD} + g a^\dagger \sigma_{SD'} + H.c., \quad \text{(B.5)}$$

with $g = i\eta\Omega_C$. In the basis of n excitations in the bosonic mode $b = \{|S, n-1\rangle, |D, n-1\rangle, |D', n\rangle\}$ the three eigenvalues of this Hamiltonian are $E_0^{(n)} = 0$ and $E_\pm^{(n)} = \pm\sqrt{g^2 n + \Omega_P^2}$, which means that the system has a dark state with zero eigenenergy, and two symmetric eigenstates energetically separated by $2\sqrt{g^2 n + \Omega_P^2}$. In a general form, these eigenstates can be written as

$$\begin{aligned} |a_0^{(n)}\rangle &= N_n^{a_0} \left[|D, n-1\rangle - \frac{\Omega_P}{g\sqrt{n}} |D', n\rangle\right], \\ |\pm^{(n)}\rangle &= N_n^{\pm} \left[|S, n-1\rangle \pm \left(\frac{\Omega_P}{\sqrt{g^2 n + \Omega_P^2}} |D, n-1\rangle + \frac{g\sqrt{n}}{\sqrt{g^2 n + \Omega_P^2}} |D', n\rangle\right)\right], \end{aligned} \quad \text{(B.6)}$$

with N_n^D and $N_n^\pm$ being normalization factors.

In the regime where the control field is much stronger than the probe field, i.e., $g\sqrt{n} \gg \Omega_P$, these eigenenergies and eigenstates become

$$E_0^{(n)} = 0 \quad : \quad |a_0^{(n)}\rangle = |D, n-1\rangle, \tag{B.7}$$

$$E_\pm^{(n)} = \pm g\sqrt{n} \quad : \quad |\pm^{(n)}\rangle = \frac{1}{\sqrt{2}}\left(|S, n-1\rangle \pm |D', n\rangle\right), \tag{B.8}$$

in accordance with the dressed state representation of the system. In this dressed state representation, the system is composed by $|D, n\rangle$ and the two symmetric states $|\pm^{(n)}\rangle$, with probe resonance at $\Delta_P = \pm g\sqrt{n}$.

The lineshape width can be obtained, for a system with n excitations in the Fock space by calculating the total decay rate from one of the dressed states $|\pm^{(n)}\rangle$ using Fermi's golden rule, with the respective collapse operators. Concerning the spontaneous decay processes in the system, the total decay rate is obtained considering the collapse operator $\sqrt{2\Gamma_{SD'}}\sigma_{SD'}$, resulting in

$$\begin{aligned} \Gamma_{\text{atom}} &= \left|\langle S, n-1|\sqrt{2\Gamma_{SD'}}\sigma_{SD'}|+^{(n)}\rangle\right|^2 \\ &= \Gamma_{SD'}. \end{aligned} \tag{B.9}$$

For the contribution of the motional mode dissipation and heating in the lineshape width, we consider the collapse operators $\sqrt{2\kappa\left(n_{\text{th}}+1\right)}a$ and $\sqrt{2\kappa n_{\text{th}}}a^\dagger$, with n_{th} being the mean thermal phonon number. So the total contribution is given by

$$\begin{aligned} \kappa_T &= \left|\langle S, n-2|\sqrt{2\kappa\left(n_{\text{th}}+1\right)}a|+^{(n)}\rangle\right|^2 + \left|\langle D', n-1|\sqrt{2\kappa\left(n_{\text{th}}+1\right)}a|+^{(n)}\rangle\right|^2 \\ &\quad + \left|\langle S, n|\sqrt{2\kappa n_{\text{th}}}a^\dagger|+^{(n)}\rangle\right|^2 + \left|\langle D', n+1|\sqrt{2\kappa n_{\text{th}}}a^\dagger|+^{(n)}\rangle\right|^2 \\ &= \kappa\left[2n\left(2n_{\text{th}}+1\right)-1\right]. \end{aligned} \tag{B.10}$$

Then, the spectral lineshape is fully characterized, with resonances located at $\Delta_P = \pm g\sqrt{n}$ and with the FWHM $= \Gamma_{SD'} + \kappa\left[2n\left(2n_{\text{th}}+1\right)-1\right]$.

B.3.2 Blue sideband (BSB)

In the case when the control field is resonant with the first blue sideband transition, i.e., $\Delta_C = \nu$, the Hamiltonian from Eq.B.4 becomes

$$H = \Omega_P\sigma_{DS} + ga\sigma_{SD'} + H.c.. \tag{B.11}$$

In the basis of n excitations in the phonon mode $b = \{|S, n\rangle, |D, n\rangle, |D', n+1\rangle\}$, we obtain, in the regime where $g\sqrt{n+1} \gg \Omega_P$, the eigenvalues $E_0^{(n)} = 0$ and $E_\pm^{(n)} =$

$\pm g\sqrt{n+1}$, and their respective eigenstates:

$$|a_0^{(n)}\rangle = |D,n\rangle, \tag{B.12}$$

$$|\pm^{(n)}\rangle = \frac{1}{\sqrt{2}}\left(|S,n\rangle \pm |D',n+1\rangle\right), \tag{B.13}$$

where the only difference from the RSB transition is the effective coupling strength being now $g\sqrt{n+1}$. Consequently, this will also alter the Autler-Townes splitting.

The total spontaneous decay rate, considering the same collapse operator $\sqrt{2\Gamma_{SD'}}\sigma_{SD'}$, is given by

$$\begin{aligned}\Gamma_{\text{atom}} &= \left|\langle S,n+1|\sqrt{2\Gamma_{SD'}}\sigma_{SD'}|+^{(n)}\rangle\right|^2 \\ &= \Gamma_{SD'},\end{aligned} \tag{B.14}$$

while the contribution from the dissipation of the phonon mode, obtained with the collapse operators $\sqrt{2\kappa\left(n_{\text{th}}+1\right)}a$ and $\sqrt{2\kappa n_{\text{th}}}a^\dagger$, is

$$\begin{aligned}\kappa_T &= \left|\langle S,n-1|\sqrt{2\kappa\left(n_{\text{th}}+1\right)}a|+^{(n)}\rangle\right|^2 + \left|\langle D',n|\sqrt{2\kappa\left(n_{\text{th}}+1\right)}a|+^{(n)}\rangle\right|^2 \\ &\quad + \left|\langle S,n+1|\sqrt{2\kappa n_{\text{th}}}a^\dagger|+^{(n)}\rangle\right|^2 + \left|\langle D',n+2|\sqrt{2\kappa n_{\text{th}}}a^\dagger|+^{(n)}\rangle\right|^2 \\ &= \kappa\left[2n\left(2n_{\text{th}}+1\right)+4n_{\text{th}}+1\right].\end{aligned} \tag{B.15}$$

This means that in the case of a BSB transition, the spectral lineshape is characterized by resonances located at $\Delta_P = \pm g\sqrt{n+1}$ and a FWHM $= \Gamma_{SD'} + \kappa\left[2n\left(2n_{\text{th}}+1\right)+4n_{\text{th}}+1\right]$.